# ENERGY HARVESTING FROM LOCALIZED DYNAMIC TRANSITIONS IN POST-BUCKLED ELASTIC BEAMS UNDER QUASI-STATIC LOADING

By

Wassim Borchani

A DISSERTATION

Submitted to
Michigan State University
in partial fulfillment of the requirements
for the degree of

Civil Engineering - Doctor of Philosophy

2015

## ABSTRACT

ENERGY HARVESTING FROM LOCALIZED DYNAMIC TRANSITIONS IN POST-BUCKLED ELASTIC BEAMS UNDER QUASI-STATIC LOADING

By

Wassim Borchani

The deployability of structural health monitoring self-powered sensors relies on their capability to harvest energy from signals being monitored. Many of the signals required to assess the structure condition are quasi-static events which limits the levels of power that can be extracted. Several vibration-based techniques have been proposed to increase the transferred level of power and broaden the harvester operating bandwidth. However, these techniques require vibration input excitations at frequencies higher than dominant structural response frequencies which makes them inefficient and not suitable for ambient quasi-static excitations.

This research proposes a novel sensing and energy harvesting technique at low frequencies using mechanical energy concentrators and triggers. These mechanisms consist of axially-loaded bilaterally-constrained beams with attached piezoelectric energy harvesters. When the quasi-static axial load reaches a certain mechanical threshold, a sudden snap-through mode-switching occurs. These transitions excite the attached piezoelectric scavengers with high-rate input accelerations, generating then electric power. The main objectives are to understand and model the post-buckling behavior of bilaterally-constrained beams, control it by tailoring geometry and material properties of the buckled elements or stacking them into system assemblies, and finally characterize the energy harvesting and sensing capability of the system under quasi-static excitations.

The fundamental principle relies on the following concept. Under axial load, a straight slender beam buckles in the first buckling mode. The increased transverse deformations from a buckled shape lead to contact interaction with the lateral boundaries. The contact interaction

generates transverse forces that induce the development of higher order buckling configurations. Transitions between the buckled configurations occur not only during loading, but also unloading.

In this work, the post-buckling response of the bilaterally constrained beam subjected to axial loading is investigated experimentally, numerically, and theoretically. The capability of the system to generate electric energy under quasi-static excitation is also assessed experimentally. The post-buckling behavior is reproducible under cyclic loadings and independent of the input loading frequency. The static and dynamic response of the beam is theoretically studied using an energy method. The model adequately predicts the beam geometry at every loading stage, including the flattening behavior just before the snap buckling transitions, the mode transition events and the released kinetic energy as well as accelerations of the beam during transitions. The buckling transitions generate high kinetic energy and acceleration spikes. However, the location of the maximum acceleration differs from one transition to another.

Tuning the parameters of the system affects dramatically the accelerations generated during snap-through transitions. However, it does not affect the number and spacing between these events. To achieve better control of the system, multiple slender beams with different geometric and material properties are stacked in parallel configurations. The system allows then to control the spacing between energy bursts and reduce the energy leakage in electronic circuits.

As an application example, the mechanical energy concentrators and triggers were integrated with a piezo-floating gate events sensor. This allowed for harvesting and recording of bursts and impulses of released energy at very low frequencies. The system can be calibrated to determine the number of times the magnitude of the input signal exceeded a mechanical threshold. The mechanism allows for frequency up-conversion from the low input frequency (in the order of mHz) to the natural frequency of the piezoelectric scavenger.

To my parents, for their devotion and sacrifice,
To my fiancée, for her love and support,
To my siblings, for their help and encouragement,
To my friends, with whom I spent so many precious moments.
I dedicate my work,
Symbol of gratitude and love.

# ACKNOWLEDGEMENTS

I would like to express my deepest gratitude to Dr. Nizar Lajnef and Dr. Rigoberto Burgueño for their excellent guidance, valuable knowledge, and precious comments and advices that helped me carry out my research.

I would like to extend my sincere appreciation to the rest of my committee members, Professor Brian Feeny and Professor Venkatesh Kodur, for their availability, guidance and valuable comments.

Special thanks should go to Dr. Shantanu Chakrabartty for his contribution on the sensor work and Dr. Yi Sun for his help with the finite element modeling.

Finally, I would like to thank my family and friends for their support and encouragement.

# TABLE OF CONTENTS

# LIST OF TABLES

# LIST OF FIGURES

# CHAPTER 1: INTRODUCTION

The presented work in this thesis builds on the novel idea of exploiting snap-through transitions in post-buckled elastic elements to harvest energy at very low frequencies. The original concept is a result of collaboration between Dr. Nizar Lajnef and Dr. Rigoberto Burgueño. The developed theoretical model, detailed in Chapter 4, constitute the major contribution of this thesis. The sensor related work presented in Chapter 5 was developed in collaboration with Dr. Chakrabartty.

## 1.1. Motivation and vision

Development of smart structures capable of monitoring critical events and alerting users has been a quest for decades. Different sensors have been developed to monitor the events that a structure can be subjected to, such as vibrations, displacements, pressure, temperature, etc. Monitoring systems, composed of a network of wireless sensors capable to communicate between themselves and with a central computer, can detect the change in the structure response, due to crack initiation or failure of one or multiple elements, and alert engineers for maintenance. However wireless monitoring systems require a continuous source of power that a battery cannot provide due to its limited lifetime. Therefore, self-powered sensors capable of harvesting energy from the signal being sensed are needed.

Although many potential sources of energy are available such as solar, thermal gradient, radio frequency, vibrations and strain energies, piezoelectric harvesters are the most promising for deployment in structures, given the size limitations and the possibility of being embedded within the construction material. One of the major disadvantages of the electro-mechanical energy

scavengers available for civil, mechanical and biomechanical applications is their narrow-band frequency response, which is concentrated around high frequencies. For instance a vibration-based scavengers with an overall volume limited to less than 5 $cm^3$ will exhibit a resonant frequency in the range 50-300 Hz (Najafi et al. 2011), while most civil structures have a fundamental vibration mode at frequencies less than 5 Hz. Likewise, changes in physical processes like temperature and pressure variations between day and night induce a stress/strain response in structures that occur at frequencies lower than 1 mHz. In biomedical engineering, changes in in-vivo strain levels during bone-healing and spinal fusion processes span from a few days to up to a few months. In all these processes monitoring the evolution of quasi-static strain is important and could provide significant benefits. For instance, the history of mechanical loading inside different structures could be used to predict the life expectancy of the structure. A more challenging prospect is to design battery-less sensors that can self-power by harvesting energy directly from these quasi-static processes.

The mismatch between the input excitation frequency and the natural frequency of the energy harvester significantly limits the levels of extractable power. Several techniques have been proposed to increase the transferred power level, including improvements through the optimization of the piezoelectric material, altering of the electrode patterns and system configuration, use of matching networks, and tuning of the device's resonant frequency. However, energy harvesting from loads, deformations, or motions within the quasi-static frequency range is beyond the reach of current vibration-based energy harvesting methods. The developed energy harvesters to date are still inefficient and not suitable for low frequency vibration sources such as human walking motion and deformations in large civil structures (Green et al. 2013).

This research presents a new technique for sensing and energy harvesting at very low frequencies (less than 1 Hz) using mechanical energy concentrators and triggers. These systems

exploit the sudden snap-through behavior between the multiple buckling modes of an axially-loaded bilaterally-constrained beam. As the axial loading increases, the strain energy that is stored in the buckled element is released as kinetic energy during mode transitions. The approach relies on the high-rate motions that are generated during the transitions between the system's multiple potential energy wells. The input is not a vibration motion but a slow quasi-static deformation. The vision for the proposed energy harvesting concept is illustrated in Figure 1-1. The presented concept is shown packaged into a device for embedment or attachment to structural components in a form-factor similar to vibrating wire strain gages. Under quasi-static structural deformations (e.g., due to service deformations, temperature fluctuations, or slow degradation in material properties), the device capsule is compressed (or tensioned), inducing variations in axial deformations to the enclosed beam element. The axial deformations imposed on the internal element leads to multiple bifurcation points in its post-buckling response due to the presence of bilateral constraining walls. Energy harvesting oscillators, attached to the axially compressed element, are excited by the sudden snap-through transitions in the beam. This conversion, from low-rate axial deformations to dynamic high-rate lateral accelerations allows the harvesting of energy from a global quasi-static input.

A piezoelectricity driven self-powered sensor contains a piezoelectric transducer that powers a minimal set of electronic modules by harvesting energy from ambient strain variations. The sensor electronics comprises of a rectification module to extract energy from the transducer, a triggering module that detects events of interest and a data-logging module that records events either on a non-volatile memory or using remote data transmission. When the piezoelectric transducer is excited quasi-statically the load voltage generated by the transducer is approximately constant. Unfortunately, the majority of the charge generated by the transducer is lost as leakage

through the electronics (for example through diode leakage) and the residual energy is insufficient to drive the rest of the sensor modules (triggering and data-logging modules).

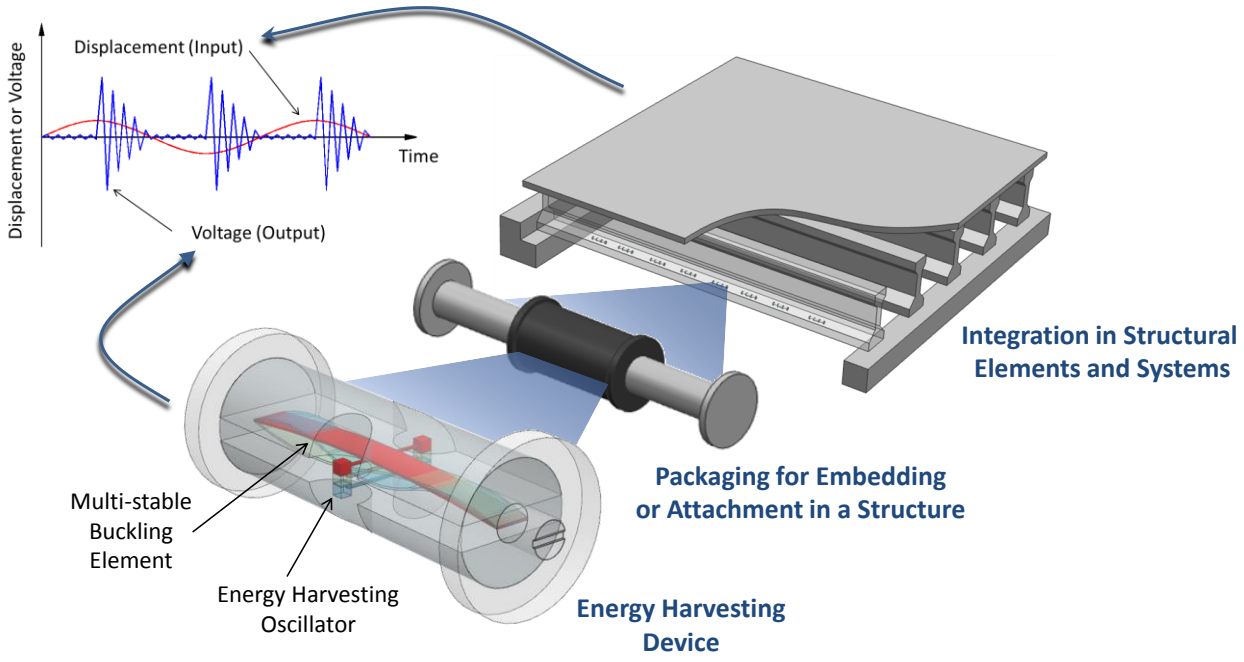


Figure 1-1: Schematic illustrating the integration and relevance of the presented concept for enhanced energy harvesting capabilities from quasi-static deformations in civil infrastructure.

This work proposes the use of mechanical energy concentrators and triggers as a front-end to circumvent the challenge of quasi-static self-powering. The role of the mechanical energy concentrator is to harvest potential energy over a long time-span and release the stored energy as bursts and impulses. The impulsive nature of the energy-release not only results in piezoelectric output voltage levels that are significantly higher than the triggering but also reduces the effect of energy leakage. Management of the extracted energy for use or storage is an important component for implementation of the concept.

## 1.2. Literature review

Buckling and post-buckling theories of elastic structures have been studied extensively for over 80 years (Euler, 1744; Hutchinson and Koiter, 1970 and Burgess, 1971). Most efforts have been focused on preventing global and local instability. However, recent attention has been paid to the potential of using post-buckling behavior for deployable and active structures. Buckled structures have been used to create bistable and multistable mechanisms that have proven to be efficient in many applications such as MEMS and energy harvesting devices (Fang and Wickert, 1994; Qiu et al., 2004; Jung and Yun, 2010; Masana and Daqaq, 2011; Lajnef et al., 2014b).

### *1.2.1. Buckling and post-buckling of elastic structures*

Buckling and post-buckling of an unrestrained beam under compressive axial stress was studied by Fang and Wickert (1994). Accounting for beam imperfections and nonlinear dependence of the transverse deflection and the compressive load, it was shown that the beam deflects only in the first mode and exhibits a continuous increase in the transverse deflection amplitude during the post-buckling response. Therefore the beam does not exhibit snap-through behavior during its post-buckling responses.

Bistability of a bow-shaped curved beam subjected to transverse force acting at its midspan without axial residual stress was theoretically investigated by Qiu et al. (2004) using energy methods. It was shown that the beam snaps under the applied actuation but does not stay in the snapped shape if the force is released. Park and Hah (2008) analyzed pre-shaped buckled-beam actuators subjected to a transverse distributed force taking into consideration the existence of an axial residual stress. It was shown that the stability of the second equilibrium position depends on the ratio between the beam's thickness and initial transverse curvature at midspan as well as

residual stresses in the beam. Results also indicate that transitions between the two equilibrium configurations do not follow the same equilibrium path.

Post-buckling behavior of buckled beams subjected to both axial and concentrated transverse loading has also been theoretically studied for central and non-central actuations (Vangbo, 1998; Cazottes et al., 2009). Equilibrium configurations were determined by minimization of the system's energy taking into consideration bending and compression. It was shown that the transverse force that should be applied to snap the beam into the second stable state depends on the pre-compression force. In addition, the position of the actuation was shown to significantly affect the system's behavior.

In an effort to generate higher buckling modes beyond the bistable configurations, several studies have been conducted on the post-buckling response of unilaterally constrained beams subjected to axial compressive forces. Stein and Wriggers (1984) used Timoshenko beam theory with large deformations and rotations to numerically investigate the problem. It was shown that the elastica buckles until it touches the lateral constraint. The system then regains stiffness and is able to carry higher loading. Chateau and Nguyen (1991) demonstrated that a contact zone develops under increased loading leading to localized buckling in that area and thus an upper buckling mode. Increasing the input loading will result in multiple contact regions with distributed reaction forces (Essenburg, 1975). Soong and Choi (1986) studied the contact problem between a beam and its boundary. The contact involves friction. The normal pressures as well as tangential forces at the contact zone were determined. It was shown that the axial compression force inside the beam is not constant due to friction. Line contacts were simplified into multiple discrete points under the condition that none of the contact points has a curvature that cuts into the local boundary. Naghdi and Rubin (1989) showed that accounting for normal extensional deformation describes

better the contact problem and correctly predicts the conditions under which the beam loses contacts.

Methods based on geometric assumptions have been the most common way to model the observed behavior for this class of problems. However, this approach significantly overestimates the required force-displacement conditions for the higher modes transitions. Numerical simulations are typically used to overcome the mismatch with measured experimental results. In the work developed by two research groups (Domokos et al., 1997; Holmes et al., 1999; Chai, 1998), the post-buckling behavior of an inextensible beam confined between two frictionless rigid side-walls and subjected to axial displacement was investigated using analytical-computational methods. Large deformations and geometric elliptic integrations were used. It was shown that a combination of line and point contacts can exist and that the deflected shape can be asymmetric. Therefore friction has to be considered in the study to more accurately describe equilibrium states and critical loads and displacements (Domokos et al., 1997; Holmes et al., 1999). Transitions to a higher buckling mode were assumed to be always bounded between a lower limit, corresponding to a single flattened contact zone, and an upper limit, corresponding to multiple flattened contact segments of equal lengths (Chai, 1998). The lateral reactions exerted by the constraints were modeled as a set of discrete point forces acting at the ends of the free standing segments of the beam. The case of a bilaterally constrained thin plate subjected to height reduction was also investigated by Roman and Pocheau (2002) through a combined experimental, theoretical, and numerical study. Experimental measurements of the contact zone length were fed back into the model to calibrate for the plate reactions. It was shown that even though friction is an important parameter, the assumed frictionless symmetric Euler's model combined with the added corrections can represent the considered behavior. Based on the collected literature for this class of problems,

it was determined that a theoretical model that is based on the physics of the device is relevant, thus the interest in this work for energy methods.

### *1.2.2. Limitation of existing energy harvesting techniques at very low frequency excitations*

Energy harvesting from loads, deformations, or motions within the quasi-static frequency range is beyond the reach of current vibration-based energy harvesting methods. Although many research works have focused on vibration energy harvesting (Elfrink et al.. 2008; Elvin et al., 2006; Finkel et al., 2009; Park et al., 2008; Rahimi et al., 2003; Sodano et al., 2004), the developed energy harvesters to date are still inefficient and not suitable for low frequency vibration sources such as human walking motion and deformations in large civil structures (Green et al., 2013). The major limitation in vibration energy harvesting revolves around the fact that the energy harvester should be excited at, or near, its resonance frequency in order to generate the most energy. Thus the vibrator should be tuned to match the most distinct frequency of the vibration source. In general, the excitation frequency varies over a large spectrum, which considerably reduces the efficiency of the harvester. Different methods to broaden the generator's operating bandwidth have been explored. Twiefel and Westermann (2013) present a survey on broadband techniques for vibration energy harvesting and classify the techniques as advanced electronic networks, linear generators and nonlinear generators. The latter two methods deal with mechanical systems and are the closest related to the work presented here. Thus, their features, advantages and disadvantages are summarized next.

Linear generators, characterized by the harvester's specific natural frequencies, are well suited for narrowband excitations. However, they are less efficient if the excitation frequency is distributed over a wide spectrum or if the frequency is very low. One way to increase their

operation bandwidth is by using an array of piezoelectric generators (e.g., cantilevered beams) with different tuned resonant frequencies (Liu et al., 2008). Another approach is to couple bimorph beams with elastically connected masses and tune their response such that they have resonant frequencies close to each other, and a wider band can be achieved by connecting more beams (Erturk et al., 2009; Yang and Yang, 2009). These methods can be effective and simple. Yet the drawbacks are that the setups can become voluminous for a wide frequency band and that mode coupling can reduce the overall response.

A number of research studies have been focused on exploiting response nonlinearities of vibration harvesters to improve energy generation and extend bandwidth. Proposed techniques include vibroimpact, monostable (Duffing) and bistable/multistable systems. Vibroimpact systems use a mechanical stopper to limit the amplitude of the harvester's vibrations such that if the excitation frequency increases the system response remains on a plateau defined by the stopper's positions (Soliman et al, 2008; Moss et al, 2010; Blystad and Halvorsen, 2011). The technique provides a wider bandwidth around the harvester's resonant frequencies but it is not practical since a slowly increasing frequency sweep is required to reach a wide plateau.

Nonlinear monostable harvesters exhibit a wider bandwidth and higher efficiency in a non-stationary vibratory environment than linear generators. The harvester's behavior is governed by Duffing equations where cubic stiffness nonlinearities can be incorporated into the harvester's design using nonlinear magnetic levitation (Mann and Sims, 2009) or by axially loading the harvester in the pre-buckling state (Daqdaq, 2010). The potential energy function of these harvesters exhibits monostable characteristics that can broaden the frequency bandwidth. However, the nonlinearity in monostable harvesters can reduce the mean output power under

colored random excitations (Daqdaq, 2010; Barton et al., 2010), and it has been shown that it has no effect on the output under white noise excitation (Langley, 2014).

Another class of nonlinear harvesters is bistable and multistable generators, which are characterized by two or more potential energy wells defining stable equilibrium positions. Depending on the excitation level and frequency these devices can exhibit either a periodic or a chaotic inter-well vibration. This behavior increases the range of frequency at which energy can be harvested (Tang et al., 2010; Zhu et al., 2010). Bistability can be introduced into energy harvesters using different techniques such as magnetic repulsion (Tang et al., 2010; Stanton et al., 2009), magnetic attraction (Erturk et al, 2009; Galchev et al., 2011) and mechanical buckling (Jung and Yun, 2010; Sneller et al., 2011). Multistable systems using multiple attracting positions to the oscillating magnet have also been investigated and shown to improve efficiency for low frequency input (Wickenheiser and Garcia, 2010). Bistable/multistable generators exhibit good performance in terms of power conversion and frequency broadband; but for very low-frequency applications they should be designed accurately in order to be efficient.

Green et al. (2013) numerically investigated the effectiveness of current nonlinear energy harvesting solutions for real ambient low frequency vibration sources. It was concluded that the efficiency of nonlinear harvesters is sensitive to the nature and type of the excitation and that the development of new devices capable of harvesting energy at very low frequency is needed. The dominant frequencies of human motions and large civil structure vibrations are less than 10 Hz (Najafi et al., 2011). Furthermore, under service loading, civil structures typically exhibit small amplitude low-rate deformations and significantly small vibration motions. Hence, the vibration energy harvesting devices mentioned above are inefficient and not suitable for this kind of application.

## 1.3. Research hypothesis and objectives

### *1.3.1. Hypothesis*

The main hypothesis behind this research is that energy can be harvested under quasi-static excitations using sudden transitions between equilibrium positions of bilaterally constrained beams. Instabilities of buckled elements can be exploited to transform the low-amplitude and low-rate service and ambient deformations into an amplified input to the piezoelectric transducer. Post-buckling response of elastic elements can be modeled and controlled for enhanced power management.

### *1.3.2. Objectives*

The main objective of this research is to develop a sensing and energy harvesting technique that is efficient at very low frequency and quasi-static excitations. The technique uses the snap-through behavior between the multiple buckling modes of a bilaterally constrained axially loaded beam to convert the low-amplitude and low-rate excitations into an amplified input to the piezoelectric scavenger. This work aims to model and control the post-buckling response of bilaterally constrained beams to maximize the levels of the extractable energy by optimizing system's parameters. To provide better understanding of the behavior and control it, theoretical modeling, finite element simulations and experiments were carried out.

A theoretical model of the post-buckling behavior of bilaterally constrained beams was developed based on an energy approach. The method minimizes the energy stored in the system to determine the deflected shapes for different load values as well as the transition states. The model detects the loads at which mode transitions occur. It also computes velocities, accelerations and energies during transitions.

Finite element simulations were performed in order to study the effect of the system's parameters on the post-buckling response of the bilaterally constrained beam. The parameters' effect on the maximum accelerations during transitions was investigated to maximize the levels of the extractable energy. The finite element method was also used to investigate the effect of combining multiple slender elastic beams, in parallel configurations, on the number and magnitude of mode branch switching events during the post-buckling response of the system.

To validate the theoretical and numerical models, an experimental apparatus was built and the post-buckling response of the beam was experimentally investigated. Piezoelectric scavengers with different natural frequencies were used to convert the high-rate motion of the beam, at transitions, into electric power. The effect of the excitation frequency as well as the natural frequency of the piezoelectric transducer on the levels of the extractable energy was experimentally investigated. The sensing ability of the developed system to low-frequency and quasi-static events was experimentally investigated by combining the mechanical energy concentrators and triggers with piezo-floating-gate sensors.

## 1.4. Outline

This dissertation is organized as follows: Chapter 2 presents a background review on energy harvesting techniques using bistable mechanisms, buckling eigenvalue analysis and the study of post-buckling behavior of bilaterally constrained beams. Chapter 3 provides experimental and numerical investigations of the post-buckling response of one and multiple parallel bilaterally constrained beams. This chapter assesses the repeatability and the reproducibility of the behavior and its dependency to the input frequency and the parameters of the system such as thickness, length and Young's modulus of the beam and the gap between the lateral rigid walls. Chapter 4

presents a theoretical study of the post-buckling behavior of the system under consideration. The study is based on an energy method. Static and dynamic models are developed to determine the response of the beam as well as energy balance and conversion during buckling mode transitions. Chapter 5 provides a novel technique for energy harvesting and self-powered sensing at very low frequency environments. The technique consists in using mechanical energy concentrators (composed of axially-loaded bilaterally-constrained beams) to convert a quasi-static strain input into a high-rate acceleration that transfers the input into a piezoelectric scavenger. The technique combines the physics of mechanical buckling in bilaterally constrained elastic beams with the physics of piezoelectricity driven hot-electron injection, thus creating a novel sensing mechanism able to self-power at milli- and micro-Hertz frequencies.

# CHAPTER 2: BACKGROUND

## 2.1. Overview

This chapter presents some experimental and theoretical background related to buckling and post-buckling of elastic structures and energy harvesting using bistability of buckled elements. The theoretical background presented in this chapter was used in the development of the theoretical model established in the current work. The chapter is divided into 4 separate sections. Section 2.2 presents a broadband energy harvesting technique that exploits bistability of buckled elements to up-convert low input frequencies into the energy harvester's resonant frequency. Section 2.3 presents a buckling eigenvalue analysis developed by Nayfeh and Emam (2004) to determine the buckling critical loads and modes. Section 2.4 summarizes a theoretical model on the post-buckling behavior of a bilaterally constrained beam under axial loads developed by Chai (1998). The results of this model will be compared to our theoretical model's in the following chapters. Section 2.5 presents a study of the contact between an elastica and its boundary involving friction. The formulation was used to investigate the effect of friction on the post-buckling behavior of the bilaterally constrained beam under study.

## 2.2. Broadband energy harvesting using bistable buckled elements

Jung and Yun (2010) presented an energy-harvesting device that employs both mechanical frequency up-conversion and bistable behavior of buckled bridges for wide-bandwidth operations at an ambient vibration frequency. The proposed device enables energy harvesting at slow and time-varying mechanical vibrations. The schematic of the proposed energy harvester is shown in

Figure 2-1 (a), and a photograph of the experimental setup of the fabricated device is shown in Figure 2-1 (b). The device consists of two pre-buckled slender bridges and cantilever beams attached to the bridges. A proof mass is mounted on top of the bridge at the center to provide sufficient inertial force at a given acceleration. A piezoelectric polymer polyvinylidene fluoride (PVDF) layer is attached on top of each cantilever beam to convert the induced strain into electrical signal. A small mass is mounted at the end of each beam in order to maximize the swing.

When the threshold acceleration is exceeded, the buckled bridge snaps through to the other equilibrium state. The transition between the two equilibrium positions generates an impulse-like excitation of the cantilever beams that vibrate freely at their resonant frequency independently of the input frequency.

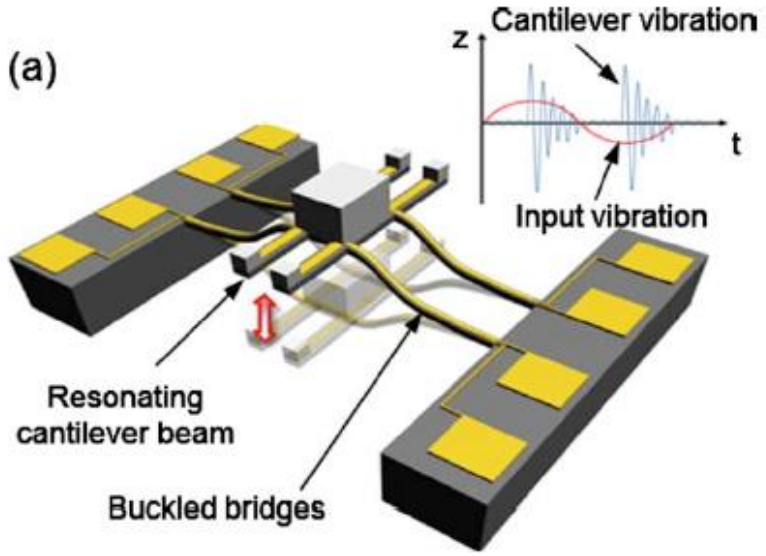


Figure 2-1: (a) Schematic view of proposed energy-harvesting device. (b) Photograph of device and experimental setup (Jung and Yun, 2010).

Figure 2-1 (cont'd)

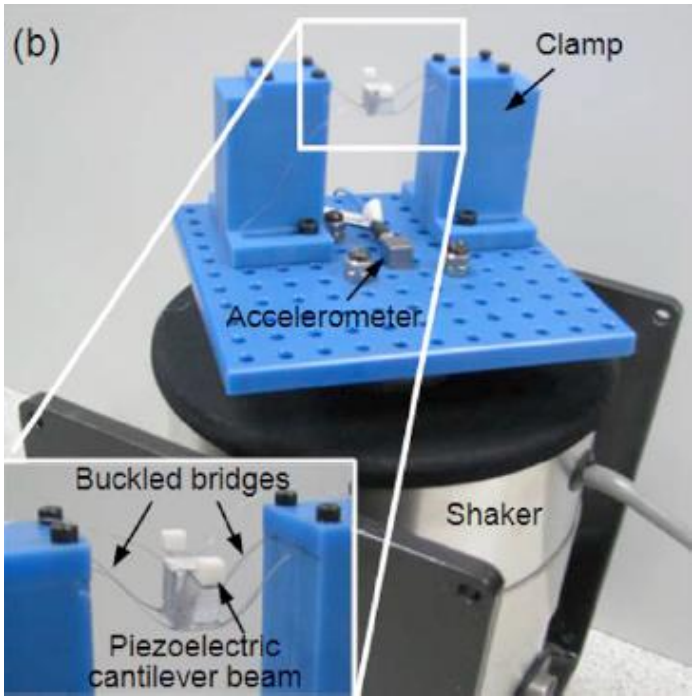


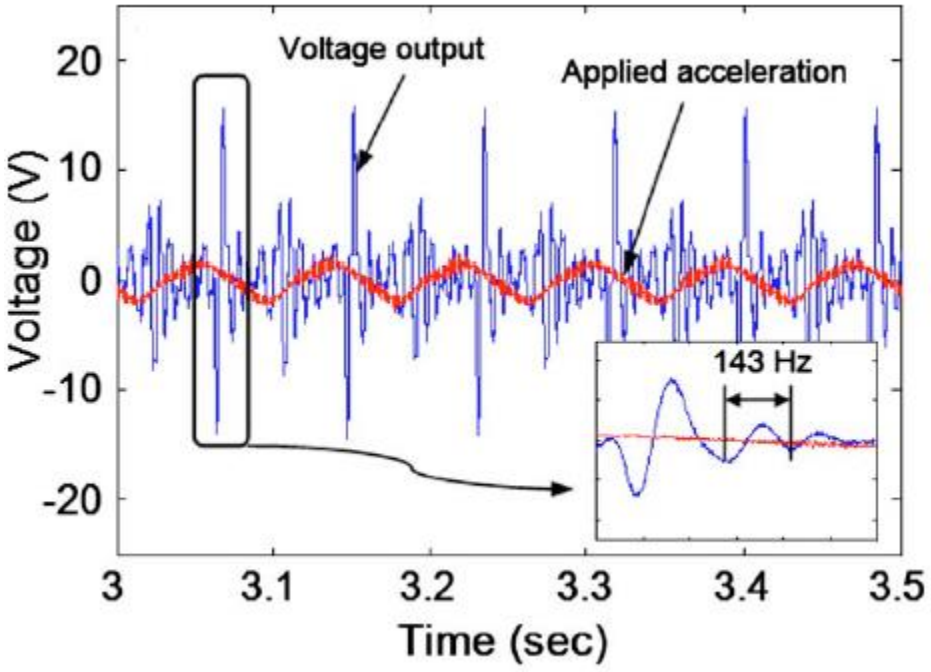


Figure 2-2: Resonance test results of the fabricated device (Jung and Yun 2010).

Figure 2-2 displays the frequency up-conversion characteristic of the device. The red line indicates the applied acceleration and the blue line represents the generated output voltage. Low frequency input vibration is converted into free and high-frequency output vibration. The input frequency is 12 Hz and the output frequency is 143 Hz. Transitions between the equilibrium positions occur at the positive and negative peaks of the input accelerations.

The proposed device exhibits a wide operational-frequency range. The snap-through motion of the buckled bridge structure occurs at various vibration input frequencies. However, the input acceleration should be high enough to obtain a snap-through motion. Figure 2-3 displays the frequency response determined experimentally by subjecting the device to harmonic excitations with different frequencies. The (acceleration$^2$/frequency) ratio was kept constant for all frequencies in order to apply same input power for all experiments. The frequency for maximum power output was approximately 30 Hz, which was much lower than the resonant frequency of the cantilever.

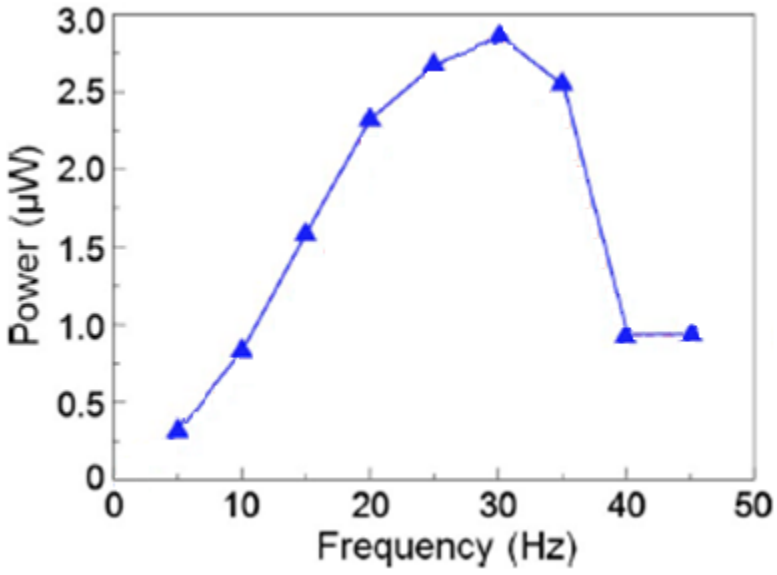


Figure 2-3: Frequency response for constant input power (Jung and Yun 2010).

Table 2-1 summarizes the experimental results for the device and a simple cantilever beam without the buckled bridge structure. The maximum output power generated by a single cantilever was 131 μW for the device at 30 Hz excitation. The average power was measured as 2.9 μW, which is significantly larger than the output power of 0.57 μW generated by a simple cantilever beam without buckled bridges. Output power amplification is due to the increase in the deflection magnitude of the cantilever beams caused by the snap-through accelerations of the bridge in addition to the base acceleration. The power generated by one of the device's cantilever beams is shown in Figure 2-4.

Table 2-1: Effect of the device on the output power.

| Parameter | Cantilever with buckled bridge | Simple cantilever without buckled bridge |
|---|---|---|
| Cantilever size ($mm^3$) | 8.0 × 4.0 × 0.2 | 8.0 × 4.0 × 0.2 |
| Resonant frequency (Hz) | 143 | 124 |
| Maximum voltage (V) | 27.1 (at 30 Hz) | 4.13 (at 124 Hz) |
| Maximum power (μW) | 131 (at 30 Hz) | 2.37 (at 124 Hz) |
| Average power (μW) | 2.9 (at 30 Hz) | 0.57 (at 124 Hz) |

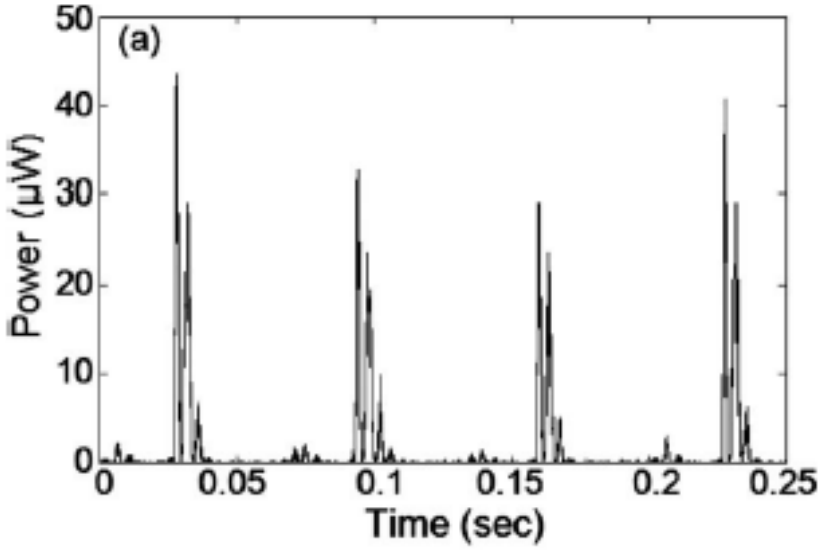


Figure 2-4: Power output generated by a single cantilever beam (Jung and Yun 2010).

## 2.3. Buckling analysis

The buckling problem of a fixed-fixed beam subjected to axial load was studied by Nayfeh and Emam (2004). The governing equation of a fixed-fixed straight beam subjected to axial load P accounting for midplane stretching is given by

$$\psi^{iv} + P\psi'' - \frac{1}{2}\psi'' \int_0^1 \psi'^2 dx = 0 \tag{2-1}$$

$$\psi = 0 \quad \text{and} \quad \psi' = 0 \quad \text{at} \quad x = 0 \ \text{and} \quad x = 1 \tag{2-2}$$

where $\psi(x)$ denotes the static buckled configuration associated with the load P and the prime denotes differentiation with respect to x. Since the integral in Equation (2-1) is a constant for a given $\psi(x)$, the buckling equation can be reduced into

$$\psi^{iv} + \lambda^2 \psi'' = 0 \tag{2-3}$$

where $\lambda^2 = P - 1/2 \int_0^1 \psi'^2 dx$ is a constant that represents the critical buckling load.

Equation (2-3) is a fourth order ordinary differential equation with constant coefficients. Its general solution is given by

$$\psi(x) = c_1 + c_2 x + c_3 \cos(\lambda x) + c_4 \sin(\lambda x) \tag{2-4}$$

where the $c_i$ are constants. Applying the boundary conditions (2-2) yields the following four algebraic equations

$$c_1 + c_3 = 0 \tag{2-5}$$

$$c_2 + \lambda c_4 = 0 \tag{2-6}$$

$$c_1 + c_2 + c_3 \cos\lambda + c_4 \sin\lambda = 0 \tag{2-7}$$

$$c_2 - \lambda c_3 \sin\lambda + c_4 \lambda \cos\lambda = 0 \tag{2-8}$$

This system of equations represents an eigenvalue problem for λ. Computing the determinant of the coefficient matrix and equating it to zero, the characteristic equation for $\lambda$ is given by

$$2 - 2\cos\lambda - \lambda \sin\lambda = 0 \tag{2-9}$$

Manipulating Equation (2-9) using trigonometric identities, the characteristic equation is simplified into

$$\sin\frac{\lambda}{2}\left(\sin\frac{\lambda}{2}-\frac{\lambda}{2}\cos\frac{\lambda}{2}\right)=0 \tag{2-10}$$

Solving the characteristic Equation (2-10) results in two kinds of buckling modes: symmetric and antisymmetric. Symmetric modes are extracted by solving $\sin\lambda/2=0$ . They can be expressed by

$$\psi(x)=1-\cos\lambda\, x \tag{2-11}$$

where $\lambda=2m\pi,\ m=1,2,\ldots$ and antisymmetric modes are extracted by solving $\tan\lambda/2=\lambda/2$. Their expression is given by

$$\psi(x)=1-2x-\cos\lambda\, x+\frac{2}{\lambda}\sin\lambda\, x \tag{2-12}$$

where $\lambda=2.86\pi, 4.92\pi, 6.94\pi, 8.95\pi, \ldots$

## 2.4. Post-buckling response of a bilaterally constrained beam

The post-buckling response of a straight prismatic bilaterally constrained beam has been theoretically studied by Chai (1998) using small and large deformation assumptions. The beam is placed between two flat rigid walls separated by a distance $h_0$ such that it lies along the surface of one of the walls. Both of its ends are clamped. The elastica has a length $L_0$, thickness t, width b and Young's modulus E. The net gap between the beam and the lateral constraints is denoted h and is defined as $h=h_0-t$. Under axial end shortening Δ, the beam buckles. The fourth-order linearized differential equation for an Euler beam under axial compression is given by

$$y''''+k^2y''=0,\quad k^2=\frac{P}{EI} \tag{2-13}$$

where a prime denotes differentiation with respect to x, y is the transverse deflection, P is the compression force and I is the moment of inertia of the beam.

### *2.4.1. Pre-contact*

After buckling the beam separates from the adjacent constraint. The mid-span rise, A, increases with Δ until touching the opposite wall. Subjected to the following boundary conditions

$$y(0) = y'(0) = y(L_0) = y'(L_0) = 0, \tag{2-14}$$

the solution to Equation (2-13) is given by

$$y(x) = \frac{A}{2}(1 - \cos kx) \tag{2-15}$$

Note that the first critical buckling load for the Euler buckling problem of fixed-fixed beams is defined as

$$P_{cr} = \frac{4\pi^2 EI}{L_0^2} \tag{2-16}$$

A normalized square-root axial force parameter $\zeta$ is introduced as follows

$$\zeta \equiv \sqrt{\frac{P}{P_{cr}}} = \frac{kL_0}{2\pi} \tag{2-17}$$

In the Pre-contact configuration the post-buckling load is defined by $\zeta = 1$. Therefore the deflected shape of Equation (2-15) becomes

$$y(x) = \frac{A}{2}\left(1 - \cos\frac{2\pi x}{L_0}\right) \tag{2-18}$$

The total end shortening is given by

$$\Delta = \frac{P}{Ebt} L_0 + \int_0^{L_0/2} (y')^2 dx \tag{2-19}$$

Using Equations (2-13) and (2-16)-(2-19) the midspan rise A can be expressed as

$$A = \frac{2t}{\sqrt{3}} \sqrt{\eta - 1}, \quad 1 \le \eta \le 1 + 0.75\tilde{h}^2 \tag{2-20}$$

where

$$\tilde{h} \equiv \frac{h}{t} \quad \text{and} \quad \eta \equiv \frac{3L_0\Delta}{(\pi t)^2} \tag{2-21}$$

*2.4.2. Point contact*

Subjected to an increased axial displacement the beam touches the opposite wall at its midspan. The boundary conditions for the free standing segment are

$$y(0) = y'(0) = y'(L_0/2) = 0, \quad y(L_0/2) = h \tag{2-22}$$

Applying these boundary conditions to Equation (2-13) and using Equations (2-19) and (2-21), transverse displacement and normalized end shortening are expressed, respectively, as

$$\frac{y}{h} = \frac{\sin\left(\frac{\pi\zeta\bar{x}}{n}\right) - \frac{\pi\zeta\bar{x}}{n} + \left(1 - \cos\left(\frac{\pi\zeta\bar{x}}{n}\right)\right)\tan\left(\frac{\pi\zeta}{2n}\right)}{2\left(\tan\left(\frac{\pi\zeta}{2n}\right) - \frac{\pi\zeta}{2n}\right)} \tag{2-23}$$

$$\eta = \zeta^2 + 0.75\tilde{h}^2 \frac{\left(\zeta^2\left(2 + \frac{1}{\cos^2\left(\frac{\pi\zeta}{2n}\right)}\right) - \frac{6n\zeta}{\pi}\tan\left(\frac{\pi\zeta}{2n}\right)\right)}{\left(\tan\left(\frac{\pi\zeta}{2n}\right) - \frac{\pi\zeta}{2n}\right)^2} \tag{2-24}$$

where n denotes the number of buckles in the beam and $\bar{x} \equiv x/(L_0/2)$.

### *2.4.3. Line contact*

It was assumed that a line contact develops over three segments situated at the ends and the midspan of the beam. Taking into account the vanishing of the bending moment along the contact zones, the independent boundary conditions for the free standing segment of length H are

$$y(0) = y'(0) = y''(0) = y'(H) = 0, \quad y(H) = h \tag{2-25}$$

The solution to Equations (2-13) and (2-25) is

$$\frac{y}{h} = \frac{2\pi\bar{x} - \sin(2\pi\bar{x})}{2\pi}, \quad 0 \le \bar{x} \equiv x/H \le 1 \tag{2-26}$$

with $H/L_0 = 1/\zeta$.

Using Equations (2-19) and (2-26) the relationship between the normalized axial load, $\zeta$, and end shortening, $\eta$, is given by

$$\eta = \zeta^2 + \frac{9n\tilde{h}^2}{2\pi^2}\zeta \tag{2-27}$$

### *2.4.4. Mode transition*

Further increase of the axial end shortening, $\Delta$, results in increasing the contact zones lengths until the longer flat segment buckles. Let a and b denote the lengths of the flat segments at the ends of the beam and c denote the length at its midspan. From geometric compatibility

$$a + b + c + 2H = L_0 \tag{2-28}$$

Substituting $H/L_0$ by $1/\zeta$ in Equation (2-28) yields

$$\frac{a+b+c}{L_0} = 1 - \frac{2}{\zeta} \tag{2-29}$$

The load at which mode transition occurs was assumed to be bounded between a lower limit corresponding to a single contact zone and an upper limit corresponding to equi-length contact zones. The lower load limit is determined by eliminating the lengths a and b in Equation (2-29) and using Equation (2-17) as

$$\frac{kc}{2\pi} = \zeta - 2 \tag{2-30}$$

The upper limit corresponds to the case where $a = b = c$. Therefore Equation (2-29) is reduced into

$$\frac{kc}{2\pi} = \frac{\zeta - 2}{3} \tag{2-31}$$

Guided by experimental observations, and due to the absence of friction, it was assumed that the most probable configuration corresponds to the symmetric configuration with $2a = 2b = c$. In this case Equation (2-29) reduces to

$$\frac{kc}{2\pi} = \frac{\zeta - 2}{2} \tag{2-32}$$

The flat segment of length c can be considered as Euler beam with fixed ends. Therefore, similar to Equation (2-17), the buckling critical load is such that $kc/2\pi = 1$. From Equations (2-30) - (2-32), the transition to the second mode is bounded in the range $3 \leq \zeta \leq 5$. The symmetric buckling occurs at $\zeta = 4$.

*2.4.5. Multiple buckles*

When the beam has multiple buckles, the buckling configuration can be either a point or a line contact. The length and the end-to-end shortening of each free standing segment of the beam, denoted, respectively, by H and $\Delta_H$, are given by

$$H = \frac{L_0}{2n} \quad \text{and} \quad \Delta_H = \frac{\Delta}{2n} \tag{2-33}$$

where n denotes the total number of buckles in the buckled configuration. The deflection of each segment and the total end shortening for the point contact configuration are given, respectively, by Equations (2-23) and (2-24). The transition from a point to a line contact takes place at $\zeta = 2n$. The results for the symmetric line contact configuration are given by Equations (2-26) and (2-27). Loads at transitions to higher buckling modes are bounded by $1 + 2n \leq \zeta \leq 1 + 4n$. Symmetric buckling transitions occur at $\zeta = 4n$. In this case, Equation (2-28) is reduced to

$$2n(c + H) = L_0 \tag{2-34}$$

The relationship between the contact zone and the load is determined by multiplying both side of Equation (2-34) by $k/2\pi$ and is given by

$$2n\frac{c}{L_0} = 1 - \frac{2n}{\zeta}. \tag{2-35}$$

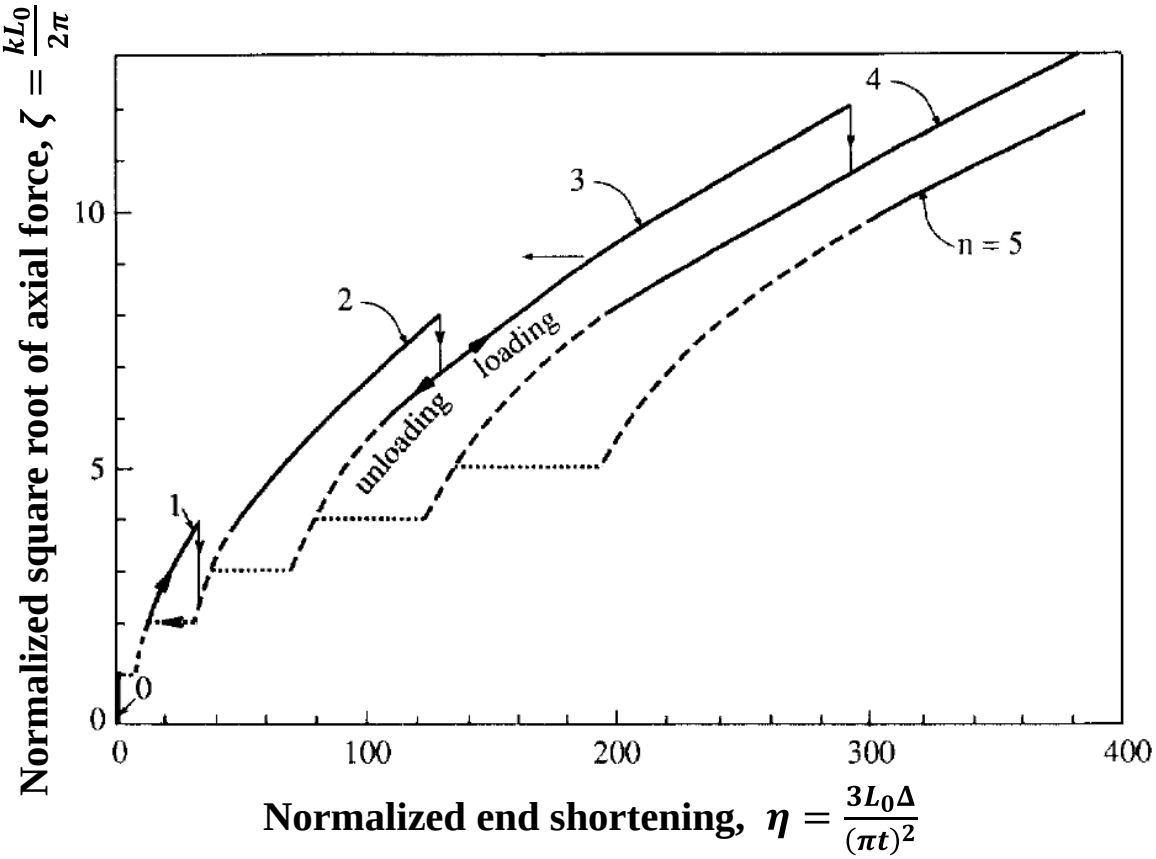


Figure 2-5: The normalized square root axial load, ζ, vs the normalized end shortening, η (Chai 1998).

Figure 2-5 shows the variation of the normalized load, $\zeta$, with respect to the normalized end shortening, $\eta$. The results shown in the figure were constructed for $\tilde{h} = 3$. The dashed and the solid lines correspond to the point contact and the line contact configurations, respectively. Following buckling, $\zeta$ remains fixed until the beam touches the opposite constraint. The point contact holds up to $\zeta = 2$. Then a line contact develops and increases until the beam snaps into two buckles at $\zeta = 4$. During transition the force drops and the end shortening remains fixed. The next mode transition (i.e. to n = 3) occurs at $\zeta = 8$, and so forth. The response of the beam depends

on the loading direction. If the beam is unloaded rather than loaded, it returns to a lower buckling mode through a different path.

## 2.5. Contact between an elastica and its boundary involving friction

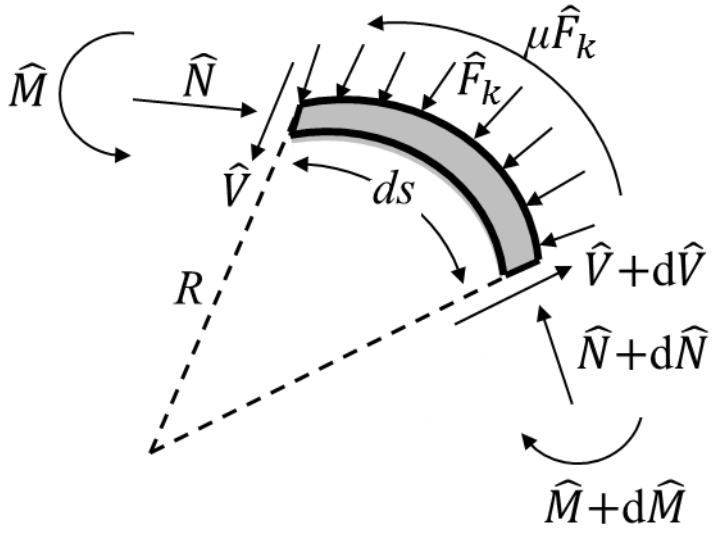


Figure 2-6: Equilibrium of a beam element subjected to lateral pressure with friction.

Soong and Choi (1986) presented a theoretical formulation of the friction force generated by the dry contact between the buckled beam and the lateral rigid walls. The beam is modeled using Euler Bernoulli beam theory and Coulomb model is used for friction. Figure 2-6 displays the force equilibrium of a buckled beam element subjected to normal pressure and tangential friction force where $\widehat{\mathrm{M}}$ is the bending moment, $\widehat{\mathrm{N}}$ is the axial compressive force, $\widehat{\mathrm{V}}$ is the transverse shear force, $\widehat{\mathrm{F}}_{\mathrm{n}}$ is the normal pressure force, $\mu_{\mathrm{k}}$ is the coefficient of friction, $ds$ is the arc length of the element, and $R$ is the local radius of curvature for the deformed beam.

The beam under consideration is homogeneous, uniform and elastic with constant bending stiffness *EI*. The Euler–Bernoulli equation describes the dependence of the local radius of curvature, bending moment and transverse shear to the beam's deflection $\widehat{\omega}$ as

$$\frac{1}{R} = \frac{d^2\widehat{\omega}}{ds^2} \tag{2-36 a}$$

$$\widehat{M} = EI\frac{d^2\widehat{\omega}}{ds^2} \tag{2-36 b}$$

$$\widehat{V} = EI\frac{d^3\widehat{\omega}}{ds^3} \tag{2-36 c}$$

From the equilibrium of tangential and normal forces the normal and tangential pressure at the contact zone are expressed as follows

$$\widehat{F}_k = \frac{\widehat{N}}{R} + \frac{d\widehat{V}}{ds} \tag{2-37}$$

$$\mu_k\widehat{F}_k = \frac{\widehat{V}}{R} - \frac{d\widehat{N}}{ds} \tag{2-38}$$

Substituting Equations (2-36) into (2-37) and (2-38) yields

$$\widehat{F}_k = \widehat{N}\frac{d^2\widehat{\omega}}{ds^2} + EI\frac{d^4\widehat{\omega}}{ds^4} \tag{2-39}$$

$$\mu_k\widehat{F}_k = EI\frac{d^3\widehat{\omega}}{ds^3}\frac{d^2\widehat{\omega}}{ds^2} - \frac{d\widehat{N}}{ds} \tag{2-40}$$

Combining Equations (2-39) and (2-40), the variation of the axial compression force is governed by the following ordinary differential equation

$$\frac{d\widehat{N}}{ds} + \mu_k N \frac{d^2\widehat{\omega}}{ds^2} = EI\left(\frac{d^3\widehat{\omega}}{ds^3}\frac{d^2\widehat{\omega}}{ds^2} - \mu_k \frac{d^4\widehat{\omega}}{ds^4}\right) \tag{2-41}$$

The solution $\widehat{N}$ to Equation (2-41) can be expressed as

$$\widehat{N} = e^{-\int_{s_0}^{s} f(\tau)\, d\tau}\left(\widehat{N}_{s=s_0} + \int_{s_0}^{s} g(\xi)\, e^{\int_{\xi_0}^{\xi} f(\tau)\, d\tau}\, d\xi\right) \tag{2-42}$$

where

$$f(s) = \mu_k \frac{d^2\widehat{\omega}}{ds^2} \tag{2-43}$$

$$g(s) = EI\left(\frac{d^3\widehat{\omega}}{ds^3}\frac{d^2\widehat{\omega}}{ds^2} - \mu_k \frac{d^4\widehat{\omega}}{ds^4}\right) \tag{2-44}$$

Substituting Equation (2-42) into (2-40), the tangential friction force is expressed by

$$\mu_k \widehat{F}_n = \mu_k\left[e^{-\int_{s_0}^{s} f(\tau)\, d\tau}\left(\widehat{N}_{s=s_0} + \int_{s_0}^{s} g(\xi)\, e^{\int_{\xi_0}^{\xi} f(\tau)\, d\tau}\, d\xi\right)\frac{d^2\widehat{\omega}}{ds^2} + EI\frac{d^4\widehat{\omega}}{ds^4}\right] \tag{2-45}$$

## 2.6. Summary

Energy harvesting using snap-through buckling for mechanical frequency up-conversion has been proposed by Jung and Yun (2010). The proposed device consists of buckled slender bridges with a proof mass to provide inertial excitation force and cantilever beams to harvest free vibration energy. Snap-through transitions between the equilibrium positions of the buckled bridges allows for frequency up-conversion. It was shown that the device harvests power over a wide frequency range. However, the input excitation has to be a vibration with accelerations high enough to activate snap-through motion.

The eigenvalue buckling analysis of a uniform fixed-fixed straight beam subjected to axial loading results in two kinds of solutions: symmetric and antisymmetric modes. Therefore, for the post-buckling analysis, if the contact between the beam and the lateral constraints involves friction, all the modes have to be included in the analysis. However, antisymmetric modes can be neglected if the contact is frictionless and the load distribution is symmetric.

The post-buckling behavior of a bilaterally constrained beam under axial loading was investigated by Chai (1998). The contact was assumed frictionless and the transitions to a higher buckling mode were assumed to be always bounded between a lower limit, corresponding to a single flattened contact zone, and an upper limit, corresponding to multiple flattened contact segments of equal lengths. The force-displacement response of the beam was investigated assuming that the buckling configuration is always symmetric.

A study of the contact problem between a beam and its boundary was carried out by Soong and Choi (1986). The contact formulation involves friction. The normal pressure as well as tangential force at the contact zones were determined. It was shown that, due to friction, the axial compression force inside the beam is not constant.

# CHAPTER 3: EXPERIMENTAL AND NUMERICAL STUDIES OF THE POST-BUCKLING RESPONSE OF BILATERALLY CONSTRAINED BEAMS UNDER AXIAL LOADING [1]

## 3.1. Overview

This chapter presents experimental and numerical studies of the post-buckling response of one and multiple parallel bilaterally-constrained beams. Section 3.1 deals with the response of one beam. An experimental apparatus was built and tested to provide better understanding of the post-buckling behavior of the beam and to assess its repeatability under cyclic loading events with different input frequencies. A finite element (FE) model was developed to extract information on the transverse accelerations generated during mode jumping and investigate the effect of the system's parameters on the beam's response. In order to control the number and the spacing between the snap-through events, multiple slender beams can be stacked, in parallel or series configurations, into a system. Section 3.3 explores the post-buckling response of multiple bilaterally constrained beams combined in a parallel configuration. The experimental setup and the FE model developed for one beam were extended to accommodate three parallel equi-length beams with fixed end supports. The effect of the system's parameters on the post-buckling response of the beams and the generated accelerations was studied. The impact of changing the thicknesses of the beams is investigated numerically and experimentally. However, other

[1] The presented results in this chapter were published in Lajnef et al. (2012 and 2014a) and Borchani et al. (2013)

parameters, such as Young's modulus and gaps between the walls, are only investigated numerically.

## 3.2. Post-buckling response of one bilaterally constrained beam

The multistable post-buckling response of an axially loaded elastic element can be obtained and controlled by providing appropriate lateral constraints to the buckling element so as to allow multiple stable equilibrium configurations. In such conditions, the increased transverse deformations from a buckled shape under axial compressive demands lead to contact interaction with discrete or continuous boundaries. The contact interaction generates secondary restraining forces that induce the development of a higher order buckling configuration. Increased transverse deformations of the second post-buckled configuration lead to new transverse forces from the lateral constraints, thus inducing a third post-buckled stable configuration, and so forth.

### *3.2.1. Experimental study*

The snap buckling, or mode jumping, characteristics of the post-buckling response of a bilaterally constrained beam was experimentally investigated. A polycarbonate beam with fixed end supports was placed between rigid continuous bilateral plexiglass frame as shown in Figure 3-1. The optically clear plexiglass acrylic frame was chosen to be 1 inch thick and was designed to have a gap, $h_{0,}$ of 4 mm for transverse deformations. The walls were constrained at the bottom and top to avoid opening of the wall gap during testing. The beam was placed inside the gap, adjacent to one of the constraining walls. The net gap, h, for traverse deformations of the beam is the difference between the wall gap, $h_0$, and the beam thickness, t. The geometry and material properties of the used polycarbonate beam are detailed in Table 3-1.The testing procedure consisted in applying a gradually increasing compressive load under displacement control to the

top of the beam using a mechanical test system (MTS model Flextest 40 with series 370 load unit) as shown in Figure 3-1.

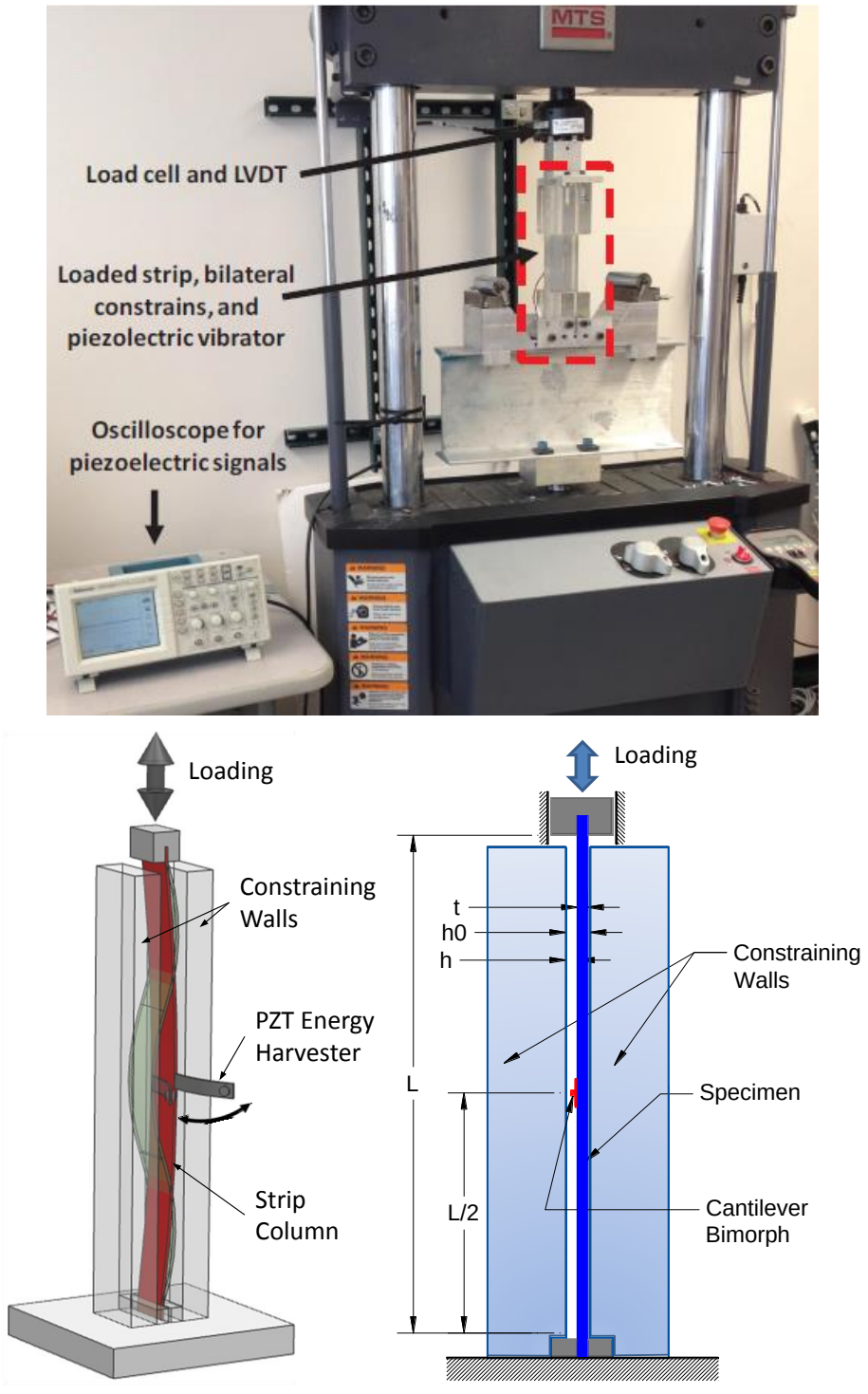


Figure 3-1: Schematic and diagrams of the test setup.

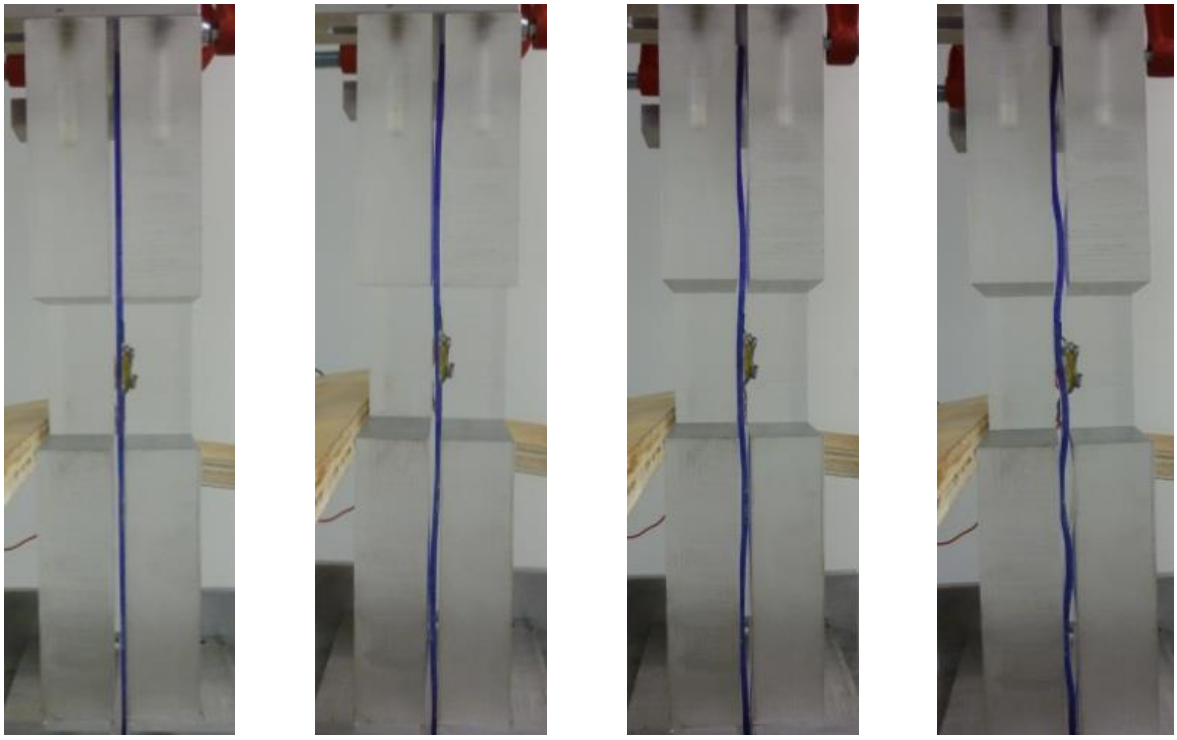

(a) Mode 1 -Φ1 (b) Mode 3 - Φ3 (c) Mode 5 - Φ5 (d) Mode 7 - Φ7

Figure 3-2: Views of the loaded beam showing the obtained multiple stable post-buckled configurations.

The applied axial load induces multistable post-buckling configurations, as shown by the experimental mode shapes in Figure 3-2. The post-buckling branch switching effect can be seen by the discontinuities (load drops) in the force-deformation response (applied force versus the top vertical displacement) plotted in Figure 3-3. The figure labels (Φ3, Φ5, etc.) indicate the buckling mode shape to which the beam transitions after the snap-through event. Each of the mode transitions represents the switch between a stable equilibrium branch to another that reduces the total potential energy in the system. The stable branches are associated with an eigenvector or buckling mode, and a branch switch constitutes a global unstable transition or a snap-through event.

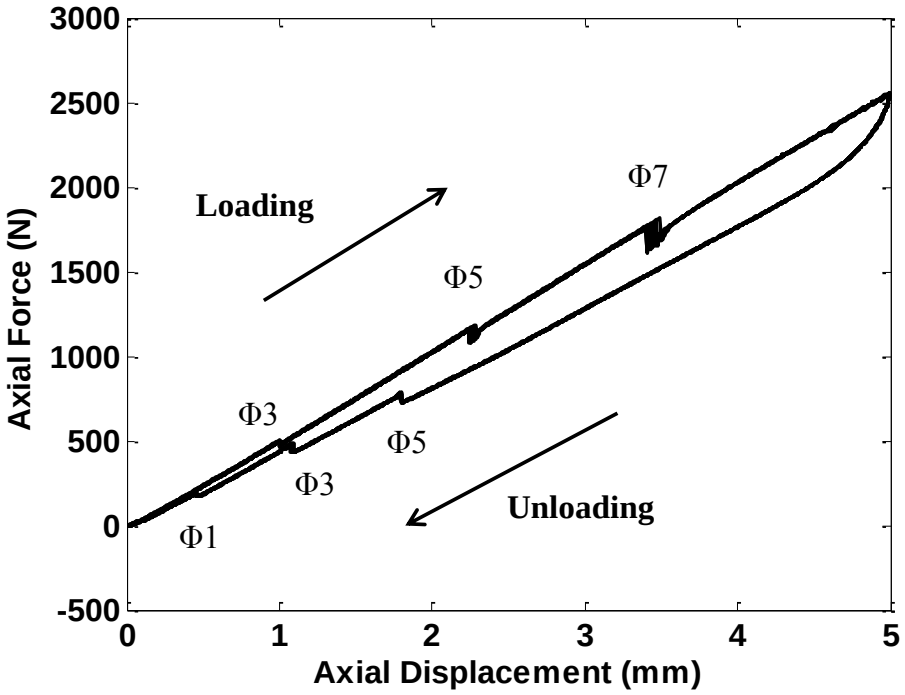


Figure 3-3: Force-displacement response for 10-cycle compression test.

To evaluate the repeatability of the post-buckling behavior and to assess its cyclic response, the bilaterally constrained beam setup was subjected to a series of displacement-controlled unidirectional compression tests. For all runs, the beam was compressed past its 7$^{th}$ buckling mode then unloaded until a zero stress state was reached. The force-displacement responses for 10 different loading cycles are displayed in Figure 3-3. The total duration of the loading/unloading cycles was set at 20 seconds, which represents a displacement rate of 0.5 mm/s. It can be seen that all of the response curves coincide, with small deviations observed at the higher transition points for modes 5 and 7.

The dependency of the beam's post-buckling response to the frequency of the input axial forces (loading rate) was also evaluated by a second set of displacement-controlled cyclic loading

tests. Tests were conducted at 0.16, 0.05, 0.025 and 0.006 Hz (i.e., 6, 20, 40 and 150 second cycle periods). Ten-cycle tests were performed for each input frequency. Figure 3-4 displays the mean force-displacement response of the beam for each frequency. It can be noticed that the input frequency had little influence on the beam post-buckling response. The post-buckling response curves are superposed and the transition points are very close. The distribution of all the transition points is presented in Figure 3-5. The transition points for each individual mode are within a relatively small range of displacement and force values. Table 3-2 summarizes the mean and standard deviation values for the force and displacement at each mode transition. The displacement and force standard deviations at the transition points were lower than 3% and 5%, respectively. Therefore, it can be concluded that the beam post-buckling response is reproducible and independent of the load rate under the considered test conditions.

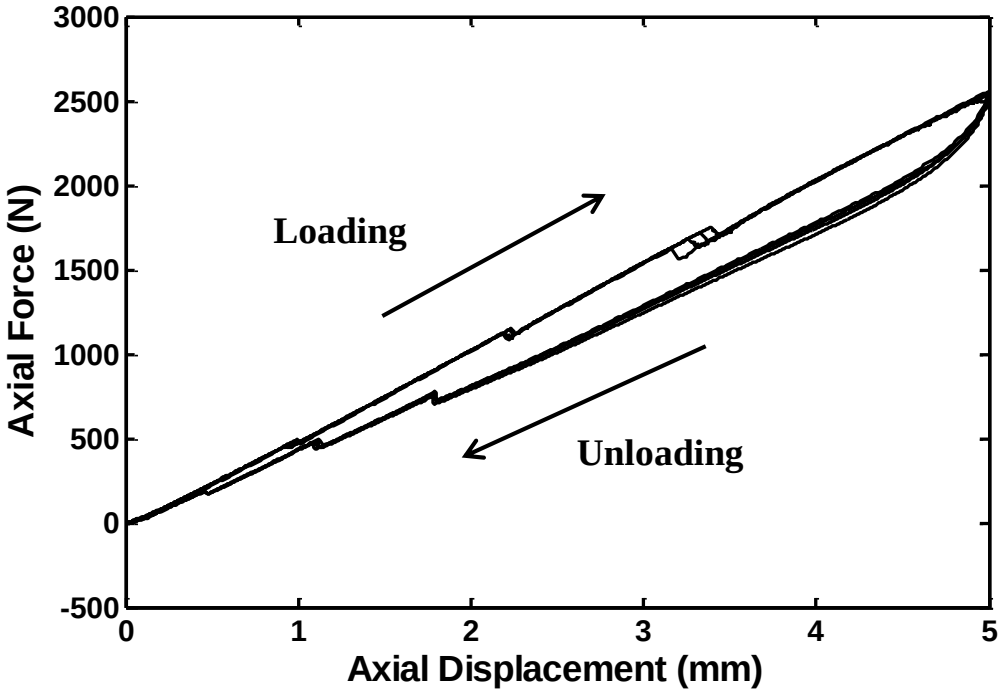


Figure 3-4: Post-buckling behavior for displacement control cyclic loading tests at 0.16 Hz, 0.05 Hz, 0.025 Hz and 0.006 Hz.

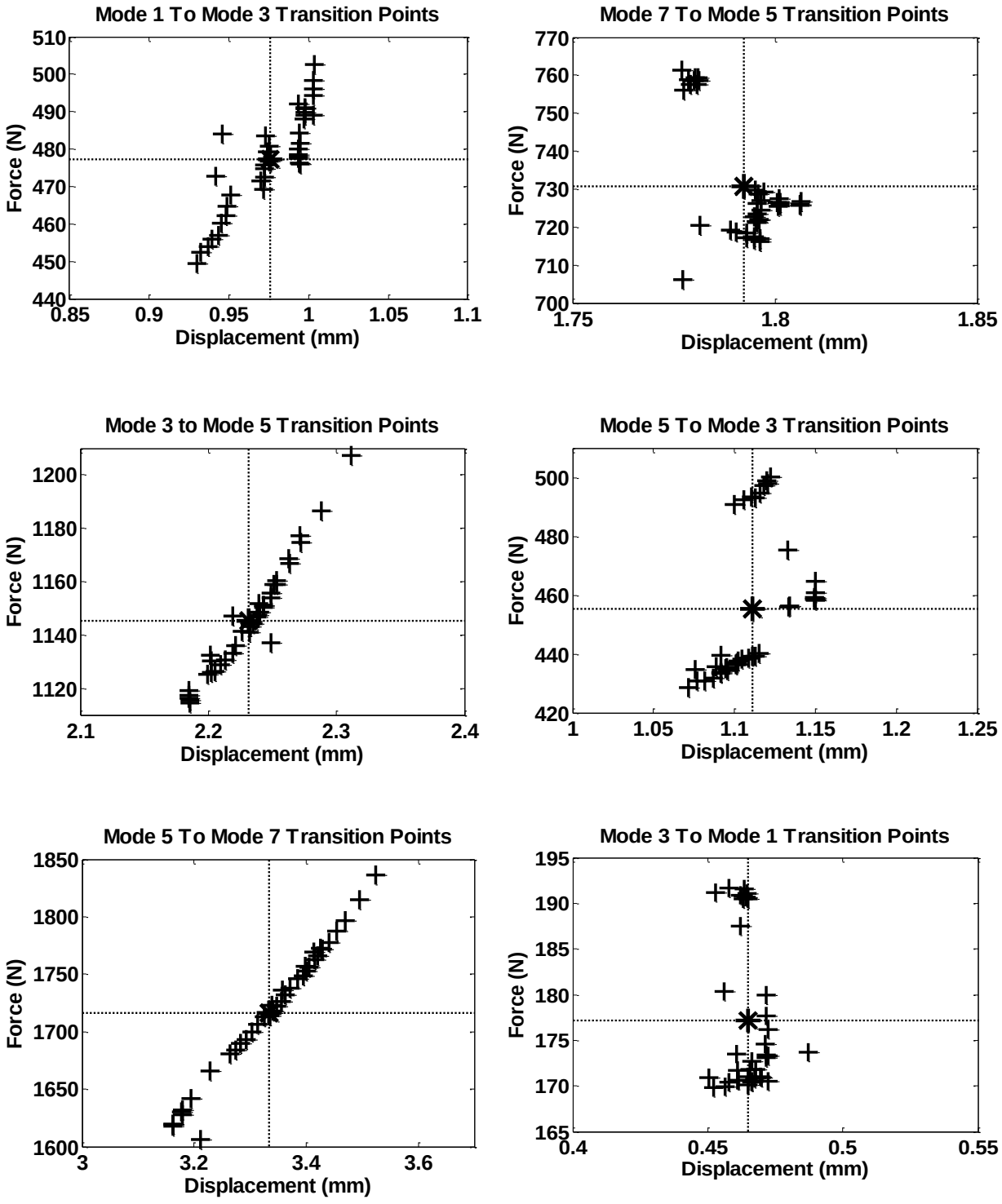


Figure 3-5: Transition points distribution.

Table 3-1: Mode transitions mean points and standard deviations.

| Mode Transition | Mean points | Standard deviations |
|---|---|---|
| | Displacement (mm), Force (N) | Displacement (mm), Force (N) |
| 1 to 3 | 0.97, 477.4 | 0.02, 13.3 |
| 3 to 5 | 2.23 , 1145.3 | 0.02, 20.4 |
| 5 to 7 | 3.33 , 1716.7 | 0.10, 59.8 |
| 7 to 5 | 1.79 , 730.8 | 0.01, 16.0 |
| 5 to 3 | 1.11 , 455.2 | 0.01 , 24.8 |
| 3 to 1 | 0.46 , 177.1 | 0.01 , 8.4 |

The effect of the interaction between the lateral constraints and the beam was experimentally investigated. The lateral rigid walls were replaced by two soft silicone blocks and the net gap between them remains the same. As the axial load increases, the pressure that the column applies on the walls increases forcing them to open the gap wider. The overall stiffness of the system drops as the loading increases. Figure 3-6 displays a comparison between the post-buckling response of the system with rigid and flexible walls. These results show that the shape of the force-displacement response curve as well as the dynamic response of the energy concentrators can be controlled.

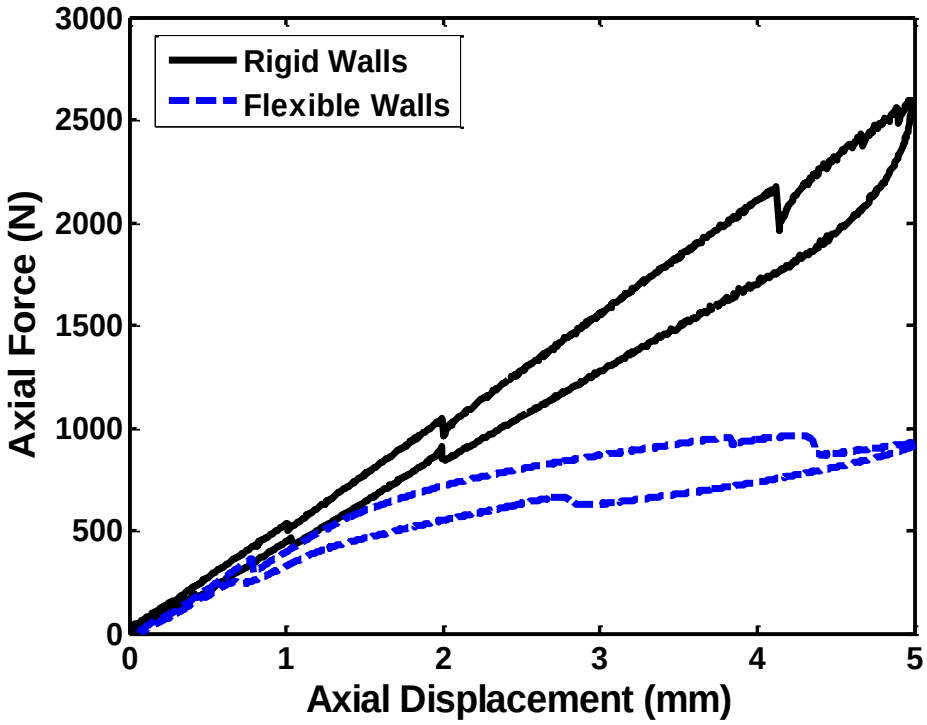


Figure 3-6: Comparison between the post-buckling response of the system with rigid and flexible walls.

### *3.2.2. Numerical study*

Small and large-deformation analytical models for predicting the force-deformation response of bilaterally constrained beams, including the identification of mode transition events, have been proposed by Chai (1998). However, the models neglect the friction between the wall and the beam and assume that the buckled configurations are symmetric. The models can adequately capture the system stiffness but the mode transitions are incrementally overestimated and the small deformation model becomes increasingly inaccurate as the number of buckled waves increases. Therefore, a finite element (FE) approach was chosen to provide further insight into the

beam's post-buckling behavior and extract information on the transverse acceleration generated during mode jumping, which determine the input to the piezoelectric energy harvester.

The numerical study was conducted using the general purpose finite element program ABAQUS. Large-strain nonlinear dynamic analyses were conducted using four-node isoparametric shell elements to model the beam and rigid no-penetration contact behavior with friction was defined for the interaction between the beam and the rigid side walls. Consideration of friction is important because this force creates a pseudo-softening effect on the load-deformation response since it acts against the direction of loading. Because shell elements have no physical thickness, the model of the test setup was such that the distance between the rigid walls was the net gap $h = h_0 - t$. To accommodate the seeding of initial imperfections for the large deformation analysis and to avoid interaction with the no-penetration rigid wall boundary, the location of the beam in the model was offset from the near wall by 5% of the net gap. Thus, the beam in the FE model had a gap of 0.05h to one side and 0.95h on the other. The element size was approximately 4 mm square and was chosen based on a sensitivity study. The friction coefficient between the wall and the beam surfaces was 0.2, chosen by calibration of the model with data from the noted test setup. Geometric imperfection was introduced to the beam by the superposition of buckling eigen modes. An implicit dynamic analysis procedure was used whereby a displacement amplitude history was prescribed to the top edge of the beam with a rate of 0.5 mm/sec.

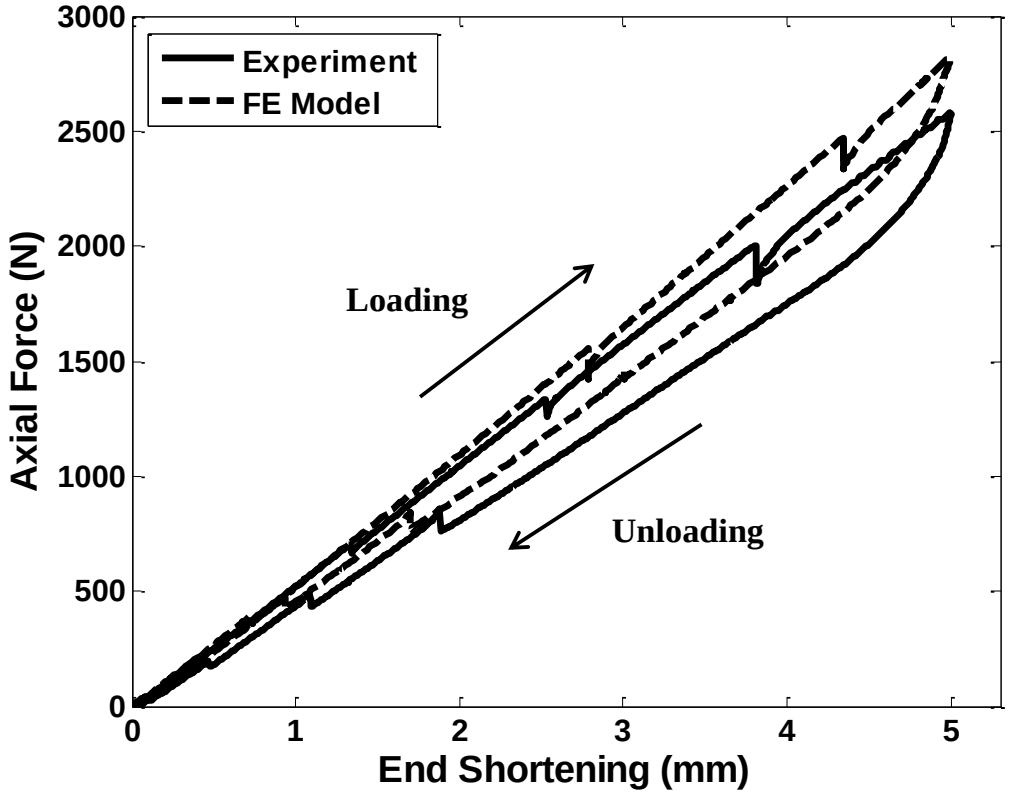


Figure 3-7: Comparison of experimental and simulated force-displacement responses of the bilaterally constrained beam.

The numerically simulated force-displacement response from the FE model is shown in Figure 3-7 together with the experimental data. It can be seen that the FE solution adequately resembled the experimental response by capturing the buckling mode transitions (both in force/deformation location and in the amount of energy loss, interpreted by the magnitude of the load drop), the loading and unloading stiffness, and the hysteretic nature of the response (induced by the friction between the beam and the walls). A comparison of the simulation and experimental post-buckling results is provided in Table 3-3. The finite element solution is considered acceptable given that parameters such as the actual values for the beam imperfection, friction coefficient and boundary conditions are unknown.

Table 3-2: Comparison of simulation post-buckling results with experimental data.

| Mode Transition | Experimental | | FEA | | | |
|---|---|---|---|---|---|---|
| | Disp. | Force | Disp. | | Force | |
| | (mm) | (N) | (mm) | % Diff. | (N) | % Diff. |
| 1 to 3 | 0.97 | 477.4 | 0.734 | -25 | 397.8 | -17 |
| 3 to 5 | 2.23 | 1145.3 | 2.785 | 25 | 1551.4 | 36 |
| 5 to 7 | 3.33 | 1716.7 | 4.346 | 30 | 2436.9 | 42 |
| 7 to 5 | 1.79 | 730.8 | 1.702 | -5 | 767.5 | 5 |
| 5 to 3 | 1.11 | 455.2 | 0.934 | -16 | 416.7 | -9 |
| 3 to 1 | 0.46 | 177.1 | 0.404 | -13 | 177.5 | 0 |

The buckled shapes obtained from the FE analysis are shown in Figure 3-8 with superposed contour maps for the transverse deformations. It can be seen that the modes correspond well with the experimentally observed buckling shapes shown in Figure 3-2. The asymmetric nature of the buckling shapes from the FE analysis, which follows from the friction between the beam and the wall, can be discerned by the nodal lines (lightest contour color). The post-buckling branch switching events of the beam during loading and unloading can also be seen in the trace of axial force vs. transverse mid-height displacement captured from the finite element solution for the experimentally evaluated system and shown in Figure 3-9. The horizontal lines in the trace represent the instantaneous transverse movements during branch switching or snap-through between post-buckled configurations. The labels note the buckled mode at the end of the unstable

branch and the annotations L and U denote if they correspond to the loading or unloading path, respectively.

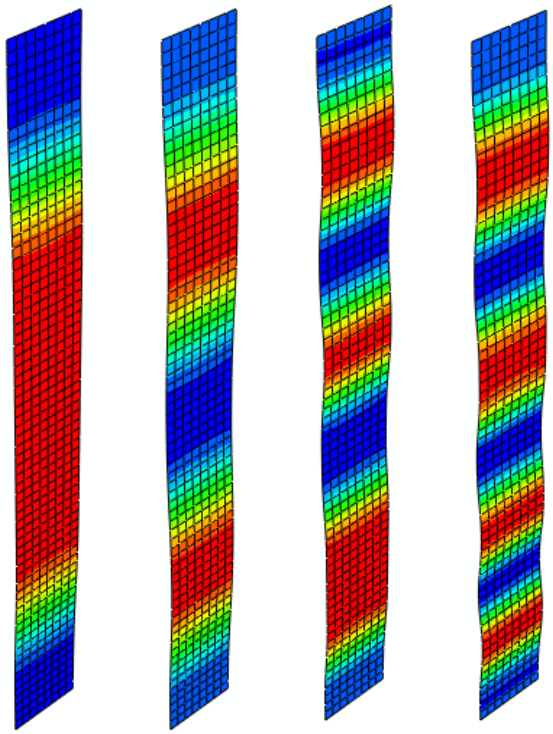

Φ1 Φ3 Φ5 Φ7

Figure 3-8: Buckled shapes from the finite element analysis of the experimentally evaluated system. The color contours represent transverse deformations with the yellow (lightest color) defining nodal lines.

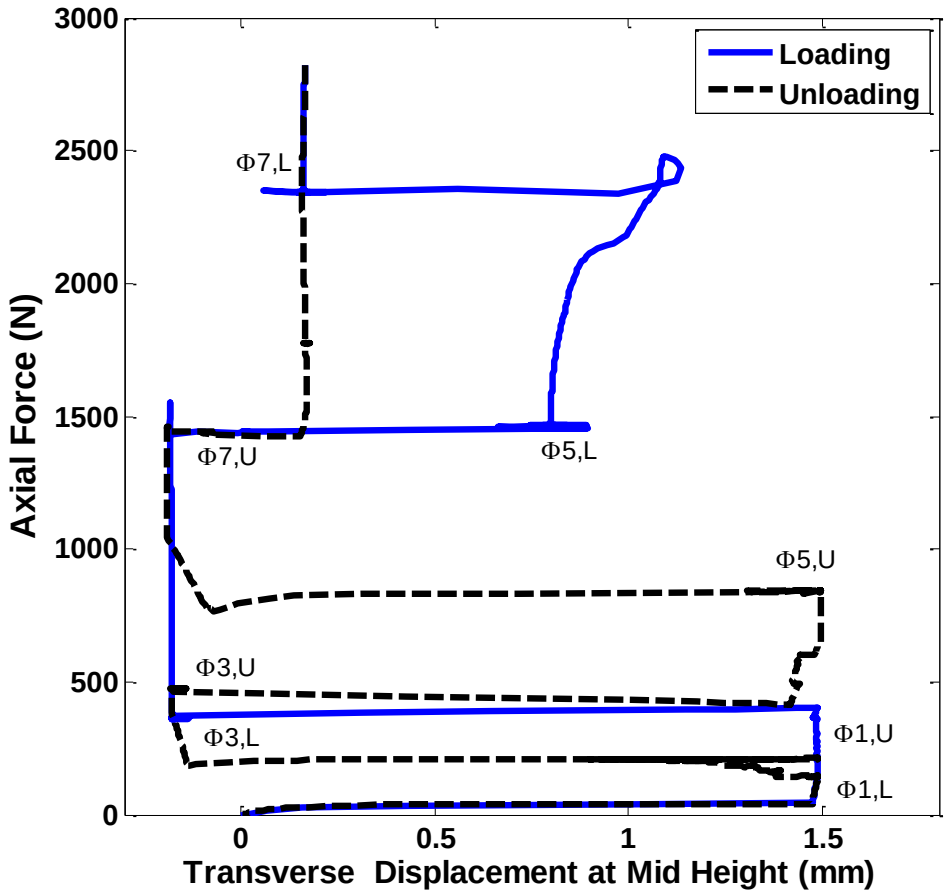


Figure 3-9: Trace of axial force vs. transverse mid-height displacement during a loading cycle indicating the post-buckling branch switching events.

Of more interest is the acceleration created by the impact of the beam on the rigid side walls as evidenced by the step-function-type response in Figure 3-10 where each vertical line is the result of a mode jump. Experimental measurements are shown in Figure 3-10 (a) while the values from the FE simulation are shown in Figure 3-10 (b). The acceleration created during the impact of the beam with the side wall creates an input to the energy harvester analogous to a step function. This effect dominates the input to the energy harvester and allows for the efficient frequency conversion of the quasi-static external input to the dynamic input for the harvester.

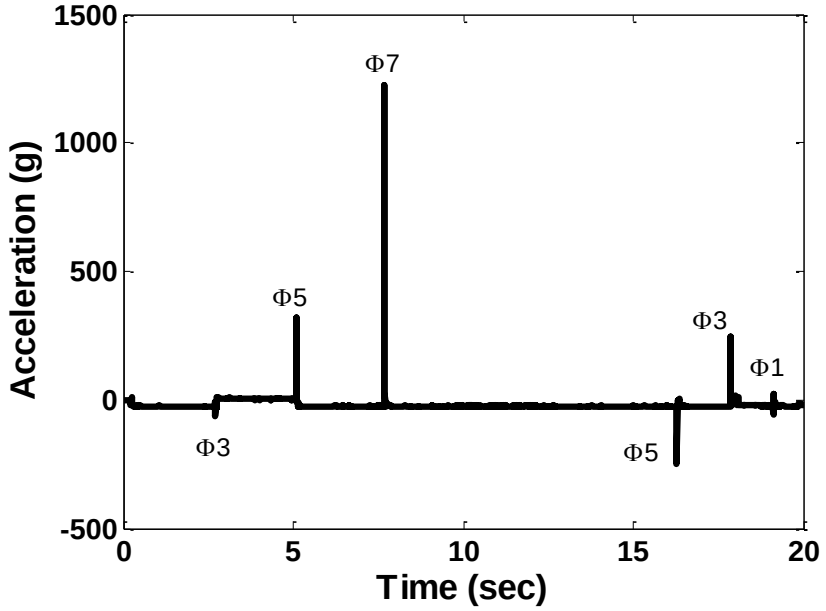


(a)

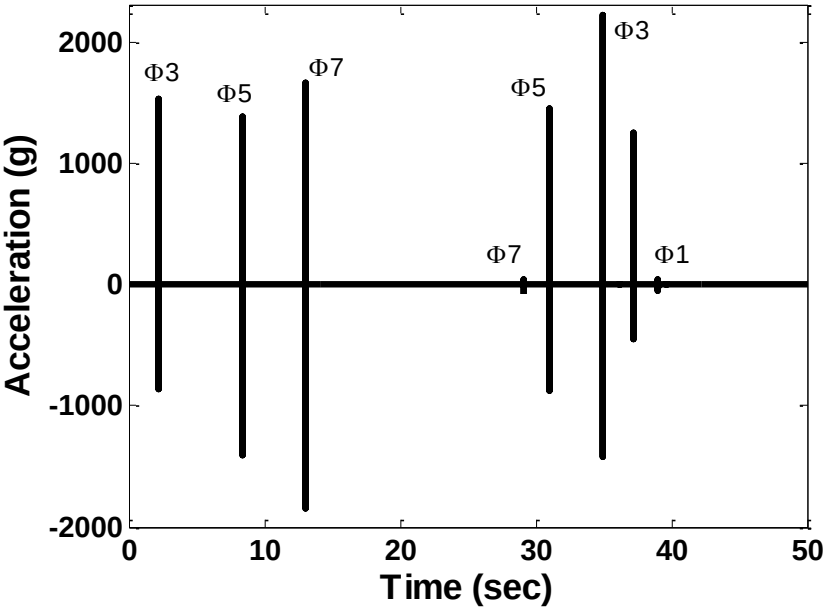


(b)

Figure 3-10: Acceleration generated from the multiple mode-jumping response of the axially loaded bilaterally constrained beam at mid-height of the beam during one loading cycle: (a) experiment, (b) finite element analysis. The labels Φ3 to Φ7 indicate the mode transition events.

The results from Figure 3-10 show that the side acceleration from the FE model for mode 7 during loading is only about 6% higher than the experimentally measured value. Discrepancies with the other mode jumps are attributed to the fact that the damping from the beam and the side wall in the experiment are not considered in the FE model.

As previously noted, the snap-through response between the equilibrium positions induces accelerations in the transverse direction of the beam upon its impact with the side walls. It has been stated that these accelerations define the input to the piezoelectric energy harvester. The ability of the FE modeling approach to capture the post-buckling response of the bilaterally constrained beam provides confidence that it can be used to evaluate the effect of system parameters (e.g., beam length, stiffness, thickness, etc.). Their effect on the energy harvesting capabilities is thus related to their effect on the generated accelerations during snap-through. A parametric study was thus performed based on the calibrated finite element model to study the effect of system parameters on the generated lateral acceleration from mode transitions. The considered parameters are the boundary conditions, position of the beam, elastic modulus, E, beam length, L, beam thickness, t, and gap between the constraining walls, $h_0$.

Table A.1 summarizes the cases considered in the study, where Case 1 is the base case previously presented in the experimental study. The remaining cases varied one or two parameters at a time as shown in bold text in table A.1. The beam width, b, and the coefficient of friction were, respectively, 30 mm and 0.2 for all cases.

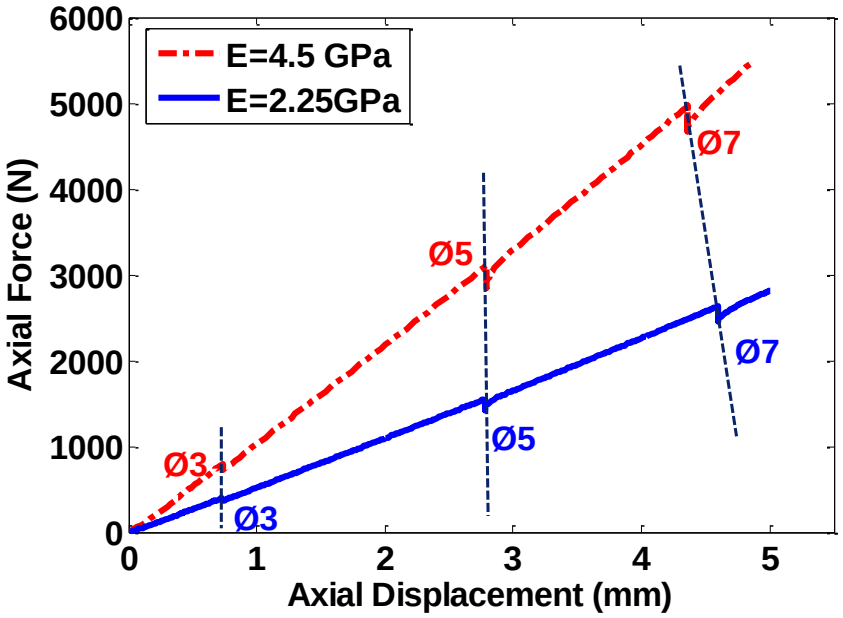


(a) Effect of Young's modulus.

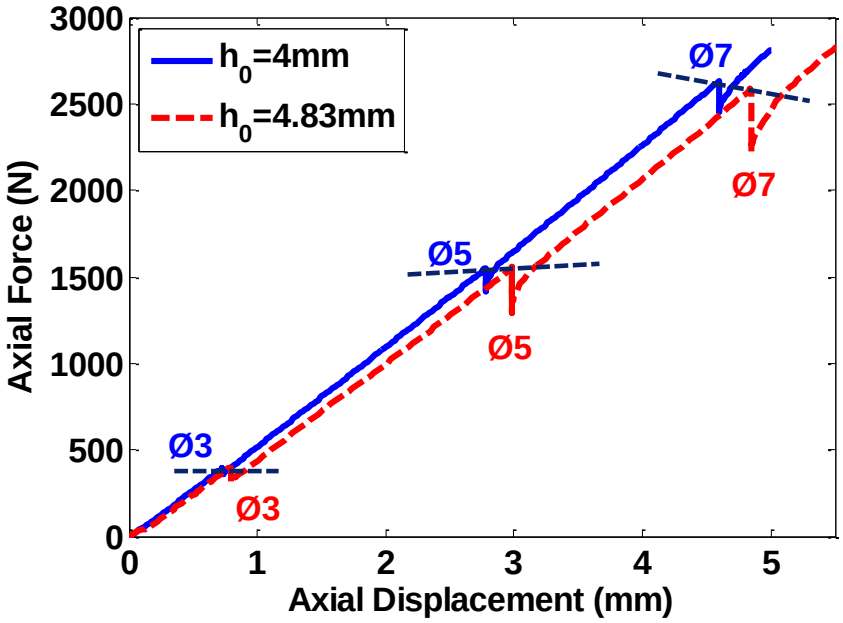


(b) Effect of the gap between the walls.

Figure 3-11: Effect of (a) Young's modulus, (b) walls gap and (c) beam's thickness on axial forces and displacements at snap-through transitions.

Figure 3-11 (cont'd)

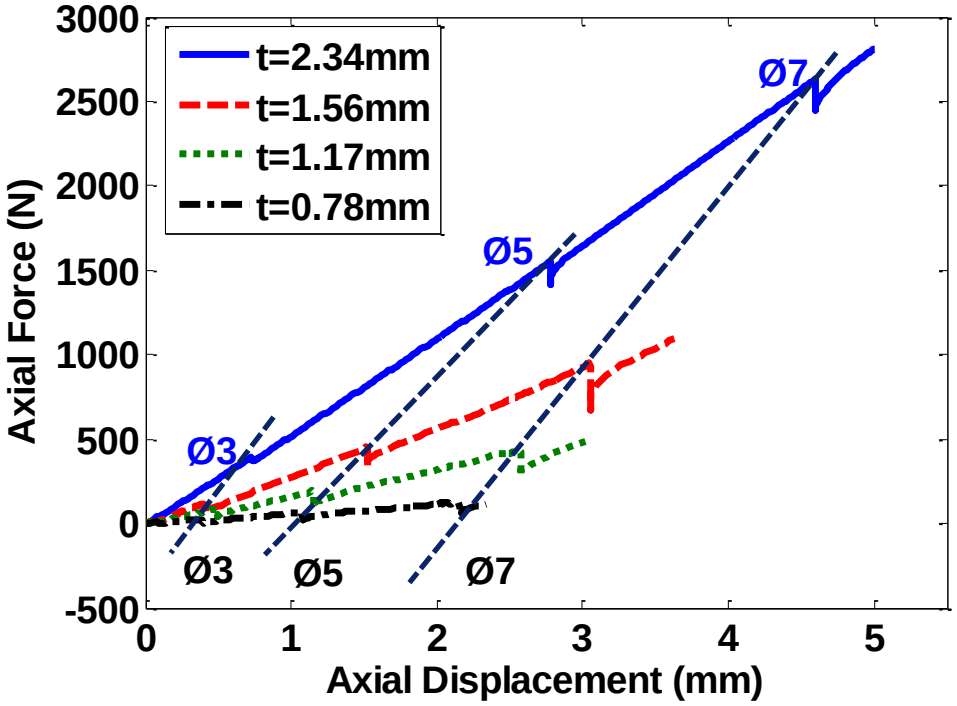


(c) Effect of beam's thickness.

Axial displacements and forces at which the transitions occur are determined by the aforementioned parameters. Their dependency to the system parameters was numerically investigated. Figure 3-11 displays the effect of Young's modulus, thickness and gap between the lateral constraints on the loading branch of the post-buckling response of the beam. This figure shows that by increasing the young's modulus the forces increase, but the axial displacements at transitions are invariant. In contrast, increasing the gap between the walls increases the axial displacements but the forces at transitions are the same. It also shows that the variation of the beam thickness affects both forces and displacements at mode transitions. However, the spacing between the events is proportional.

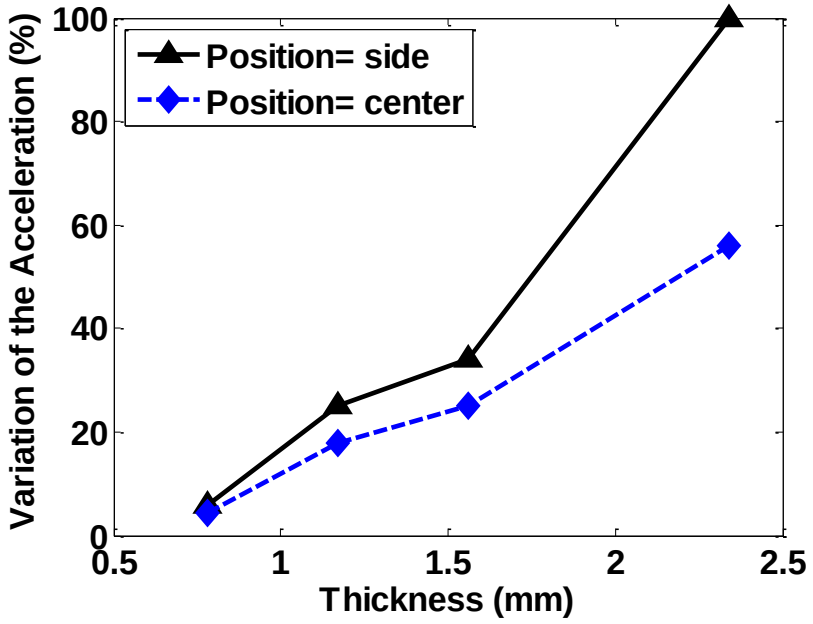


(a)

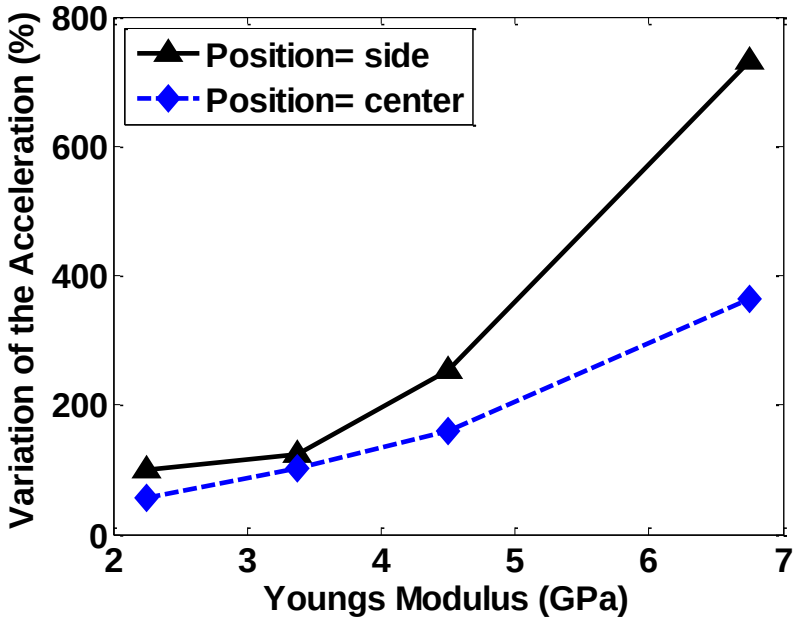


(b)

Figure 3-12: Results from the numerical parametric study showing the effect of (a) beam thickness, (b) elastic modulus, (c) wall gap, (d) beam length, and (e) boundary conditions on the maximum acceleration generated by snap-through behavior.

Figure 3-12 (cont'd)

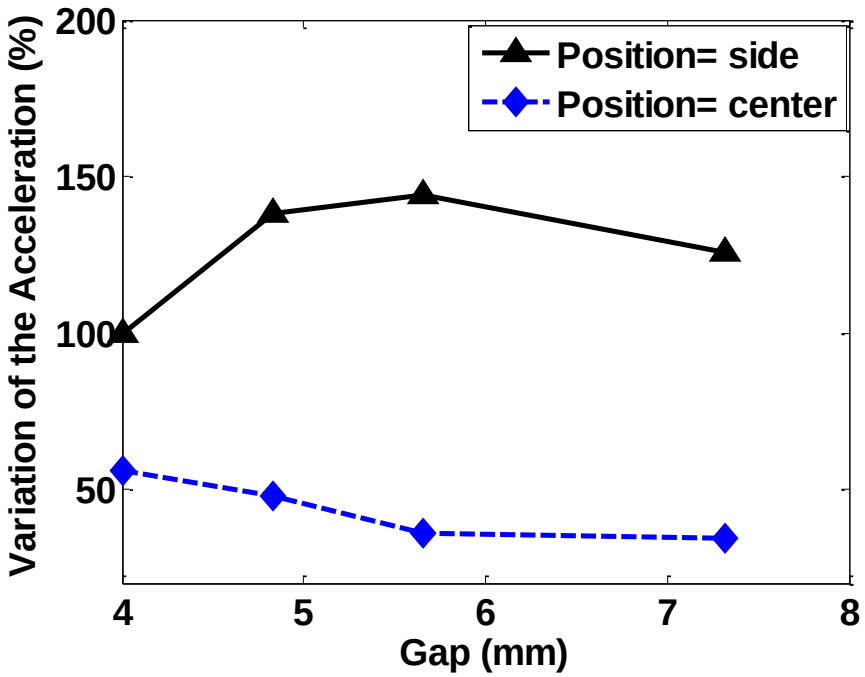


(c)

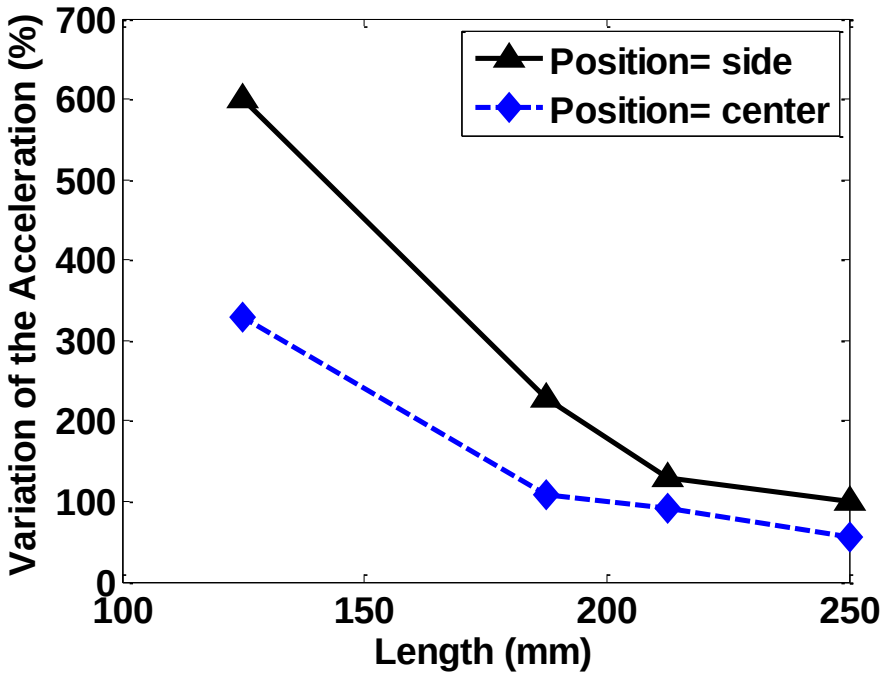


(d)

Figure 3-12 (cont'd)

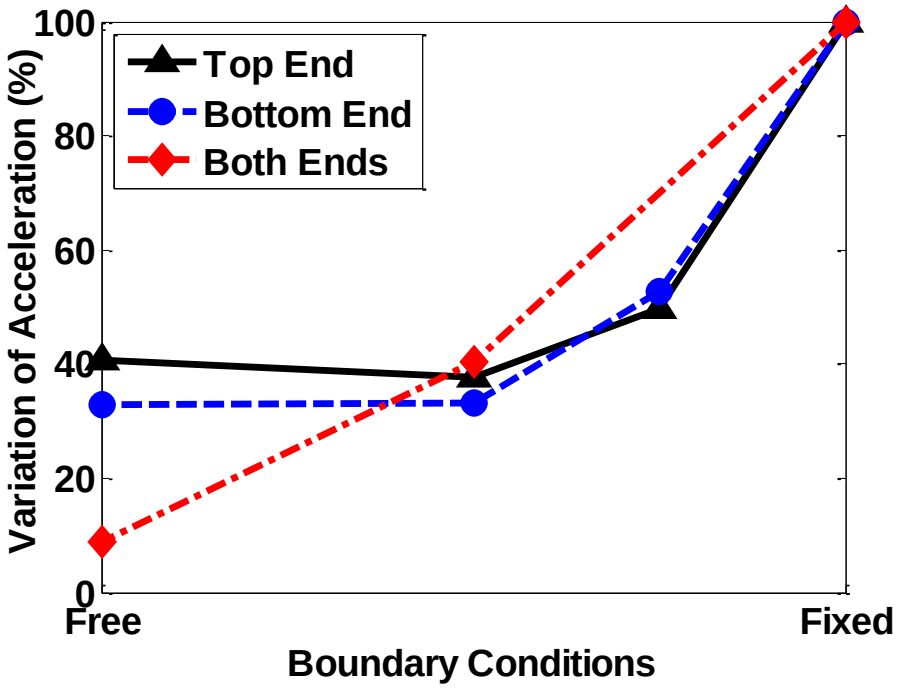


(e)

The maximum generated accelerations along the beam's height from the snap-through events for each of the first thirty five cases are compared in Figure 3-12 for each of the evaluated parameters. Each of the five plots corresponds to one of the parameters in the study and the result from Case 1 is presented in all plots. For all cases the data points correspond to the snap-through transition to the 7th buckling mode. Thus, the total vertical end shortening was varied to ensure that the 7th mode transition was achieved in all cases. Effect of the boundary conditions on the snap-through accelerations was investigated by gradually releasing the end rotations. Partial restraints were simulated by considering rotation springs at each end.

The results show that acceleration from snap-through will increase with: (a) an increase in beam thickness, (b) an increase in the beam elastic modulus, (c) an increase in the wall gap and (d) a decrease in the beam length. The noted trends are considered to be reasonable because the beam is stiffer if its thickness or Young's modulus increases or if its length is reduced. Also, an increase in the gap between the walls allows higher rotations of the beam in its buckled shape, which results in higher potential energy due to bending. Therefore the beam is able to store higher strain energy that is then released during the snap-through transitions. Results also show that the generated accelerations during transitions increase by placing the beam adjacent to one of the lateral walls (figures 3-12 (a) - (d)) and by adopting fixed-end configuration (Figure 3-12 (e)). Therefore for the remaining analyses the beam was placed adjacent to one of the lateral walls with fixed-end supports.

The results shown indicate the possibilities for optimizing the system performance and support the feasibility of down-scaling the system into sizes adequate for a device that can be embedded inside a structure as shown in figure 1-1 for the concept integration. For that purpose, a second set of simulations was carried out to investigate the combined effect of reducing the length and varying one of the other parameters.

Figure 3-13 displays the variation of the maximum acceleration with respect to the beam's length for different thickness values. The gap between the walls and the young's modulus remain constant. It should be noted that for case 16 (L = 76.2 mm and t = 2.34 mm) and case 45 (L = 76.2 mm and t = 1.56 mm) the beam fails to reach the seventh buckling mode. It was shown in Figure 3-12 (a) that, for the original length (L = 250 mm), the thicker is the beam, the higher are the snap-through accelerations. However, the results shown in Figure 3-13 indicate that for shorter beams

(L = 76.2 mm) the thickness should be reduced in order to reach the seventh mode and generate higher accelerations.

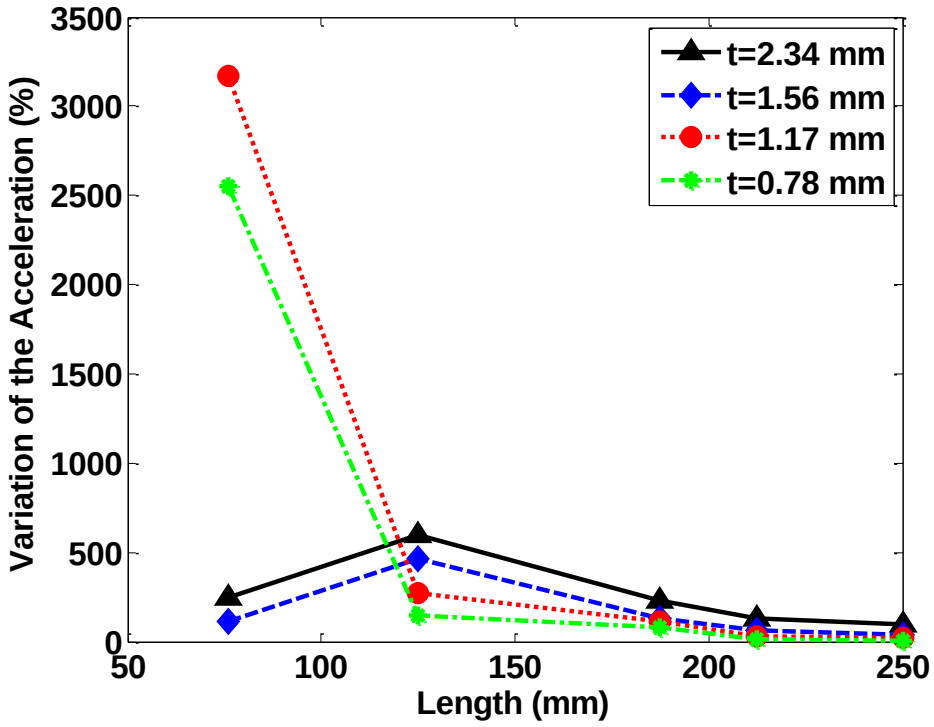


Figure 3-13: Effect of beam thickness and length on the maximum acceleration.

The combined effect of the gap between the walls and the length of the beam is presented in Figure 3-14. The cases 56 and 59 (G = 7.32 mm, L = 125 mm and L = 76.2 mm) fail to reach the seventh buckling mode. Therefore for reduced lengths the gap should be increased with an upper bound representing the limit after which the beam is locked in a lower buckling mode.

The net gap and the thickness are related. Therefore results shown in figures 3-13 and 3-14 are equivalent since a decrease in the thickness is equivalent to an increase in the gap. Hence, to design shorter beams, the ratio t/h is an important parameter to consider.

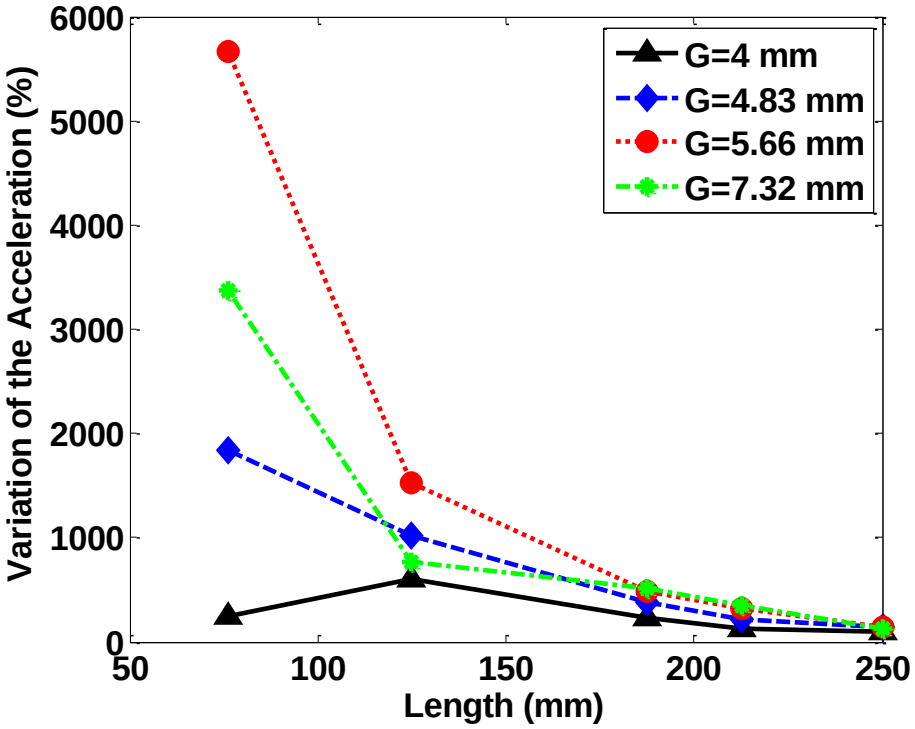


Figure 3-14: Effect of gap and length on the maximum acceleration.

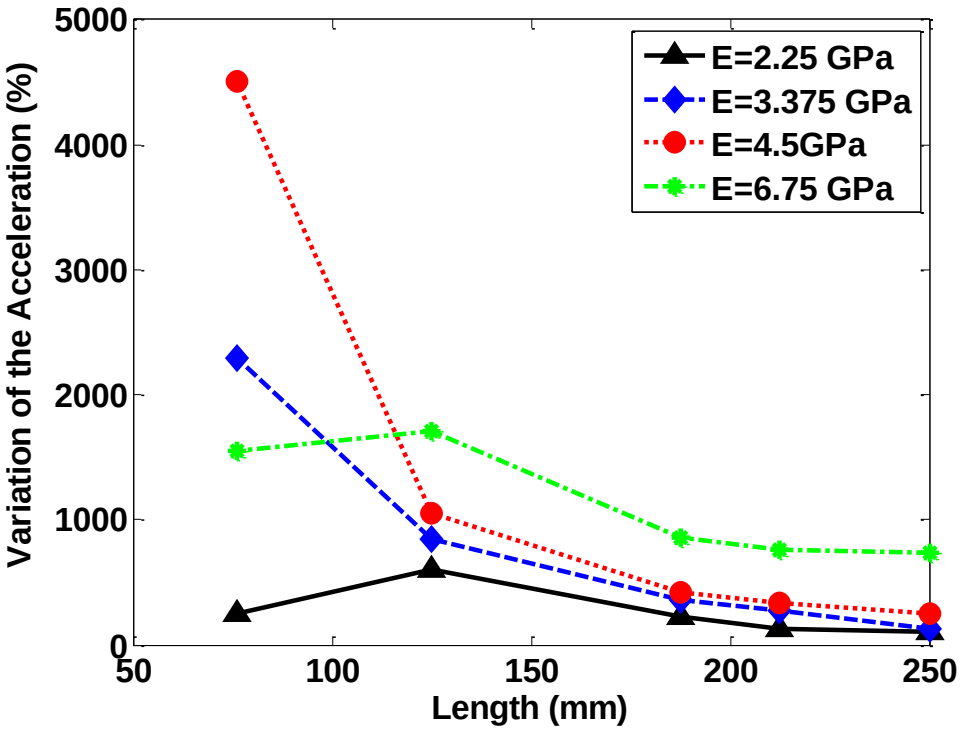


Figure 3-15: Effect of Young's modulus and length on the maximum acceleration.

Figure 3-15 displays the effect of the young's modulus and the length on the maximum acceleration generated during transitions. Similar to the gap, increasing the young's modulus amplify the levels of the accelerations. However, higher modes risk to be blocked for shorter beams (L = 76.2 mm, E = 6.75 GPa). Therefore the young's modulus should be bounded.

## 3.3. Post-buckling response of multiple bilaterally constrained beams in parallel configuration

Although tuning the parameters of the system affects dramatically the accelerations generated in snap-through transitions, the number and the spacing between these events was shown non-sensitive to the studied parameters. In order to tailor the number and spacing of the mode branch switching during the post-buckling response, the experimental setup described above for one bilaterally constrained beam was extended to accommodate for three parallel beams with fixed end supports. The constraining walls were kept separated by a 4 mm gap and three equi-length beams were placed inside the gap, adjacent to one of the constraining walls as shown in Figure 3-16.

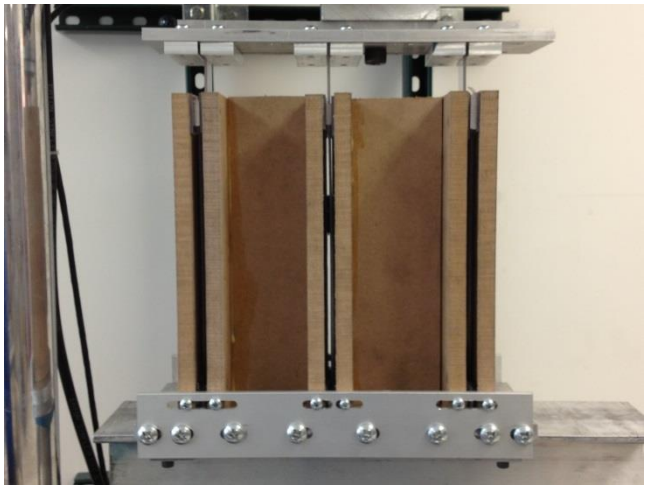

Figure 3-16: Test setup with three parallel constrained beams.

Two sets of experiments were conducted to demonstrate the system's ability to increase the number and force drop magnitude in the buckling mode transitions without exceeding the seventh mode in each beam. In the first experiment three similar beams with the same geometry and material properties as presented in Table 3-1 were used. The beams were axially loaded in compression under displacement control to a total end shortening of 5 mm and then unloaded. The top extremities of the beams exhibit the same loading displacement. In the second experiment one of the beams was substituted with a thinner polycarbonate beam (1.47 mm thickness) and the same experiment procedure was applied. Only one parameter changed between the two experiments, which is the thickness of one beam. The net gap between the walls was kept constant.

Figure 3-17 and Figure 3-18, successively, display the resulting force-displacement response of the system in the first and second experiment. Comparing the two plots it can be concluded that by changing one parameter, which in this case was the thickness of one beam, the number and force drop magnitude of the transitions change. Furthermore the location of the transitions and the overall stiffness of the system are affected by any modification in the major parameters. The finite element model described above was modified to investigate the effect of the beams thicknesses, young's modulus and the gap between the rigid walls on the number, positions and drop force magnitude of mode branch switchings during the post-buckling response, and to extract information on the transverse acceleration generated during mode jumping as well, which define the input to the piezoelectric energy harvester.

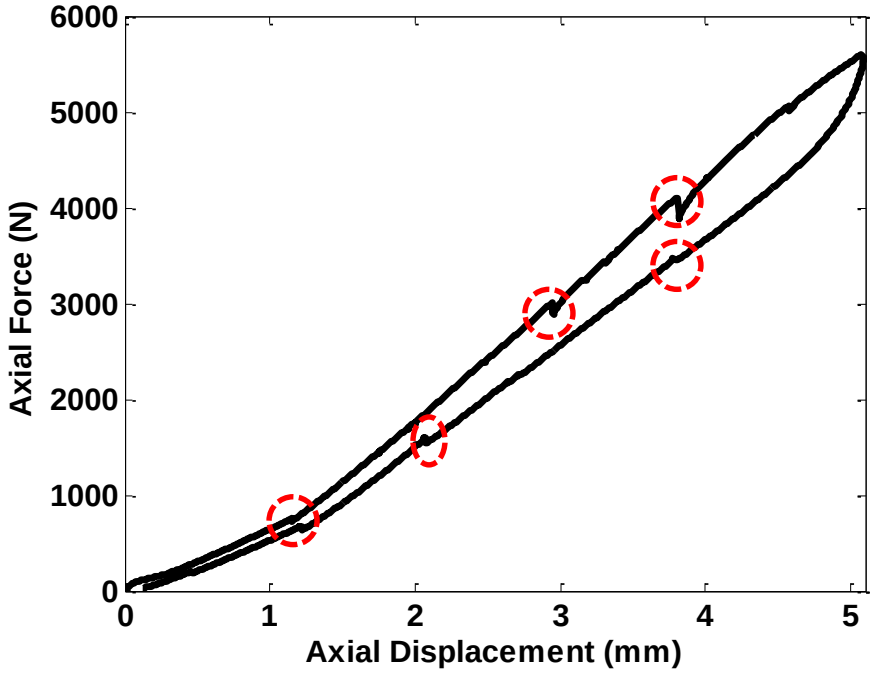


Figure 3-17: Force-displacement response of three similar parallel bilaterally constrained beams.

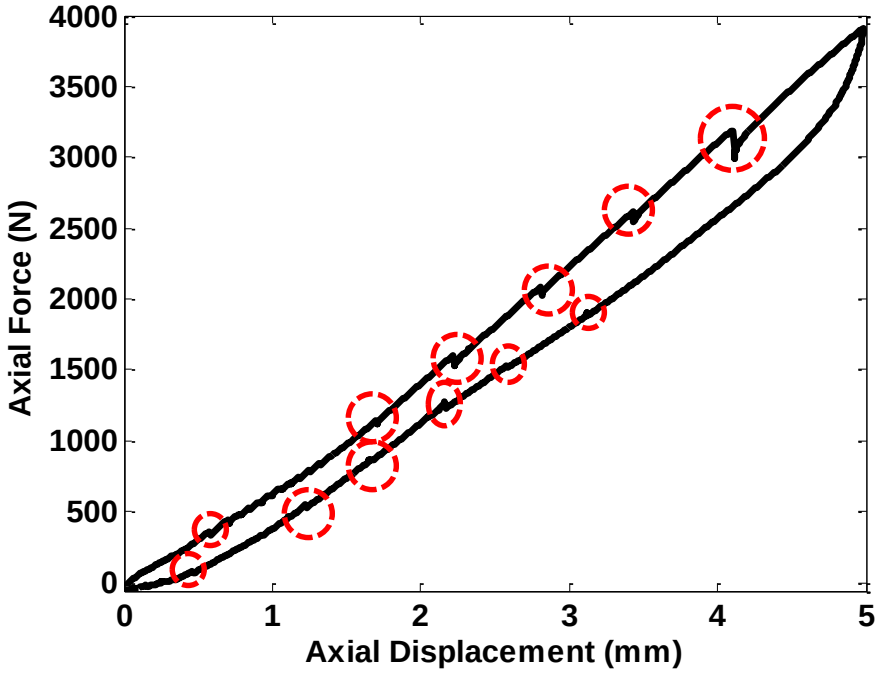


Figure 3-18: Force-displacement response of three parallel bilaterally constrained beams: two of them are similar and the third is thinner.

Table 3-3: Modified Parameter at each simulated case.

| Case | Young's modulus (MPa) | | | Beams thickness (mm) | | | Gap (mm) | | |
|---|---|---|---|---|---|---|---|---|---|
| | beam1 | beam2 | beam3 | beam1 | beam2 | beam3 | beam1 | beam2 | beam3 |
| 1 | 2250 | 2250 | 2250 | 2.34 | 2.34 | 2.34 | 4 | 4 | 4 |
| 2 | 2250 | 3375 | 4500 | 2.34 | 2.34 | 2.34 | 4 | 4 | 4 |
| 3 | 2250 | 2250 | 2250 | 2.34 | 1.47 | 0.78 | 4 | 4 | 4 |
| 4 | 2250 | 2250 | 2250 | 2.34 | 2.34 | 2.34 | 4 | 5 | 6 |

The overall force-displacement response of the three parallel constrained beam system is sensitive to the beams' geometry, material properties and gap between the constraining walls. To evaluate the impact of each parameter, four cases were numerically simulated. The first case consists of three beams with the same geometry and material properties as presented in Table 3-1 and the other cases change one of the pre-mentioned parameters at a time. Table 3-4 highlights the modified property of the beams at each case. In all cases the top edges of the beams were subjected to a total end shortening of 5 mm. The loading branches of the force displacement responses as well as transverse accelerations in the beams were extracted from the FE analyses database and are displayed in Figure 3-19 to Figure 3-22. Each acceleration spike is resulted from one or multiple beams movement or transitions between modes. The force drop magnitude and the acceleration levels can reflect the level of the released energy when the system transitions from one position to another. The number and spacing between the mode switching events can be tuned by modifying one or multiple parameters. Although the number and the locations of the transitions are very sensitive to the investigated parameters, the levels of the maximum acceleration are of the

same order. Hence the system transitions can be controlled such that the snap-through happens at certain predetermined axial forces or displacements without sacrificing acceleration levels.

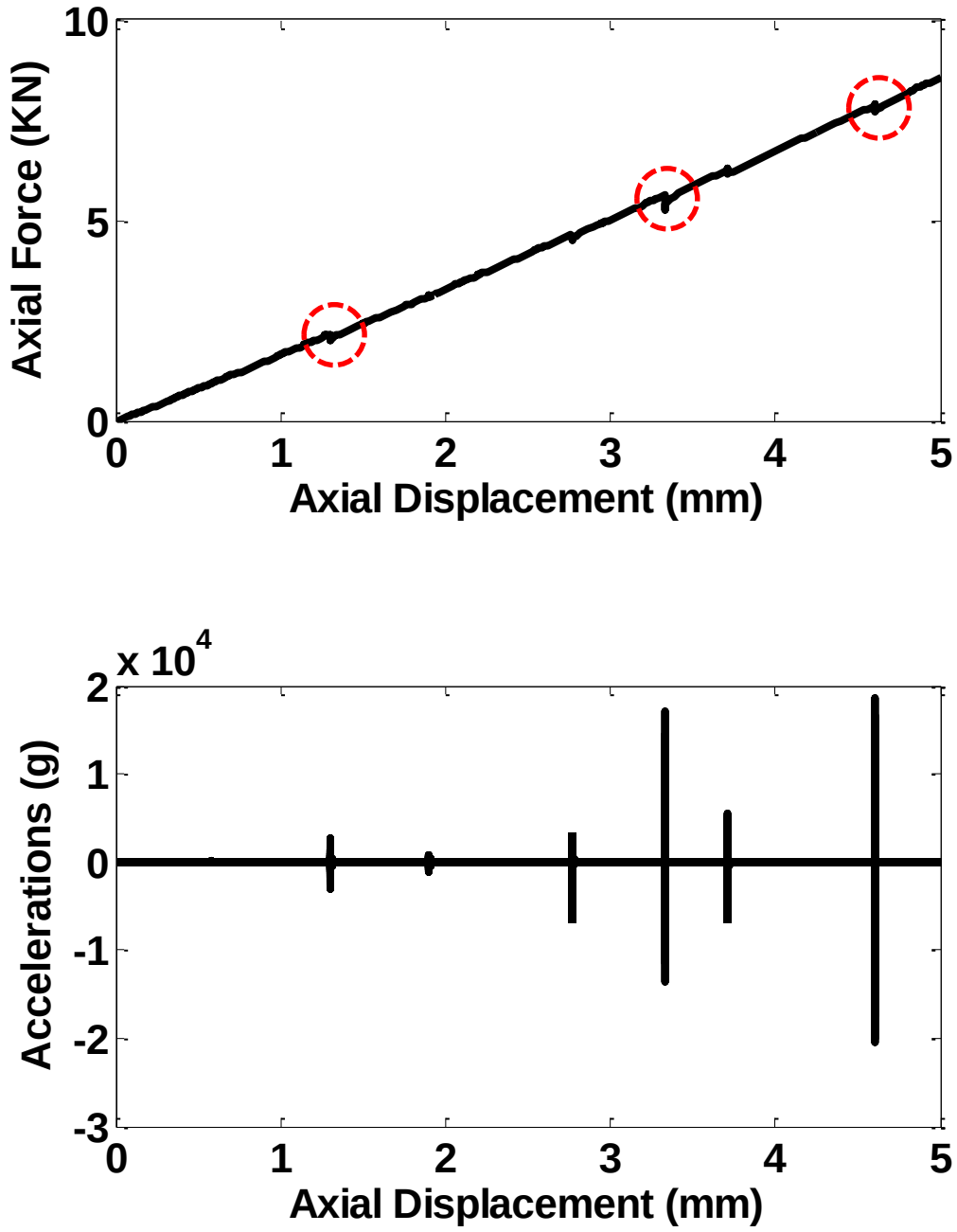


Figure 3-19: Loading branch of the force-displacement response and accelerations generated during transitions for Case 1 in Table 3-4 (same geometry and material properties for all beams).

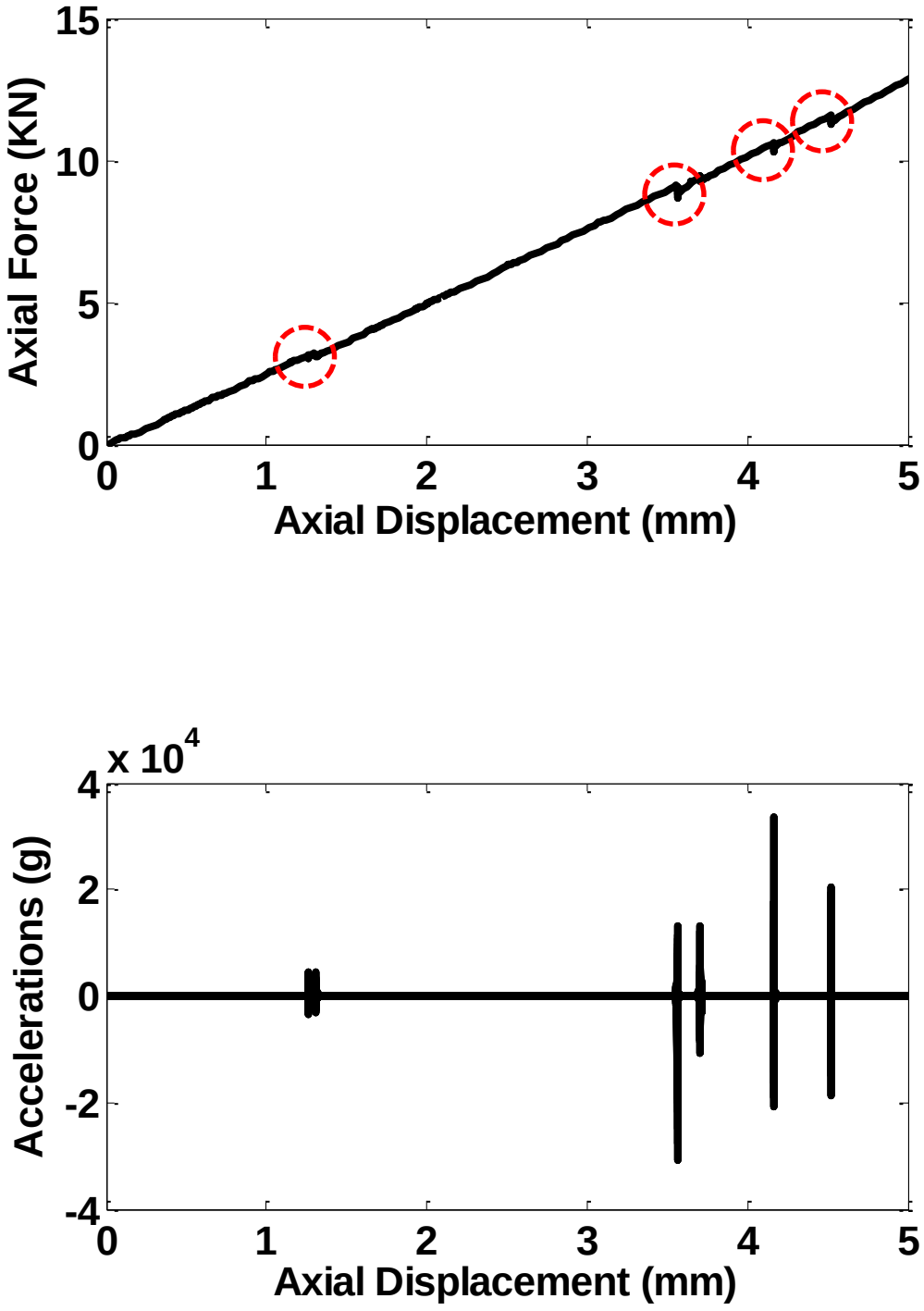


Figure 3-20: Loading branch of the force-displacement response and accelerations generated during transitions for Case 2 in Table 3-4 (variation of Young's moduli).

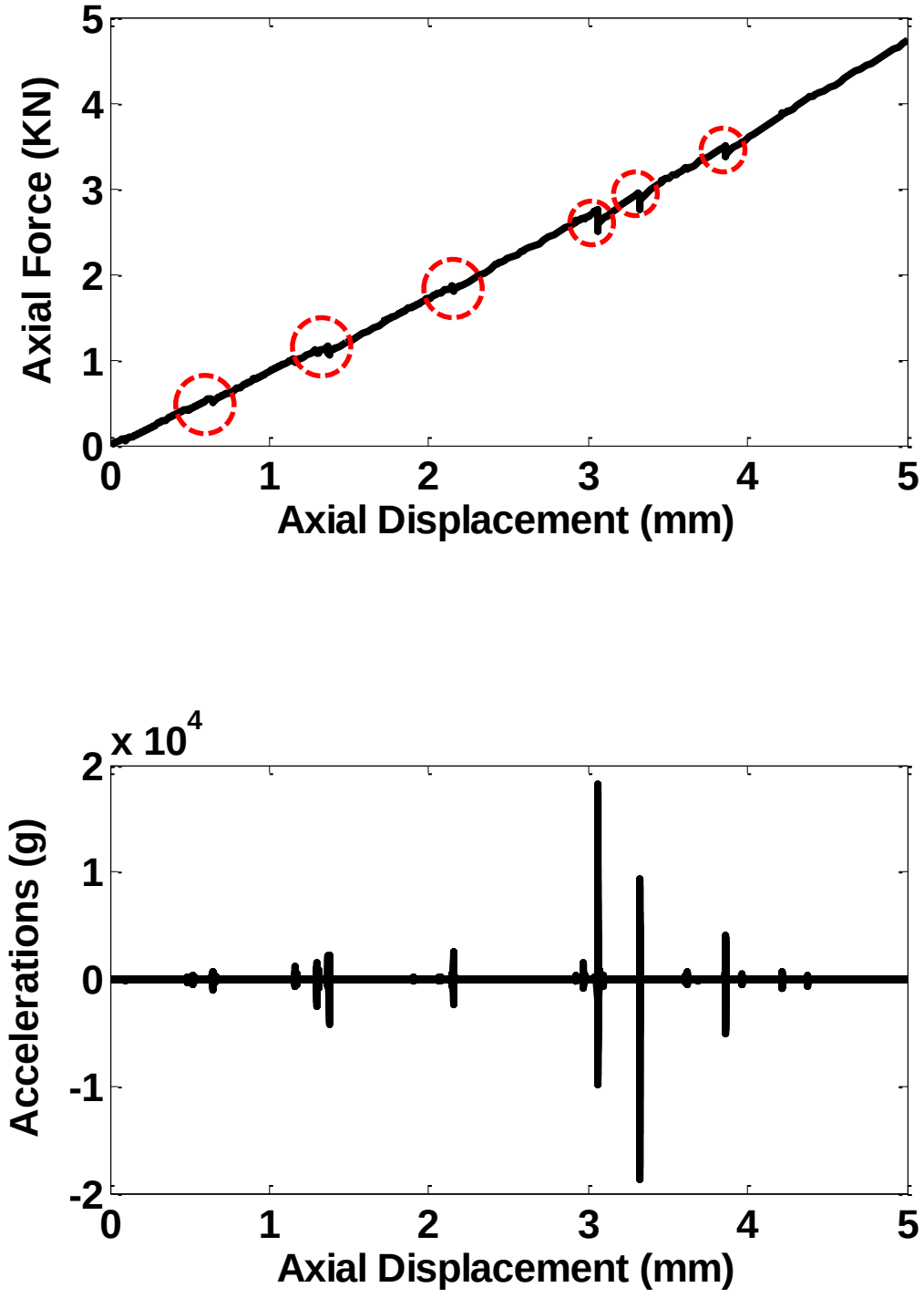


Figure 3-21: Loading branch of the force-displacement response and accelerations generated during transitions for Case 3 in Table 3-4 (variation of beams thicknesses).

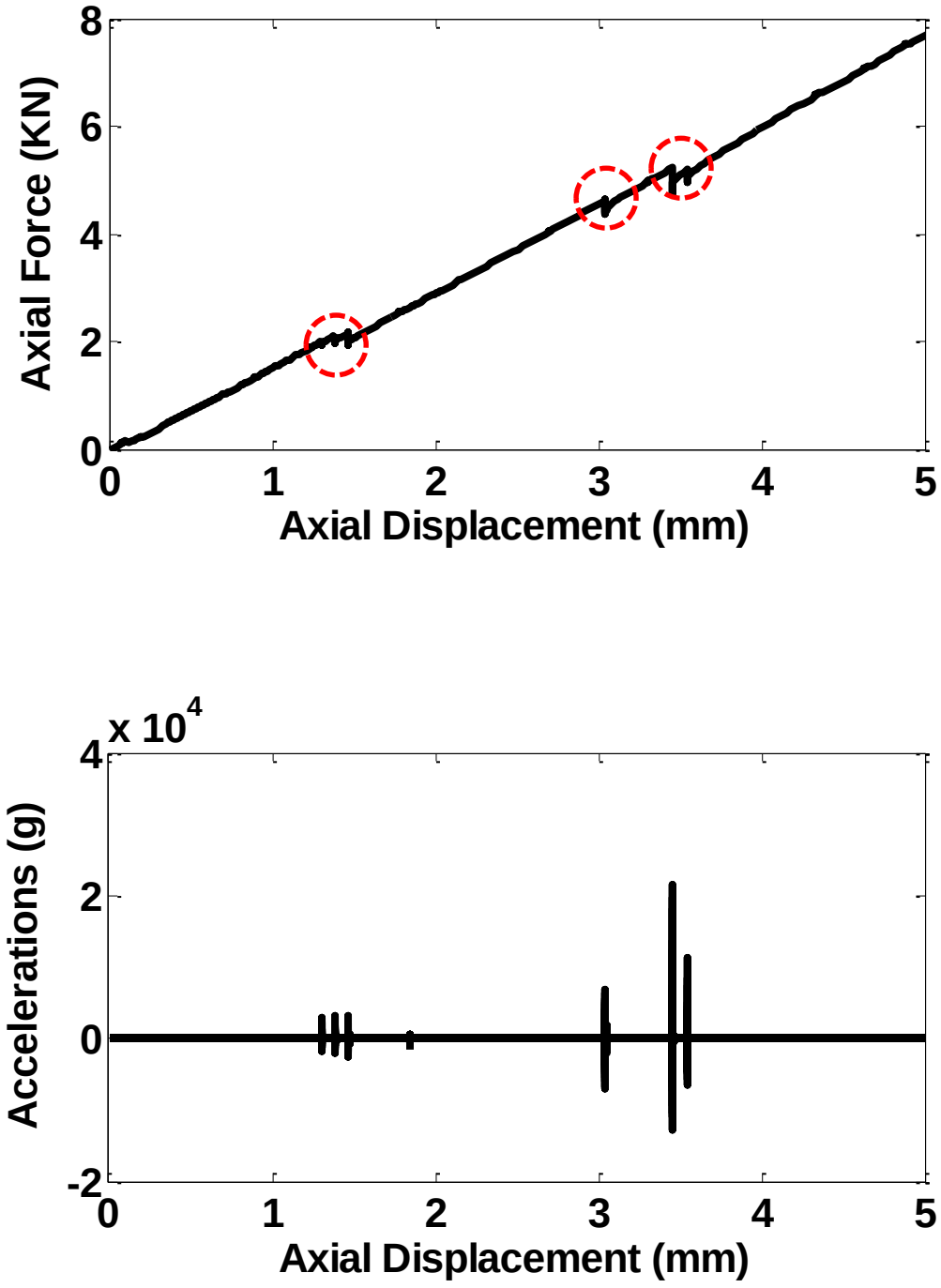


Figure 3-22: Loading branch of the force-displacement response and accelerations generated during transitions for Case 4 in Table 3-4 (variation of gaps between the lateral walls).

## 3.4. Summary

The post-buckling response of the axially loaded bilaterally constrained beams was investigated experimentally and numerically to provide better understanding of its behavior. It was shown that the beam can achieve higher buckling modes by providing the appropriate lateral constraints. Furthermore, the transitions between modes are sudden and generate high-rate transverse accelerations.

Experimental results show that the post-buckling behavior is reproducible under cyclic loadings and independent of the input loading frequency. An FE model that accounts for the friction between the beam and the lateral walls was developed to extract information on the transverse accelerations and to investigate the effect of system parameters on the accelerations as well as axial forces and displacements at mode transitions. It was shown that placing the beam adjacent to one of the lateral walls with fixed-end supports generates higher accelerations. Furthermore, the accelerations amplify by increasing the thickness, Young's modulus or gap between the walls, or by decreasing the length of the beam. However, the combination between length and one of the other parameters may have opposite effect. Results show that for short beams the thickness, young's modulus and gap should be upper-bounded in order to allow for the development of higher modes and hence the generation of high accelerations.

Although tuning the parameters of the system affects dramatically the accelerations generated in snap-through transitions, the number and the spacing between these events was shown to be insensitive to the studied parameters. In order to control the number and the spacing between mode transitions, multiple slender beams were stacked in parallel configurations. Experiments and numerical studies were conducted to investigate the global response of the system and the accelerations generated from each beam. It was shown that the global force-displacement response

is sensitive to the beams thicknesses, Young's moduli and gaps between the walls. Any modification of these parameters affects the locations of the transitions and the overall stiffness of the system. More important is that the number and the spacing between these events can be controlled by tuning the aforementioned parameters without sacrificing the levels of generated accelerations.

# CHAPTER 4: THEORETICAL STUDY OF THE POST-BUCKLING RESPONSE OF A BILATERALLY CONSTRAINED BEAM UNDER AXIAL LOADING [2]

## 4.1. Overview

This chapter presents a theoretical study of the post-buckling snap-through behavior of a bilaterally constrained beam subjected to axial loading using energy methods. In Section 4.2 the nonlinear relationship between strain and displacement is determined. Section 4.3 provides an eigenvalue buckling analysis that accounts for longitudinal deformations to determine the buckling modes. Using the Galerkin discretization method, the transverse deflection is expressed as a linear combination of buckling modes multiplied by weight coefficients that define the contribution of each mode to the deflection. The normalized kinetic, potential and friction-induced energies are expressed in terms of the unknown weight coefficients in Section 4.4. Section 4.5 presents a frictionless static analysis of the beam's response based on minimization of the potential energy under the confinement constraints. The potential energy is composed of bending and compression energies and the work of the external load. Both displacement- and force- control formulations are presented. The dynamic snap-through transitions under axial force loading are investigated in Section 4.6. The released kinetic energy as well as accelerations of the beam during buckling mode switching are determined by minimizing the total energy which is the sum of kinetic and potential energies.

[2] Results presented in this chapter were published in Borchani et al. (2014a and 2014b).

## 4.2. Strain-displacement Relationship

The problem under consideration consists of a straight beam subjected to increasing axial load, $\hat{p}$. The loaded end is allowed to slide axially and the other end is fixed as shown in Figure 4-1. The beam has a length L, a uniform cross section area A, a moment of inertia I and a modulus of elasticity E. The beam is confined between two rigid surfaces spaced by a distance h. $\hat{u}(x)$ and $\hat{w}(x)$ denote the axial displacement and transverse deflection, respectively.

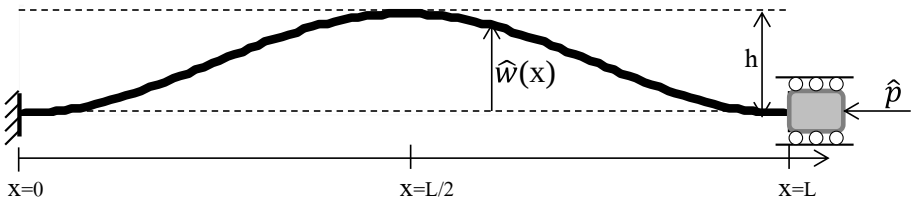


Figure 4-1: Geometry of the beam buckled in the first mode.

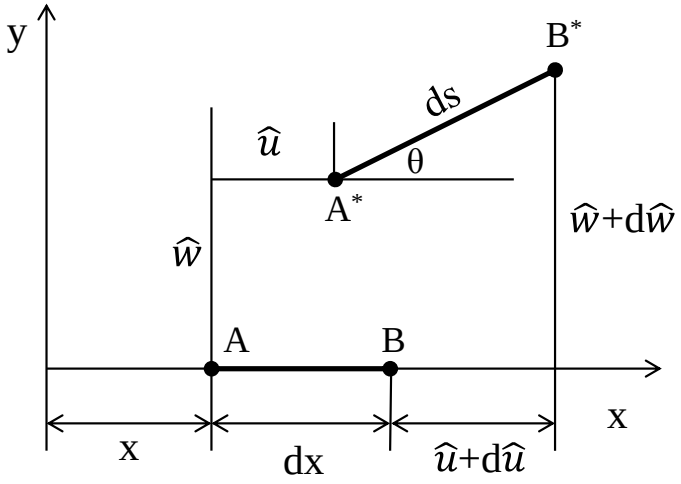


Figure 4-2: Deformation of beam element.

The nonlinear strain-displacement relationship is obtained by considering a differential element AB located at a distance x from the origin as shown in Figure 4-2. The element length in

the undeformed beam is dx. The beam under study is slender and therefore it can be modeled using nonlinear Euler-Bernoulli beam theory.

The length of the element in the deformed configuration can be related to the longitudinal and transversal displacements by:

$$ds = \sqrt{(dx + d\hat{u})^2 + d\hat{w}^2}. \tag{4-1}$$

The total elongation of the differential element is given by:

$$e = ds - dx$$

$$= \sqrt{(dx + d\hat{u})^2 + d\hat{w}^2} - dx. \tag{4-2}$$

The resulting strain $e/dx$ is then expressed as:

$$\varepsilon = \sqrt{(1 + \hat{u}')^2 + \hat{w}'^2} - 1$$

$$= \sqrt{1 + 2\hat{u}' + \hat{u}'^2 + \hat{w}'^2} - 1 \tag{4-3}$$

where the over primes denote the derivative with respect to $x$. Using a binomial series expansion for the quadratic terms and neglecting higher order terms in the displacement gradient, the resulting strain can be expressed as:

$$\varepsilon = \hat{u}' + \frac{\hat{w}'^2}{2}. \tag{4-4}$$

By integrating the strain over the beam's span, the variation in length due to the buckled configuration can be expressed as:

$$\Delta = \Delta_c + \int_0^L \frac{\widehat{w}'^2}{2}\, dx. \tag{4-5}$$

The first term, $\Delta_c = \hat{u}(L) - \hat{u}(0)$, is due to axial compression and the second term, $\int_0^L \widehat{w}'^2/2\, dx$, is induced by the midplane rotation due to buckling. The midplane stretching induces an axial compressive force that can be expressed by:

$$S = \frac{EA}{L}\Delta_c$$

$$= EA\left(\varepsilon - \frac{1}{2L}\int_0^L \widehat{w}'^2\, dx\right). \tag{4-6}$$

## 4.3. Buckling analysis

The governing equations that account for longitudinal deformations in a fixed-fixed straight beam subjected to axial load $\hat{p}$ are:

$$EI\frac{d^4\widehat{w}(x)}{dx^4} + \left(\hat{p} - \frac{EA}{2L}\int_0^L \widehat{w}'^2\, dx\right)\frac{d^2\widehat{w}(x)}{dx^2} = 0$$

$$\widehat{w}(0) = \widehat{w}(L) = 0, \qquad \left.\frac{d\widehat{w}(x)}{dx}\right|_{x=0} = \left.\frac{d\widehat{w}(x)}{dx}\right|_{x=L} = 0. \tag{4-7}$$

For convenience, the following non-dimensional variables are used:

$$X = \frac{x}{L}, \qquad W(X) = \frac{\widehat{w}(X\,L)}{h}, \qquad N^2 = \frac{\hat{p}L^2}{EI} - \frac{Ah^2}{2I}\int_0^1 \left(\frac{dW}{dX}\right)^2 dX. \tag{4-8}$$

Substituting Equation (4-8) into (4-7), the non-dimensional buckling equation is then expressed as:

$$\frac{d^4W(X)}{dX^4} + N^2\frac{d^2W(X)}{dX^2} = 0$$

$$W(0) = W(1) = 0, \qquad \left.\frac{dW(X)}{dX}\right|_{X=0} = \left.\frac{dW(X)}{dX}\right|_{X=1} = 0. \tag{4-9}$$

The general solution of Equation (4-9) is given by Equation (2-4). The buckling analysis was presented in details in Section 2.3. The symmetric and antisymmetric mode shapes are expressed, respectively, by:

$$\left.\begin{aligned} W_j(X) &= 1 - cos\left(N_jX\right) \\ N_j &= (j+1)\pi \end{aligned}\right\} \; j = 1, 3, 5, \ldots \tag{4-10}$$

$$\left.\begin{aligned} W_j(X) &= 1 - 2X - cos\left(N_jX\right) + \frac{2sin\left(N_jX\right)}{N_j} \\ N_j &= 2.86\pi, 4.92\pi, 6.94\pi, 8.95\pi, , \ldots \end{aligned}\right\} j = 2, 4, 6, \ldots \; . \tag{4-11}$$

The Buckling modes given in Equations (4-10) and (4-11) form an orthogonal basis. Hence mode superposition method can be used to express the beam deflection as a linear combination of buckling modes, written as:

$$W(X) = \sum_{j=1}^{\infty} A_j\, W_j(X), \tag{4-12}$$

where $A_j$ are weight coefficients that determine the contribution of each mode to the transverse deflection.

## 4.4. Derivation of kinetic, potential and dissipation energies

Every stable equilibrium configuration corresponds to an energy minimum. If the loading is static with no dissipation of energy, the equilibrium corresponds to a potential energy well. As the axial force increases the equilibrium at a certain configuration becomes unstable, thus the beam snaps into a different stable configuration with lower energy. The total energy is the sum of the potential energy, kinetic energy and dissipated energy. Since the axial loading is quasi-static, kinetic energy in the axial direction can be neglected. Therefore the kinetic energy, $\widehat{K}$, can be expressed by:

$$\widehat{K}(\hat{t}) = \frac{1}{2}\int_0^L m(x)\left(\frac{\partial \widehat{\omega}(x,\hat{t})}{\partial \hat{t}}\right)^2 dx, \tag{4-13}$$

where $m(x)$ is a constant representing the mass per unit length of the undeformed beam and $\hat{t}$ is the time variable. The total potential energy is the sum of the bending and axial compression strain energies stored in the deformed elastic element and the potential energy due to external force.

In general, if a force is applied to a prismatic beam in a gradual manner, i.e. the magnitude of the force increases from 0 to $p$, and the bar stretches by $\Delta$, when the material behaves in a linear-elastic manner $F = px/\Delta$ then the work of the external force is given by:

$$u_e = \int_0^{\Delta} \frac{p}{\Delta} x\, dx = \frac{1}{2} p\, \Delta. \tag{4-14}$$

Since the force is gradually increasing, the potential energies $u_b$ ,$u_c$ and $u_p$ due to bending, compression and external applied force, respectively, are given by:

$$u_b = \frac{1}{2} EI \int_0^L \left( \frac{d^2 \widehat{w}(x)}{dx^2} \right)^2 dx \tag{4-15}$$

$$u_c = \frac{1}{2} S \Delta_c \tag{4-16}$$

$$u_p = -\frac{1}{2} \hat{p} \Delta. \tag{4-17}$$

The following non-dimensional variables are introduced:

$$d = \frac{\Delta L}{h^2}, \qquad U(X) = \frac{\hat{u}(XL)L}{h^2}, \qquad Q = \frac{t}{h}, \qquad \delta = \frac{\Delta_c L}{h^2}, \qquad P = \frac{\hat{p} L^2}{EI}$$

$$V_b = \frac{u_b L^3}{EIh^2}, \qquad V_c = \frac{u_c L^3}{EIh^2}, \qquad V_P = \frac{u_p L^3}{EIh^2}, \qquad K = \frac{\widehat{K} L^3}{EIh^2}, \qquad t = \hat{t} \sqrt{\frac{EI}{mL^4}} \tag{4-18}$$

The normalized transverse displacement is expressed in Equation (4-12) as a linear combination of all the buckling modes expressed in Equations (4-10) and (4-11). Substituting their expressions and differentiating the normalized transverse displacement up to four times gives

$$W(X) = \sum_{j=1,3,5,\ldots}^{\infty} A_j \left(1 - cos\left(N_j X\right)\right) + \sum_{j=2,4,6,\ldots}^{\infty} A_j \left(1 - 2X - cos\left(N_j X\right) + \frac{2\, sin\left(N_j X\right)}{N_j}\right) \tag{4-19 a}$$

$$W'(X) = \sum_{j=1,3,5,\ldots}^{\infty} A_j \; N_j sin\left(N_j X\right) + \sum_{j=2,4,6,\ldots}^{\infty} A_j \left(-2 + N_j \, sin\left(N_j X\right) \; + 2\, cos\left(N_j X\right)\right) \tag{4-19 b}$$

$$W''(X) = \sum_{j=1,3,5,\ldots}^{\infty} A_j \; N_j^2 \; cos\left(N_j X\right) + \sum_{j=2,4,6,\ldots}^{\infty} A_j \left(N_j^2 \; cos\left(N_j X\right) - 2 N_j \, sin\left(N_j X\right)\right) \tag{4-19 c}$$

$$W'''(X) = -\sum_{j=1,3,5,\ldots}^{\infty} A_j \; N_j^3 \; sin(N_j X)$$

$$-\sum_{j=2,4,6,\ldots}^{\infty} A_j \left(N_j^3 \; sin(N_j X) \; + 2N_j^2 \; cos(N_j X)\right) \quad \text{(4-19 d)}$$

$$W^{(4)}(X) = -\sum_{j=1,3,5,\ldots}^{\infty} A_j \; N_j^4 \; cos(N_j X)$$

$$-\sum_{j=2,4,6,\ldots}^{\infty} A_j \left(N_j^4 \; cos(N_j X) - 2N_j^3 \; sin(N_j X)\right) \quad \text{(4-19 e)}$$

### *4.4.1. Normalized kinetic energy*

Substituting the non-dimensional variables expressed in Equation (4-18) into the expression of the kinetic energy (Equation (4-13)), the normalized kinetic energy can be expressed by

$$K = \frac{1}{2}\int_0^1 \left(\frac{\partial W(X,t)}{\partial t}\right)^2 dX \quad \text{(4-20)}$$

Time and space coordinates can be separated using Galerkin discretization method. The transverse displacement can be expressed as a linear combination of admissible functions multiplied by unknown temporal coordinate:

$$W(X,t) = \sum_{i=1}^{\infty} A_i(t) W_i(X) \quad \text{(4-21)}$$

where $A_i(t)$ are the generalized temporal coordinate and $W_i(X)$ are the buckling mode shapes which constitute a set of orthonormal admissible functions. Substituting the buckling mode shape expressions in Equations (4-10) and (4-11) into Equation (4-20), the normalized kinetic energy is then expressed by:

$$K = \frac{1}{2}\int_0^1 \left(\sum_{i=1}^{\infty} \frac{\partial A_i(t)}{\partial t} W_i(X)\right)^2 dX$$

$$= \frac{1}{2}\left( \sum_{i=1,3,5,\ldots}^{\infty} \frac{3}{2}\left(\frac{\partial A_i(t)}{\partial t}\right)^2 + 2 \sum_{i=1,3,5,\ldots}^{\infty} \sum_{j=3,5,\ldots>i}^{\infty} \frac{\partial A_i(t)}{\partial t}\frac{\partial A_j(t)}{\partial t} \right.$$

$$+ \sum_{i=2,4,6,\ldots}^{\infty} \left(\frac{\partial A_i(t)}{\partial t}\right)^2 \frac{1}{12\,\mathrm{N_i^3}} \left(2\,\mathrm{N_i}\left(6 + 5\,\mathrm{N_i^2}\right) + 96\,\mathrm{N_i}\cos(\mathrm{N_i}) + 12\,\mathrm{N_i}\cos(2\,\mathrm{N_i})\right.$$

$$\left. + 24\left(-4 + \mathrm{N_i^2}\right)\sin(\mathrm{N_i}) + 3\left(-4 + \mathrm{N_i^2}\right)\sin(2\,\mathrm{N_i})\right)$$

$$+ 2 \sum_{i=2,4,6,\ldots}^{\infty} \sum_{j=4,6,\ldots>i}^{\infty} \frac{\partial A_i(t)}{\partial t}\frac{\partial A_j(t)}{\partial t} \frac{1}{3\,\mathrm{N_i^3}\left(\mathrm{N_i} - \mathrm{N_j}\right)\mathrm{N_j^3}\left(\mathrm{N_i} + \mathrm{N_j}\right)} \left(3\,\mathrm{N_i^2 N_j}\cos\left(\mathrm{N_j}\right)\left(4\,\mathrm{N_i}\left(\mathrm{N_i^2}\right.\right.\right.$$

$$\left. - \mathrm{N_j^2}\right) + \left(4 + \mathrm{N_i^2}\right)\mathrm{N_j^2}\sin(\mathrm{N_i})\Big) - 3\mathrm{N_i N_j^2}\cos(\mathrm{N_i})\left(-4\,\mathrm{N_i^2 N_j} + 4\,\mathrm{N_j^3} + \mathrm{N_i^2}\left(4 + \mathrm{N_j^2}\right)\sin\left(\mathrm{N_j}\right)\right)$$

$$+ \left(\mathrm{N_i^2} - \mathrm{N_j^2}\right)\left(3\,\mathrm{N_j^2}\sin(\mathrm{Ni})\left(\left(-4 + \mathrm{N_i^2}\right)\mathrm{N_j} - 2\mathrm{N_i^2}\sin\left(\mathrm{N_j}\right)\right)\right.$$

$$\left.\left. + \mathrm{N_i^3}\left(\mathrm{N_j^3} + 3\left(-4 + \mathrm{N_j^2}\right)\sin(\mathrm{Nj})\right)\right)\right)$$

$$+ 2 \sum_{i=1,3,5,\ldots}^{\infty} \sum_{j=2,4,6,\ldots}^{\infty} \frac{\partial A_i(t)}{\partial t}\frac{\partial A_j(t)}{\partial t} \frac{1}{\mathrm{N_i^2}\left(\mathrm{N_i} - \mathrm{N_j}\right)\mathrm{N_j^2}\left(\mathrm{N_i} + \mathrm{N_j}\right)} \left(2\,\mathrm{N_i^4} - 2\,\mathrm{N_i^2 N_j^2} + 2\,\mathrm{N_j^4}\right.$$

$$+ \mathrm{N_i^3 N_j^2}\sin(\mathrm{N_i}) - \mathrm{N_i N_j^4}\sin(\mathrm{Ni}) + \mathrm{N_i^2}\cos\left(\mathrm{N_j}\right)\left(-2\,\mathrm{N_i^2} + 2\,\mathrm{N_j^2} + \mathrm{N_i N_j^2}\sin(\mathrm{N_i})\right)$$

$$- \mathrm{N_i^4\,N_j}\sin\left(\mathrm{N_j}\right) + \mathrm{N_i^2 N_j^3}\sin\left(\mathrm{N_j}\right) - 2\,\mathrm{N_i^3 N_j}\sin(\mathrm{N_i})\sin\left(\mathrm{N_j}\right)$$

$$\left.\left. - \mathrm{N_j^2}\cos(\mathrm{N_i})\left(-2\,\mathrm{N_i^2} + 2\,\mathrm{N_j^2} + 2\mathrm{N_i^2}\cos\left(\mathrm{N_j}\right) + \mathrm{N_i^2 N_j}\sin\left(\mathrm{N_j}\right)\right)\right)\right). \qquad (4\text{-}22)$$

*4.4.2. Normalized potential energy*

The normalized midplane stretching and potential energies are expressed by substituting Equations (4-8) and (4-18) into Equations (4-5) and (4-15)-(4-17) as:

$$d = \frac{L}{h^2}\left[\Delta_c + \int_0^L \frac{w'^2}{2}\, dx\right]$$

$$= \delta + \frac{1}{2}\int_0^1 \left(\frac{dW}{dX}\right)^2 dX, \tag{4-23}$$

$$V_b = \frac{1}{2}\int_0^1 \left(\frac{d^2W(X)}{dX^2}\right)^2 dX, \tag{4-24}$$

$$V_P = -\frac{1}{2}\frac{L^3}{EIh^2}\,\frac{EIP}{L^2}\,\frac{h^2 d}{L}$$

$$= -\frac{Pd}{2}, \tag{4-25}$$

$$V_c = \frac{1}{2}\left(\frac{L^3}{EIh^2}\right)\left(\frac{EA}{L}\frac{h^2\delta}{L}\right)\frac{h^2\delta}{L}$$

$$= \frac{6}{Q^2}\delta^2. \tag{4-26}$$

Substituting Equation (4-19) into Equations (4-23) and (4-24), the normalized end shortening and bending strain energy are expressed, respectively, as

$$d = \delta + \frac{1}{2}\int_0^1 \left(\frac{dW}{dX}\right)^2 dX$$

$$= \frac{PQ^2}{12} + \frac{1}{2}\int_0^1 \left(\sum_{j=1,3,5,\ldots}^{\infty} A_j\, N_j sin\left(N_j X\right)\right.$$

$$\left. + \sum_{j=2,4,6,\ldots}^{\infty} A_j\left(-2 + N_j\, sin\left(N_j X\right) + 2\, cos\left(N_j X\right)\right)\right)^2 dX$$

$$= \frac{PQ^2}{12} + \frac{1}{2}\Bigg[\sum_{j=1,3,5,\ldots}^{\infty} \frac{N_j^2}{2} A_j^2 + \sum_{j=2,4,6,\ldots}^{\infty} \frac{A_j^2}{2N_j}\Big(6N_j + N_j^3 - 2N_j\cos\left(2N_j\right) - 16\sin\left(N_j\right)$$

$$+ \cos\left(N_j\right)\sin\left(N_j\right)\left(8N_j - \left(N_j^2 - 4\right)\right)\Big) + 2\sum_{i=2,4,6,\ldots}^{\infty}\sum_{j=4,6,8,\ldots>i}^{\infty}\Bigg(-2$$

$$-\frac{1}{4N_iN_j\left(N_i - N_j\right)\left(N_i + N_j\right)\left(-2 + N_i\cot\left(\frac{N_i}{2}\right)\right)\left(-2 + N_j\cot\left(\frac{N_j}{2}\right)\right)}$$

$$\times\Bigg(\csc\left(\frac{N_i}{2}\right)^2\csc\left(\frac{N_j}{2}\right)^2\left(-2 + 2\cos(N_i) + N_i\sin(N_i)\right)$$

$$\times\left(-2 + 2\cos\left(N_j\right) + N_j\sin\left(N_j\right)\right)\left(-N_iN_j\cos\left(N_j\right)\left(2\left(N_i^2 - N_j^2\right)\right.\right.$$

$$\left.+ N_i\left(4 + N_j^2\right)\sin(N_i)\right) + N_iN_j\cos(N_i)\Big(-2N_i^2 + 2N_j^2 + 2\left(N_i^2 - N_j^2\right)\cos\left(N_j\right)$$

$$\left.\left.+ (4 + N_i^2)N_j\sin\left(N_j\right) + 4\left(N_i^2 - N_j^2\right)\Big(N_j\sin(N_i) + N_i\left(-N_j + \sin\left(N_j\right)\right)\Big)\Big)\Big)\Bigg)\Bigg)A_iA_j$$

$$+ 2\sum_{i=1,3,5,\ldots}^{\infty}\sum_{j=2,4,6,\ldots}^{\infty}\frac{2N_i^2 - 2N_i^2\cos\left(N_j\right) - N_i^2N_j\sin\left(N_j\right)}{N_i^2 - N_j^2}A_iA_j\Bigg], \qquad (4\text{-}27)$$

$$V_b = \frac{1}{2}\int_0^1 \left( \sum_{j=1,3,\dots}^{\infty} A_j\ N_j^2\ cos(N_j X) + \sum_{j=2,4,\dots}^{\infty} A_j \left(N_j^2\ cos(N_j X) - 2N_j\ sin(N_j X)\right) \right)^2 dX$$

$$= \frac{1}{2}\Bigg[ \sum_{j=1,3,5,\dots}^{\infty} \frac{N_j^4}{2} A_j^2 + \sum_{i=2,4,6,\dots}^{\infty} \frac{N_j}{4}(2N_i(2+N_i^2) + 4N_i\ cos(2N_i) + (-4+N_i^2)\ sin(2N_i))A_i^2$$

$$+ 2\sum_{i=1,3,5,\dots}^{\infty}\ \sum_{j=2,4,6,\dots}^{\infty} \frac{N_i^2 N_j \left(2N_j - N_j\left(2\ cos(N_j) + N_j\ sin(N_j)\right)\right)}{N_i^2 - N_j^2} A_i A_j$$

$$+ 2\sum_{i=2,4,6,\dots}^{\infty}\ \sum_{j=4,6,8,\dots>i}^{\infty} \frac{N_i N_j}{N_i^2 - N_j^2}\left(N_j(4+N_i^2)\ cos(N_j)\ sin(N_i)\right.$$

$$\left. - N_i\left(4+N_j^2\right) cos(N_i)\ sin(N_j) - 2\left(N_i - N_j\right)\left(N_i + N_j\right) sin(N_i)\ sin(N_j)\right) A_i A_j \Bigg]. \qquad (4\text{-}28)$$

### *4.4.3. Normalized energy dissipated due to friction*

The dry friction between the beam and the walls is modeled using Coulomb model. The friction force is considered distributed over the contact surface. The energy dissipated due to friction depends on the developed normal pressure as well as contact length and displacement of the contact points. Dissipation of energy occurs only when the beam is in contact with the lateral walls (i.e. $\widehat{\omega}(x) = 0$ or $\widehat{\omega}(x) = h$). Hence, the dissipated energy can be expressed as:

$$w_f = \int_0^L \mu_k \hat{F}_n(x)\, \hat{u}(x) \left( H\left(-\hat{\omega}(x)\right) + H(\hat{\omega}(x) - h) \right) dx, \tag{4-29}$$

where $H(x)$ is the Heaviside function and $\mu_k$is the kinetic coefficient of friction. The normalized expression of the dissipated energy is expressed as:

$$W_f = \int_0^1 \mu_k F_n(X)\, U(X) \left( H\left(-W(X)\right) + H(W(X) - 1) \right) dX \tag{4-30}$$

where

$$W_f = \frac{w_f L^3}{EIh^2} \quad \text{and} \quad F_n(X) = \frac{\hat{F}_n(XL)\, L^3}{EI}. \tag{4-31}$$

Due to friction, the axial compression force inside the beam was shown to fluctuate in Section 2.5. Its expression is given by Equation (2-42) where $s_0 = 0$ and $\hat{N}_{s=s_0}$ is the compression force applied at the end which is equal to $\hat{p}$. Figure 4-3 displays the variation of the axial force inside the beam under different axial forces and corresponding buckling modes. In all cases the force variation is less than 1% of the applied load. The relative force variation was computed by $RV\% = 100 \times (\hat{N} - \hat{N}_{s=s_0})/\hat{N}_{s=s_0}$. Therefore, for simplification of the computation, the axial force inside the beam, $\hat{N}$, will be considered constant and equal to the applied force, $\hat{p}$.

The tangential force at contact zones is given by Equation (2-45). Assuming that the axial compression force inside the beam is constant and using non-dimensional variables expressed in Equations (4-8), (4-18) and (4-31), the friction induced tangential force can be simplified into

$$\mu_k F_n(X) = \frac{h}{L} \mu_k \left[ \frac{d^4 W(X)}{dX^4} + P \frac{d^2 W(X)}{dX^2} \right]. \tag{4-32}$$

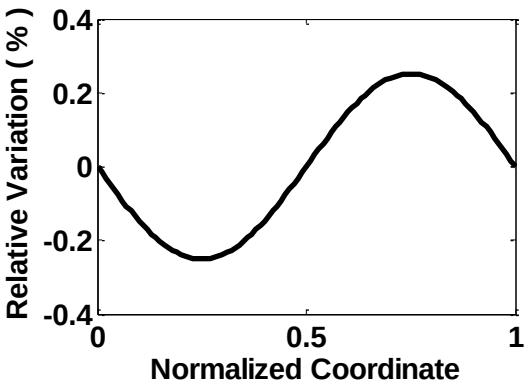


(a) 1st buckling mode, $\hat{p}$=300 N

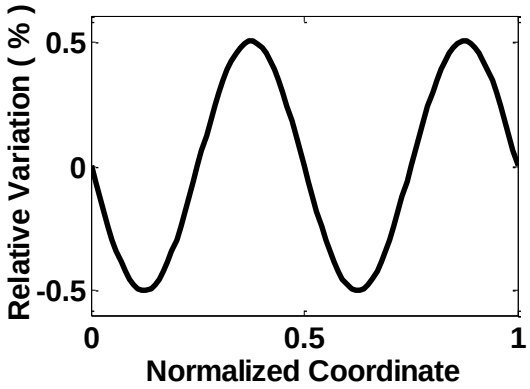


(b) 3rd buckling mode, $\hat{p}$=1000 N

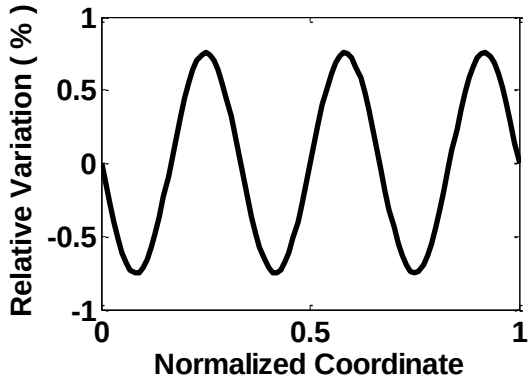


(c) 5th buckling mode, $\hat{p}$=2000 N

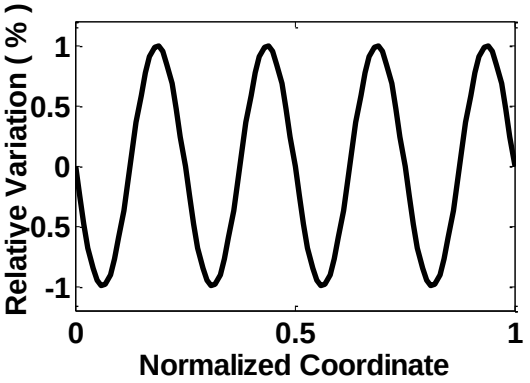


(d) 7th buckling mode, $\hat{p}$=2700 N

Figure 4-3: Variation of the axial force in the beam under different loading forces and corresponding buckling shapes.

Substituting Equations (4-19) in Equation (4-32) the tangential force is expressed in terms of the unknown coefficients, $A_j$, as:

$$\mu_k F_n(X) = \frac{h}{L}\mu_k \left( \sum_{j=1,3,5,\dots}^{\infty} \left(P - N_j^2\right) A_j \, N_j^2 \, cos\left(N_j X\right) + \sum_{j=2,4,6,\dots}^{\infty} \left(P - N_j^2\right) A_j \left(N_j^2 \, cos\left(N_j X\right) - 2N_j \, sin\left(N_j X\right)\right) \right). \quad (4\text{-}33)$$

On the other hand, from Equation (4-4) the displacement gradient over the beam is expressed as

$$\hat{u}'(x) = \varepsilon - \frac{1}{2}\left(\frac{d\hat{\omega}(x)}{dx}\right)^2 \tag{4-34}$$

Integrating Equation (4-34) between 0 and the $x$ coordinate yields the axial displacement field as

$$\hat{u}(x) = \int_0^x \left(\frac{\hat{p}}{EA} - \frac{1}{2}\left(\frac{d\hat{\omega}(x)}{dx}\right)^2\right) dx \tag{4-35}$$

Using the non-dimensional variables expressed in Equations (4-8) and (4-18), the normalized axial displacement field is expressed by:

$$U(X) = \frac{P}{12}Q^2X - \frac{1}{2}\int_0^X \left(\sum_{j=1}^{\infty} A_j \frac{\partial W_j(X)}{\partial X}\right)^2 dx$$

$$= \frac{P}{12}Q^2X - \frac{1}{2}\int_0^X \left(\sum_{j=1,3,5,\dots}^{\infty} A_j\ N_j sin\left(N_jX\right)\right.$$

$$\left. + \sum_{j=2,4,6,\dots}^{\infty} A_j\left(-2 + N_j\ sin\left(N_jX\right)\ + 2\ cos\left(N_jX\right)\right)\right)^2 dx$$

$$= \frac{P}{12} Q^2 X - \frac{1}{2}\Bigg[ \sum_{j=1,3,5,\ldots}^{\infty} \frac{N_j}{4} \left(2\, N_j\, X - \sin\left(2\, N_j\, X\right)\right) A_j^2 + \sum_{i=2,4,6,\ldots}^{\infty} \Bigg( -3 + 4\cos(N_i\, X)$$

$$- \frac{-2\mathrm{N_i}(12 + \mathrm{N_i^2})\, X + 4\,\mathrm{N_i}\cos(2\mathrm{N_i}\, X) + 32\sin(\mathrm{N_i} X) + (-4 + \mathrm{N_i^2})\sin(2\mathrm{N_i}\, X)}{4\mathrm{N_i}} \Bigg) A_i^2$$

$$+ 2 \sum_{i=1,3,5,\ldots}^{\infty} \sum_{j=3,5,7,\ldots>i}^{\infty} \frac{\mathrm{N_i}\, \mathrm{N}_j \left(\mathrm{N_j}\cos\left(\mathrm{N_j}\, \mathrm{X}\right)\sin(\mathrm{N_i}\, \mathrm{X}) - \mathrm{N_i}\cos(\mathrm{N_i}\, X)\sin\left(\mathrm{N_j}\, X\right)\right)}{\mathrm{N_i^2} - \mathrm{N_j^2}} A_i A_j$$

$$+ 2 \sum_{i=1,3,5,\ldots}^{\infty} \sum_{j=2,4,6,\ldots}^{\infty} \frac{1}{\mathrm{N_i^2} - \mathrm{N_j^2}} \Big( -\cos(\mathrm{N_i}\, X)\left(-2\mathrm{N_i^2} + 2\mathrm{N_j^2} + 2\mathrm{N_i^2}\cos\left(\mathrm{N_j}\, X\right)\right.$$

$$\left. + \mathrm{N_i^2 N_j}\sin\left(\mathrm{N_j}\, X\right)\right) + \mathrm{N_j}\Big(2\mathrm{N_j} + \mathrm{N_i}\, \mathrm{N_j}\cos\left(\mathrm{N_j}\, X\right)\sin(\mathrm{N_i}\, X)$$

$$- 2\mathrm{N_i}\sin(\mathrm{N_i}\, X)\sin\left(\mathrm{N_j}\, X\right)\Big)\Big) A_i A_j + 2 \sum_{i=2,4,6,\ldots}^{\infty} \sum_{j=4,6,8,\ldots>i}^{\infty} \Bigg( -2$$

$$- \frac{1}{4\mathrm{N_i}\left(\mathrm{N_i} - \mathrm{N_j}\right)\mathrm{N_j}\left(\mathrm{N_i} + \mathrm{N_j}\right)\left(-2 + \mathrm{N_i}\cot\left(\frac{\mathrm{N_i}\, X}{2}\right)\right)\left(-2 + \mathrm{N_j}\cot\left(\frac{\mathrm{N_j}\, X}{2}\right)\right)} \Bigg( \csc\left(\frac{\mathrm{N_i}\, X}{2}\right)^2$$

$$\times \csc\left(\frac{\mathrm{N_j}\, X}{2}\right)^2 (-2 + 2\cos(N_i\, X) + \mathrm{N_i}\sin(N_i\, X))\left(-2 + 2\cos\left(N_j\, X\right)\right.$$

$$\left. + \mathrm{N_j}\sin\left(N_j\, X\right)\right)\Bigg( -\mathrm{N_i N_j}\cos\left(\mathrm{N_j}\, X\right)\left(2\left(\mathrm{N_i^2} - \mathrm{N_j^2}\right) + \mathrm{N_i}\left(4 + \mathrm{N_j^2}\right)\sin(N_i\, X)\right)$$

$$+ \mathrm{N_i N_j}\cos(\mathrm{N_i}\, X)\left(-2\mathrm{N_i^2} + 2\mathrm{N_j^2} + 2\left(\mathrm{N_i^2} - \mathrm{N_j^2}\right)\cos\left(N_j\, X\right) + (4 + \mathrm{N_i^2})\mathrm{N_j}\sin\left(N_j X\right)\right)$$

$$+ 4\left(\mathrm{N_i^2} - \mathrm{N_j^2}\right)\Big(\mathrm{N_j}\sin(\mathrm{N_i} X) + \mathrm{N_i}\left(-\mathrm{N_j}\, X + \sin\left(\mathrm{N_j}\, X\right)\right)\Big)\Bigg)\Bigg) A_i A_j \Bigg]. \qquad (4\text{-}36)$$

Similarly to the compression force inside the beam, the axial displacement field can be reduced to the first linear term, $\mathrm{P\,Q^2\,X/12}$, and the displacements due to mid-plane rotation can be neglected. Therefore the energy dissipated due to friction is expressed as

$$W_f = \mu_k \frac{h}{L} \frac{PQ^2}{12} \int_0^1 X \left( \sum_{j=1,3,5,\dots}^{\infty} \left(P - N_j^2\right) A_j \, N_j^2 \, cos\left(N_j X\right) + \sum_{j=2,4,6,\dots}^{\infty} \left(P - N_j^2\right) A_j \right.$$

$$\left. \times \left(N_j^2 \, cos\left(N_j X\right) - 2N_j \, sin\left(N_j X\right)\right) \right) \left(H\left(-W(X)\right) + H(W(X) - 1)\right) dX \qquad (4\text{-}37)$$

Due to the existence of the Heaviside function that ensures that the dissipation of energy occurs only at the contact zones, the integral in Equation (4-37) is computed numerically to approximate the energy $W_f$.

## 4.5. Frictionless static model

In this study, the beam is placed adjacent to one of the lateral walls. Hence, it deflects only in the direction of the other constraint when it buckles in the first mode. Moreover, in this section, the contact between the beam and the lateral constraints is considered frictionless. Therefore, the transverse deflection can be expressed as a linear combination of only symmetric modes as

$$W(X) = \sum_{j=1}^{\infty} A_j \left(1 - cos\left(N_j X\right)\right) \qquad (4\text{-}38)$$

where $\mathrm{N_j = 2j\pi}$.

The normalized end shortening, work of external force, bending strain energy and compression strain energy are reduced, respectively, to

$$d = \delta + \frac{1}{4}\sum_{j=1}^{\infty} A_j^2 N_j^2 \tag{4-39}$$

$$V_P = -\frac{P}{2}\left[\delta + \frac{1}{4}\sum_{j=1}^{\infty} A_j^2 N_j^2\right] \tag{4-40}$$

$$V_b = \frac{1}{4}\sum_{j=1}^{\infty} A_j^2 N_j^4 \tag{4-41}$$

$$V_c = \frac{6}{Q^2}\delta^2 \tag{4-42}$$

In order to determine the deflected shape of the beam under axial loading, the potential energy is minimized with respect to $A_j$. Lateral constraints allow the beam to undergo higher modes, rather than buckle in the first mode only. The presence of the lateral walls can be modeled mathematically as a constraint imposed on the transverse deflection. Therefore, the deflection is always bounded by the distance between the walls. The constrained minimization problem of the potential energy can be expressed as

$$\begin{cases} Min\ \Pi(A_j) \\ 0 \le W(X) \le 1 \end{cases} \tag{4-43}$$

where $\Pi = V_b + V_c + V_p$ is the normalized total potential energy.

The problem is then solved for the coefficients $A_j$ that will simultaneously generate an accurate representation of the deformations at each loading state, determine the balance of energies, and the exact mode transition points. Figure 4-4 displays the normalized deflected shapes of the beam determined by the presented model under increasing axial load up to the fifth mode. The dimensions and the material properties of the beam used for all the theoretical results are summarized in Table 3-1. Under increasing load the beam deflects until it touches the opposite constraint at a single point ($P$ = 89), it flattens ($P$ = 390) and then snaps into the third mode ($P$ =

410). Flattening of the contact zones can be also seen before the transition to the fifth mode ($P$ =1020).

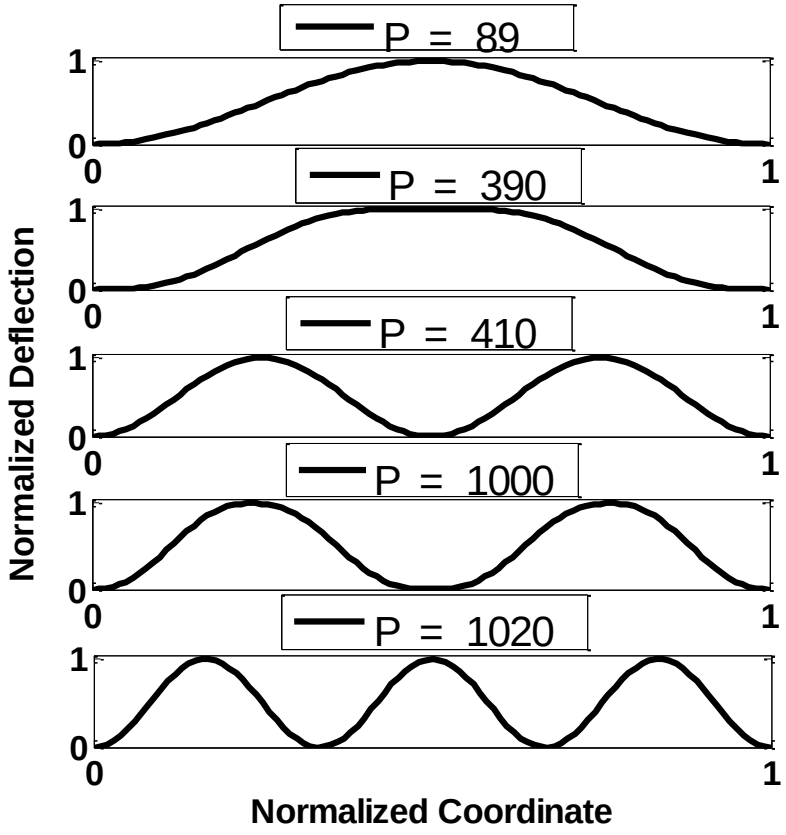


Figure 4-4: Deflected shape for increasing axial load.

*4.5.1. Force-control formulation*

In this section the beam shown in Figure 4-1 is subjected to a gradually-increased axial force $\hat{p}$. Axial shortening $\Delta_c$ due to the axial load can be expressed as

$$\Delta_c = \frac{\hat{p}L}{EA} \tag{4-44}$$

Substituting Equation (4-18) into Equation (4-44) yields

$$\delta = \frac{P}{12} Q^2 \tag{4-45}$$

Inserting Equation (4-45) into Equations (4-39) - (4-42), the non-dimensional midplane stretching and potential energies are expressed as

$$d = \frac{P}{12} Q^2 + \frac{1}{4} \sum_{j=1}^{\infty} A_j^2 N_j^2 \tag{4-46}$$

$$V_P = -\frac{P^2}{24} Q^2 - \frac{P}{8} \sum_{j=1}^{\infty} A_j^2 N_j^2 \tag{4-47}$$

$$V_b = \frac{1}{4} \sum_{j=1}^{\infty} A_j^2 N_j^4 \tag{4-48}$$

$$V_c = \frac{P^2}{24} Q^2 \tag{4-49}$$

Therefore, the total potential energy can be expressed in terms of P and $A_j$ as

$$\Pi = \frac{1}{4} \sum_{j=1}^{\infty} A_j^2 N_j^4 - \frac{P}{8} \sum_{j=1}^{\infty} A_j^2 N_j^2 \tag{4-50}$$

Figure 4-5 displays the model predictions and experimental measurements, from the setup shown in Figure 3-1, of the force-displacement response of the beam under incremental quasi-static axial force loading. A comparison with the study developed by Chai (1998) is presented in Figure 4-6. The study was summarized in section 2-4. Chai's model can adequately capture the system stiffness but the mode transitions are incrementally overestimated and the model becomes increasingly inaccurate as the number of buckled waves increases. The developed static model, which is based on the minimization of the potential energy, predicts better the loading forces and displacements at which transitions occur and has a better agreement with the experimental results.

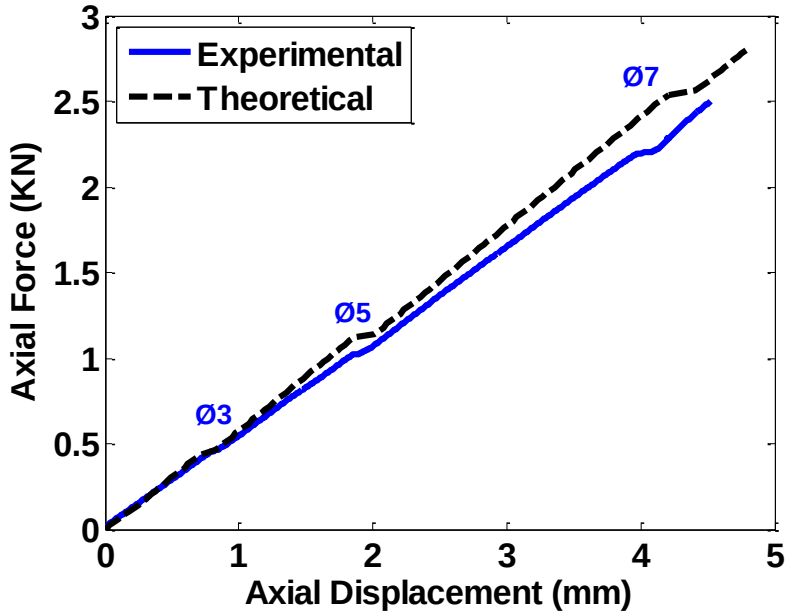


Figure 4-5: Theoretical and experimental Force-displacement response under force-control loading.

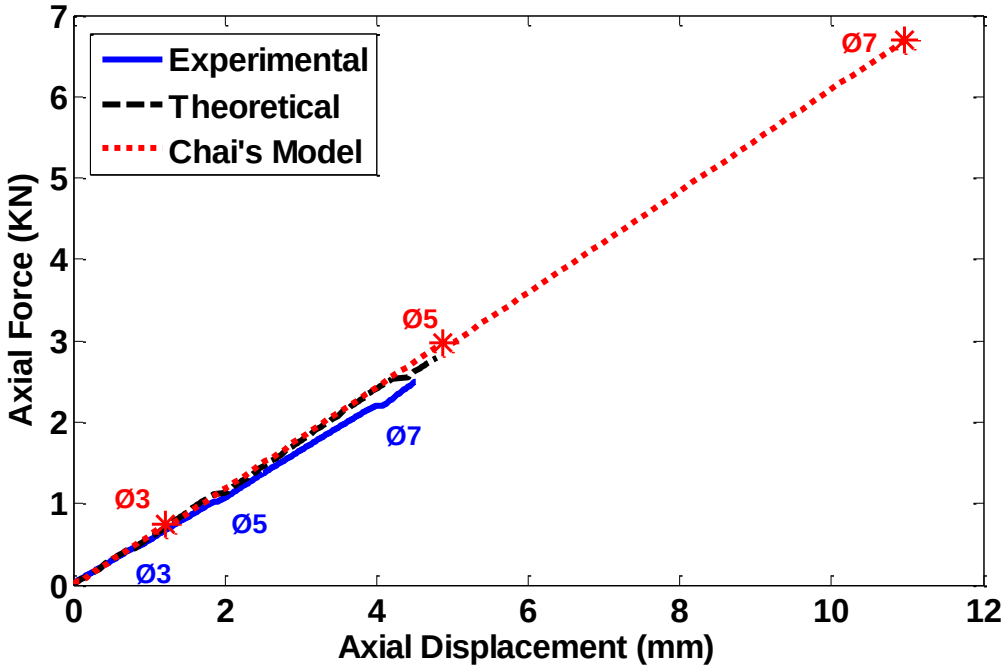


Figure 4-6: Comparison between the presented static model and Chai's model (Chai 1998).

*4.5.2. Displacement-control formulation*

In this section the beam shown in Figure 4-1 is subjected to a gradually-increasing axial displacement $\Delta$. The axial force $\hat{p}$ due to the prescribed axial displacement can be expressed as

$$\hat{p} = \frac{EA}{L}(\Delta - \frac{1}{2}\int_0^L \left(\frac{dw}{dx}\right)^2 dx) \tag{4-51}$$

Substituting Equation (4-18) into Equation (4-51), the non-dimensional axial force is expressed by

$$P = \frac{12}{Q^2}\left(d - \frac{1}{4}\sum_{j=1}^{\infty} A_j^2 N_j^2\right) \tag{4-52}$$

Substituting Equation (4-52) into Equations (4-39) - (4-42), the non-dimensional midplane stretching and potential energies are expressed as

$$\delta = d - \frac{1}{4}\sum_{j=1}^{\infty} A_j^2 N_j^2 \tag{4-53}$$

$$V_P = -\frac{6}{Q^2}\left(d^2 - \frac{d}{4}\sum_{j=1}^{\infty} A_j^2 N_j^2\right) \tag{4-54}$$

$$V_b = \frac{1}{4}\sum_{j=1}^{\infty} A_j^2 N_j^4 \tag{4-55}$$

$$V_c = \frac{6}{Q^2}\left(d^2 - \frac{d}{2}\sum_{j=1}^{\infty} A_j^2 N_j^2\right) \tag{4-56}$$

Therefore the total potential energy can be expressed in terms of d and $A_j$ as

$$\Pi = \frac{1}{4}\sum_{j=1}^{\infty} A_j^2 N_j^4 - \frac{3}{2}\frac{d}{Q^2}\sum_{j=1}^{\infty} A_j^2 N_j^2 \tag{4-57}$$

Theoretical and experimental force-displacement responses of the beam subjected to incremental quasi-static axial displacement loading are displayed in Figure 4-7. The response predictions from the developed model correlate with the actual observed experimental behavior.

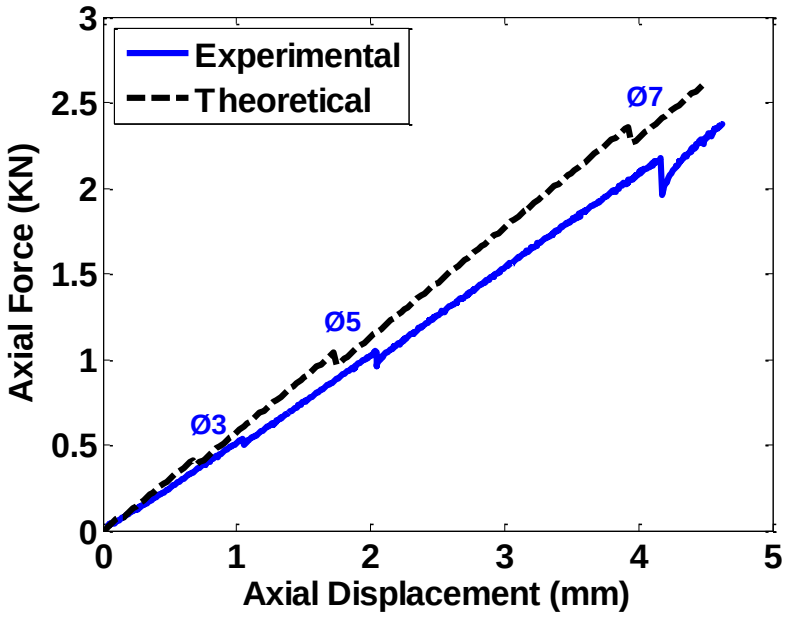


Figure 4-7: Theoretical and experimental force-displacement response under displacement-control loading.

## 4.6. Dynamic analysis

Snap-through buckling from one mode into a higher or lower mode configuration is induced when the total energy transitions through an unstable path to a lower value represented by a different stable geometric configuration. The difference in energies is released as kinetic energy. A dynamic model was then developed to investigate the released kinetic energy as well as accelerations of the beam during transitions. The presented model was developed based on the force-control formulation presented in Section 3.5.1, but displacement-control can also be used for this study.

In this analysis friction is neglected. Therefore, the total energy at any equilibrium state is the sum of the kinetic and the potential energies. The normalized kinetic energy, K, is expressed in Equation (4-22) and the total potential energy, Π, is the sum of the potential energy due to external force and the axial compression and bending strain energies expressed, respectively, in Equations (4-25), (4-26) and (4-28). The constrained minimization problem of the total energy can be expressed as

$$\begin{cases} Min\ \mathrm{K} + \Pi \\ 0 \le W(x) \le 1 \end{cases} \tag{4-58}$$

The beam is subjected to a linearly increasing and decreasing load, $\hat{p}$, such that

$$\hat{p} = \begin{cases} \hat{p}_{max} \dfrac{\hat{t}}{T/2} & if\ \ 0 \le \hat{t} \le T/2 \\ \hat{p}_{max} \left( 2 - \dfrac{\hat{t}}{T/2} \right) & if\ \ T/2 \le \hat{t} \le T \end{cases} \tag{4-59}$$

where T is the loading period, $\hat{p}_{max}$ is the maximum applied load and $\hat{t}$ is the time coordinate. The variation of the axial loading force, $\hat{p}$, with respect to time, $\hat{t}$ is displayed in Figure 4-8.

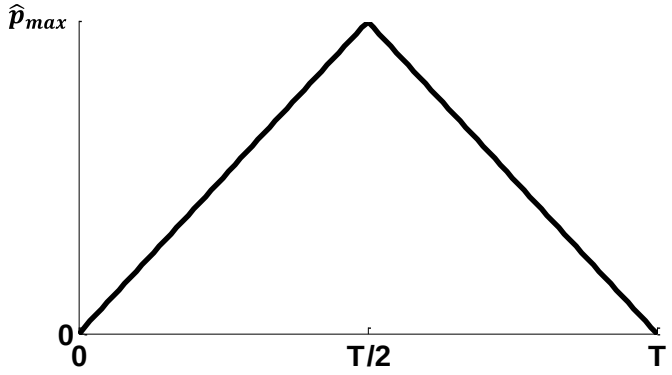


Figure 4-8: Variation of axial loading force, $\hat{p}$.

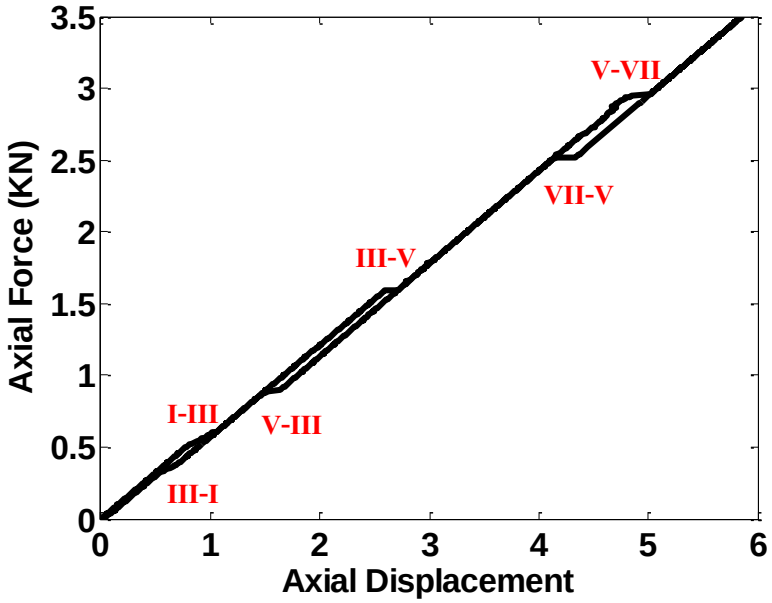


Figure 4-9: Dynamic force-displacement response under force-controlled cyclic loading.

Figure 4-9 displays the simulated dynamic force-displacement response of the beam under cyclic force loading. The loading period, T, is 10 s and the maximum applied force, $\hat{p}_{max}$, is 3500 N. Results show that, during unloading, the beam returns to a lower buckling mode through a different equilibrium path. The symbols I-III, III-V, V-VII, VII-V, V-III and III-I denote the transitions between the buckling modes; for example I-III denotes the transition from the first into the third mode. The normalized axial displacement, $d$, kinetic energy, $K$, and accelerations, $A$, over a loading cycle are presented in Figure 4-10. The normalized acceleration is given by

$$A = \frac{m\,L^4}{hEI}\,\hat{A} = \frac{\partial^2 W(X,t)}{\partial t^2} \tag{4-60}$$

where $\hat{A} = \partial^2 \widehat{W}(x,\hat{t})/\partial \hat{t}^2$ is the transverse acceleration. Snap-through transitions are witnessed by the jumps in the axial displacement response and the spikes in the kinetic energy and accelerations.

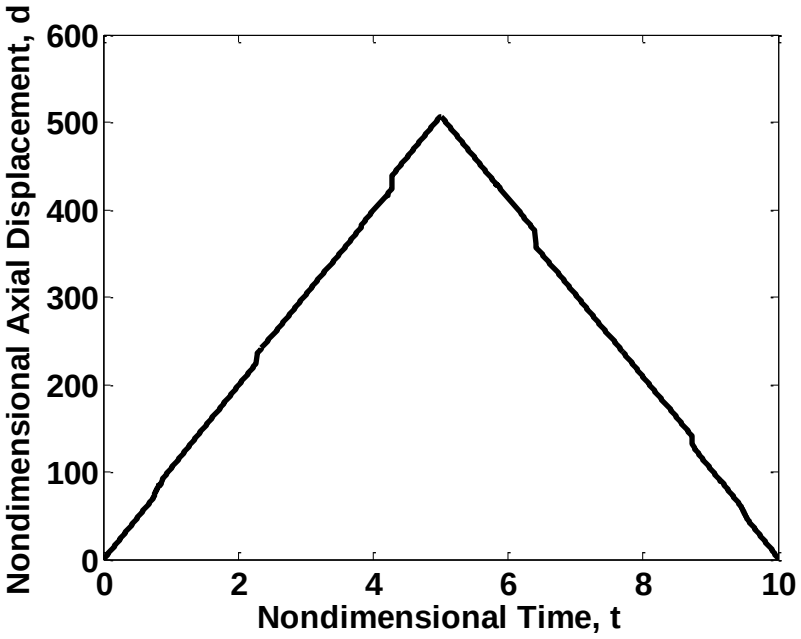


(a)

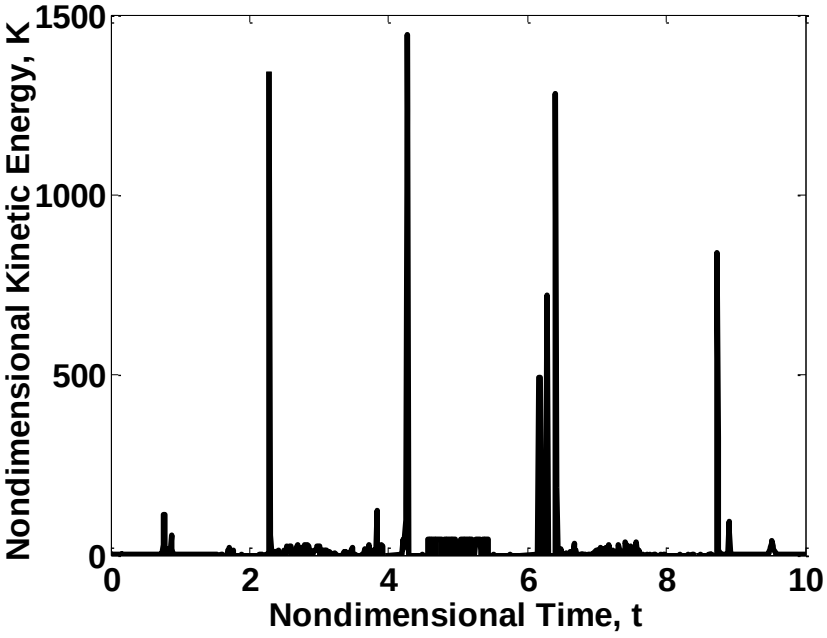


(b)

Figure 4-10: (a) Displacement response, (b) released kinetic energy and (c) generated accelerations during one loading cycle.

Figure 4-10 (cont'd)

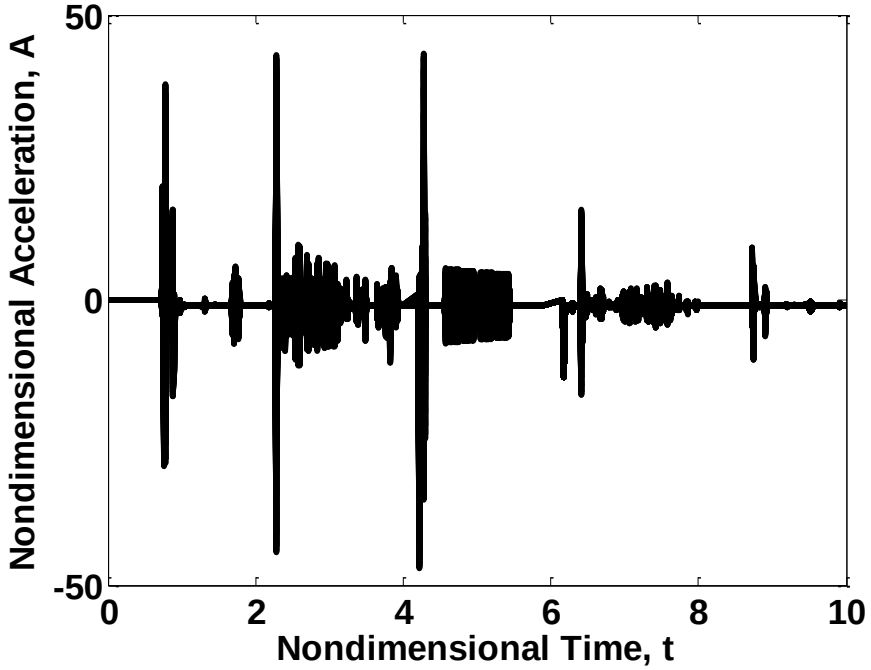


(c)

The deflected shapes of the beam before and after each transition are shown in Figure 4-11. It can be noticed that the deflected beam is not symmetric and the snap does not always occur at the same location. Figure 4-12 displays the distance, $W_R = W_f - W_i$, that the beam travels at each transition where $W_i$ and $W_f$ represent, respectively, the deflected shapes before and after transitions. The normalized values and locations of the maximum relative displacement at transitions are presented in Table 4-1. Opposite transitions occur at the same location with opposite maximum displacement sign except for I-III and III-I. For example, in transitions V-VII and VII-V, maximum displacements are located at 0.37 X-coordinate, but with opposite sign. Similarly, transitions III-V and V-III have maximum displacements located approximately at 0.68 X-coordinate. However, transitions I-III and III-I occur at different locations (0.21 and 0.5, respectively) with the same maximum displacement sign.

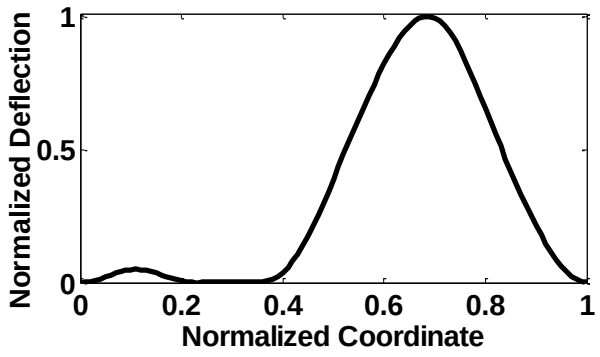


(a) before transition I-III.

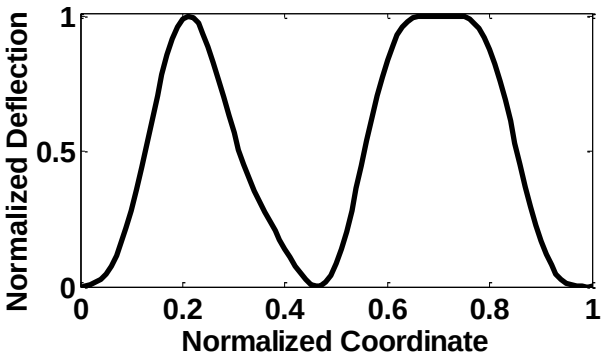


(b) after transition I-III.

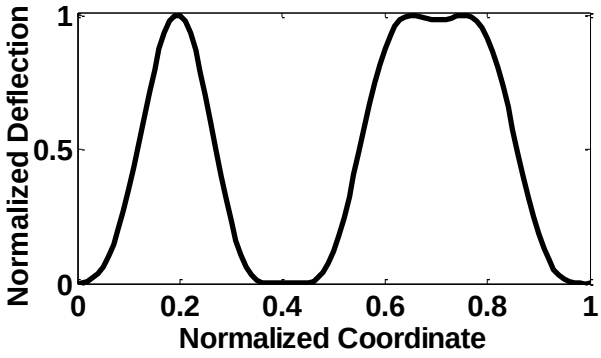


(c) before transition III-V.

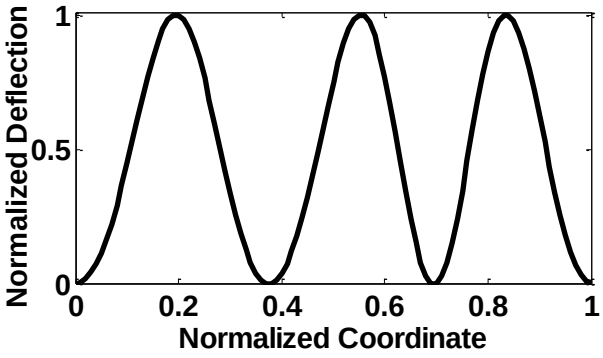


(d) after transition III-V.

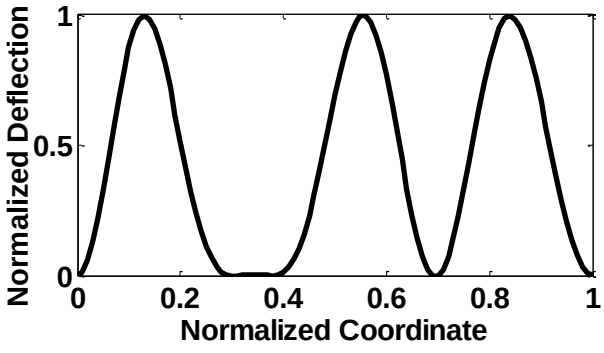


(e) before transition V-VII.

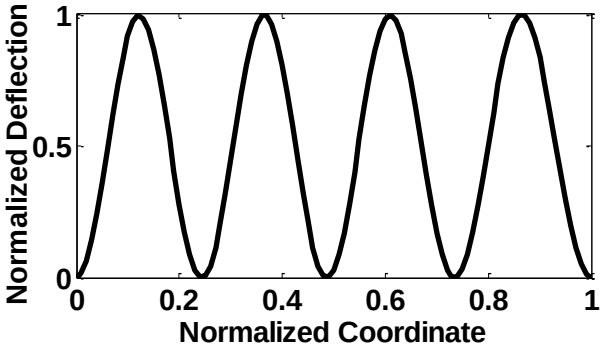


(f) after transition V-VII.

Figure 4-11: Deflected shapes before and after each mode transition.

Figure 4-11 (cont'd)

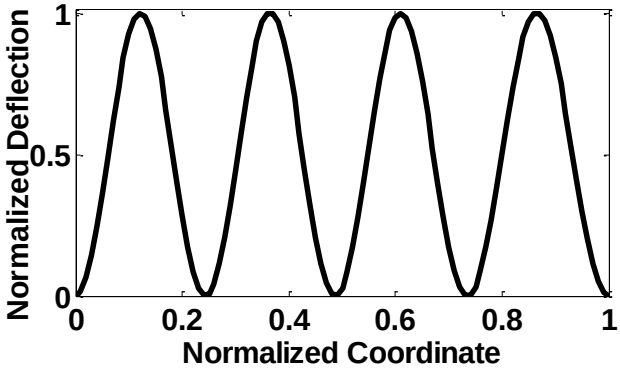


(g) before transition VII-V.

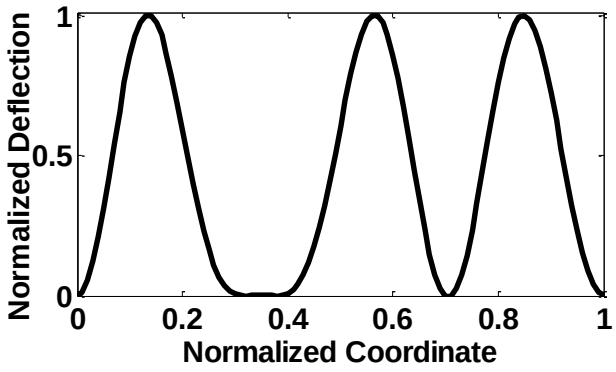


(h) after transition VII-V.

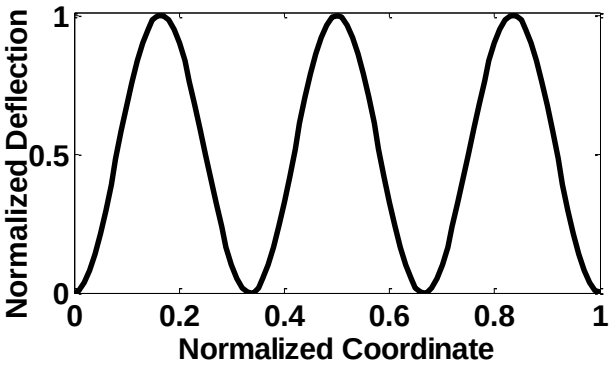


(i) before transition V-III.

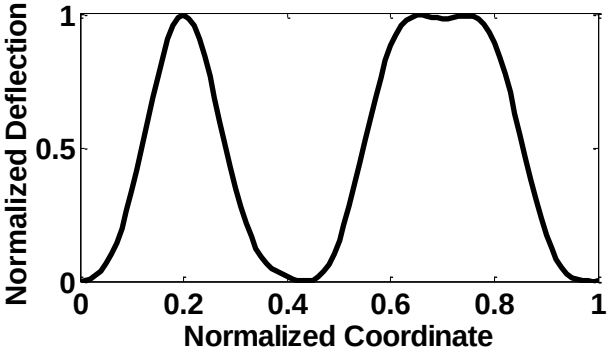


(j) after transition V-III.

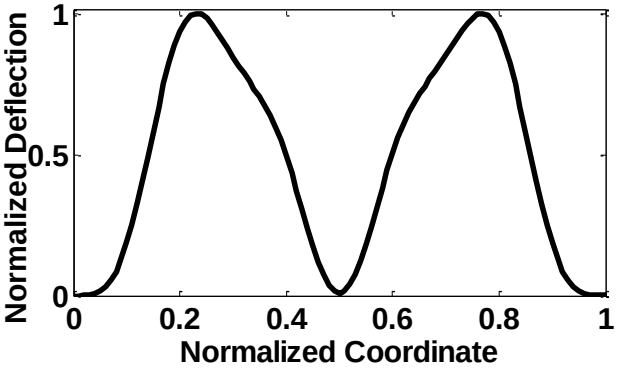


(k) before transition III-I.

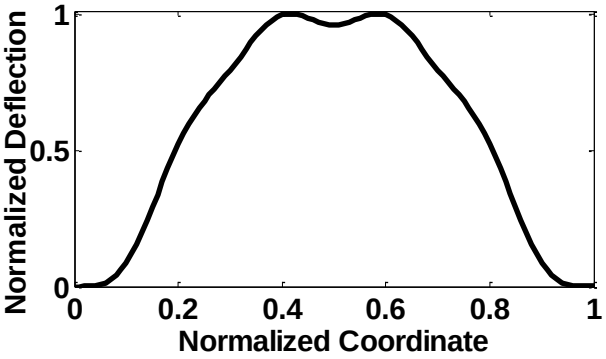


(l) after transition III-I.

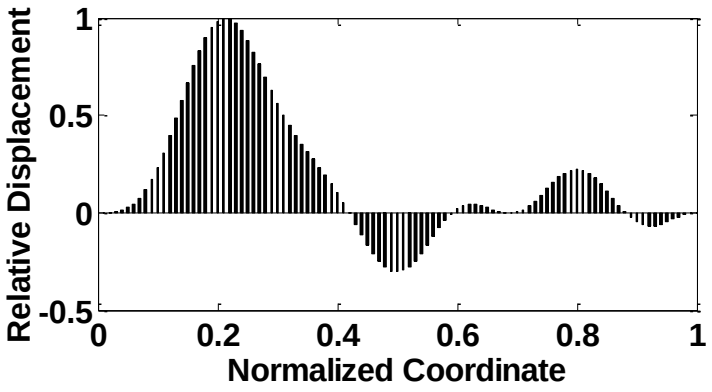


(a) Relative displacement, $W_R$, at transition I-III.

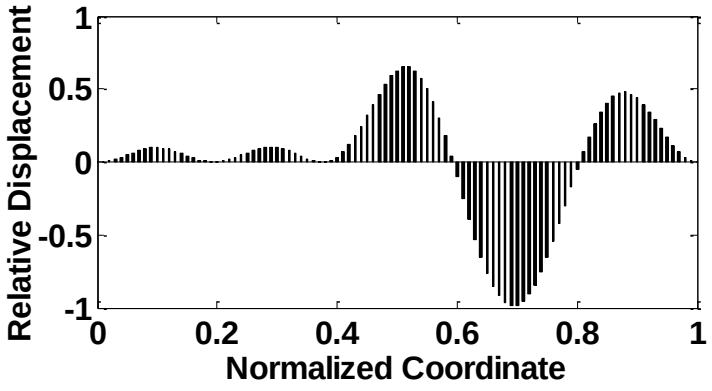


(b) Relative displacement, $W_R$, at transition III-V.

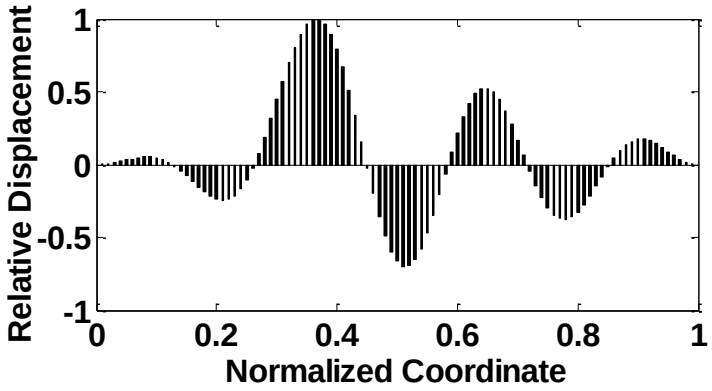


(c) Relative displacement, $W_R$, at transition V-VII.

Figure 4-12: Relative displacement, $\boldsymbol{W_R = W_f - W_i}$, at mode transitions where $\boldsymbol{W_i}$ and $\boldsymbol{W_f}$ represent, respectively, the deflected shapes before and after transitions.

Figure 4-12 (cont'd)

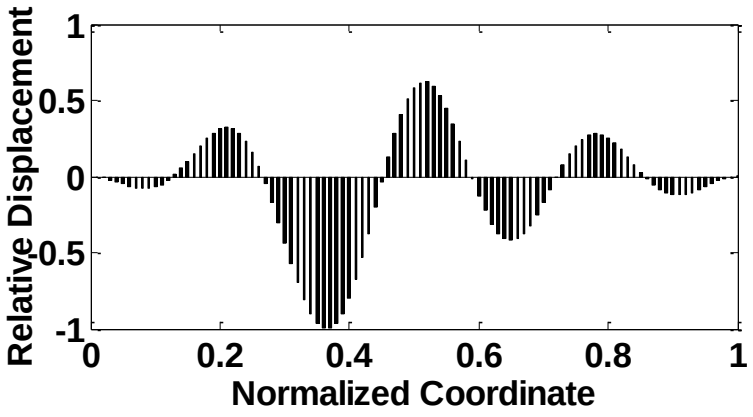


(d) Relative displacement, $W_R$, at transition VII-V.

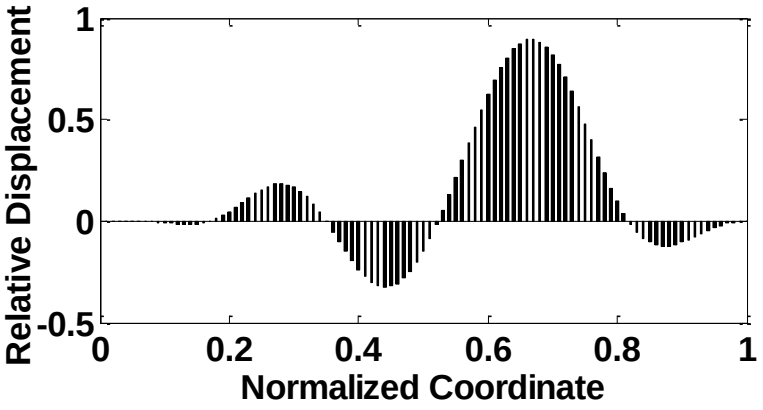


(e) Relative displacement, $W_R$, at transition V-III.

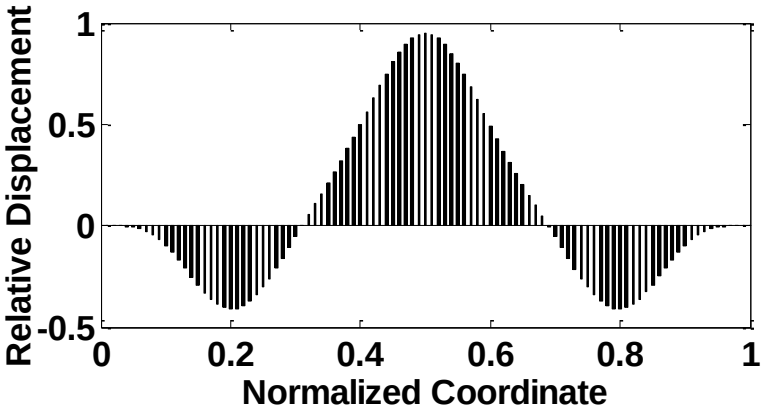


(f) Relative displacement, $W_R$, at transition III-I.

Table 4-1: Value and location of the maximum displacement at transitions.

| Mode transitions | Maximum displacement during transitions | Normalized X-coordinate of the maximum displacement |
|---|---|---|
| I-III | 0.997 | 0.21 |
| III-V | -0.984 | 0.69 |
| V-VII | 1 | 0.37 |
| VII-V | -1 | 0.37 |
| V-III | 0.895 | 0.67 |
| III-I | 0.942 | 0.5 |

The points located at 0.21, 0.37, 0.5 and 0.69 exhibit the maximum displacements during mode transitions. Their accelerations over the loading cycle are displayed in Figure 4-13. Results show that the accelerations generated during loading are much higher than unloading. Moreover, the accelerations generated during the transitions III-V and V-VII are comparable (Figure 4-13 (b) and (d)) but higher than I-III. The location X = 0.37 snaps only in the transitions between the fifth and seventh mode and the location X = 0.21 provide low accelerations during mode switching. Therefore locations X = 0.5 and X = 0.69 are better candidates to attach the energy scavenger to the bilaterally constrained beam.

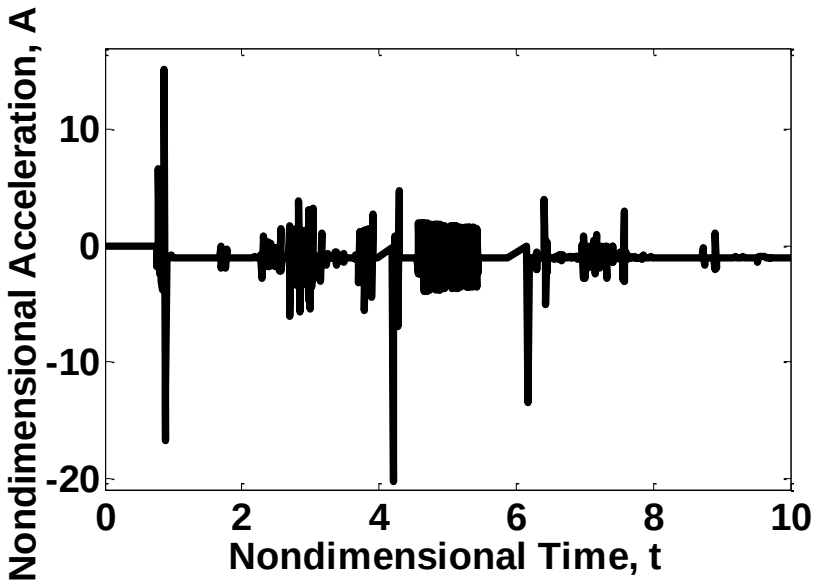


(a) Accelerations at X=0.21.

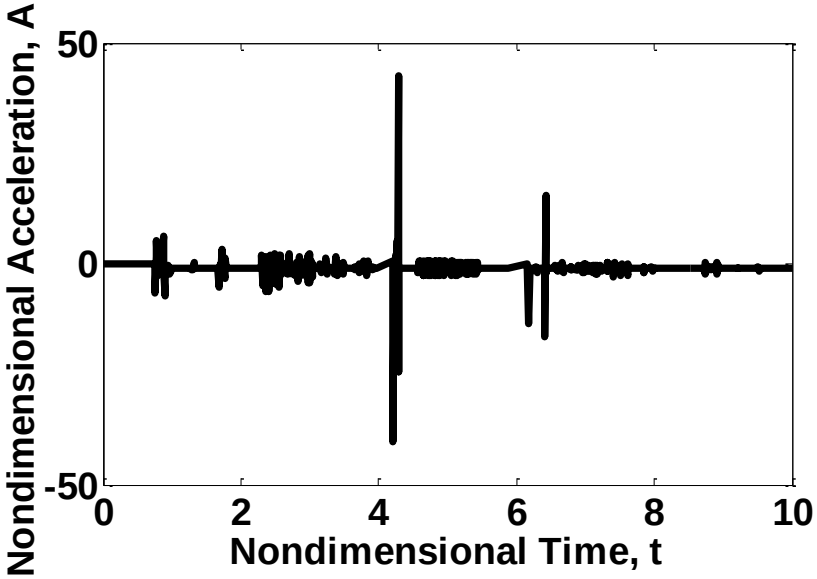


(b) Accelerations at X=0.37.

Figure 4-13: Non-dimensional accelerations at the locations (a) X = 0.21, (b) X = 0.37, (c) X = 0.5 and (d) X = 0.69 during a loading cycle of 10 s.

Figure 4-13 (cont'd)

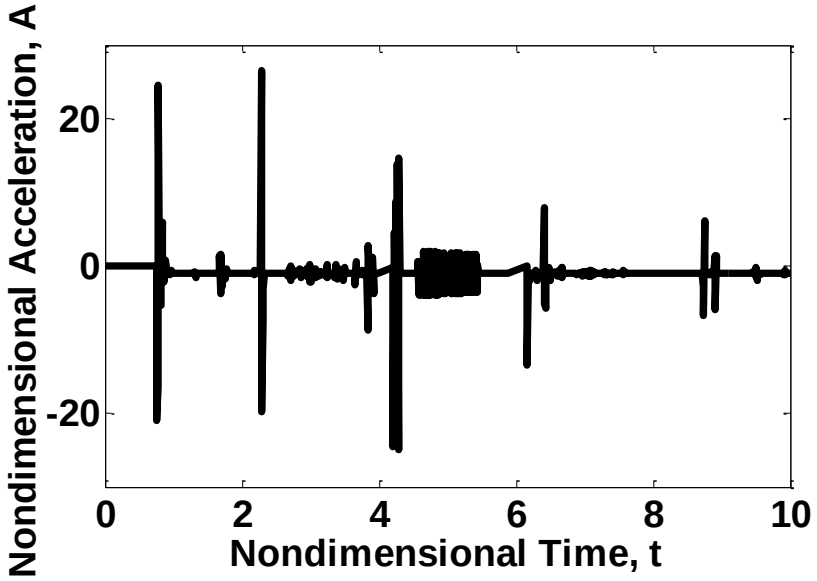


(c) Accelerations at X=0.5.

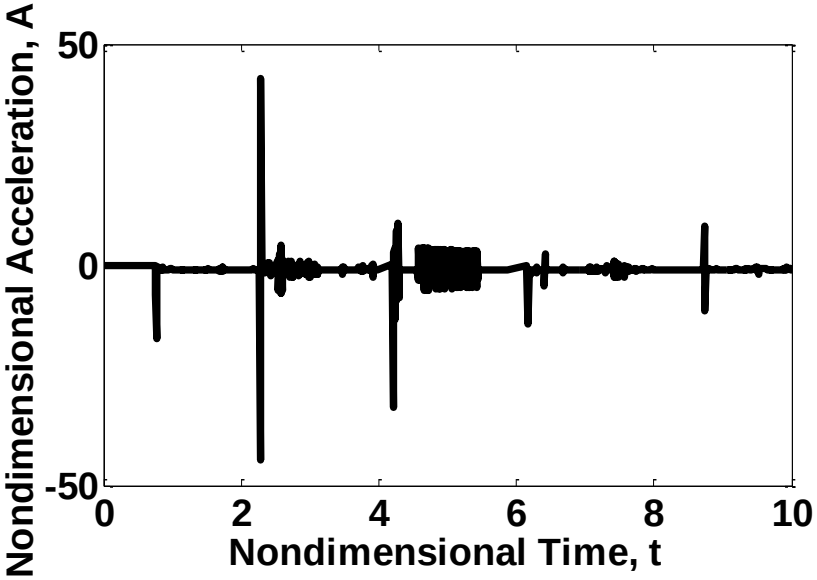


(d) Accelerations at X=0.69.

## 4.7. Summary

The post-buckling response of a bilaterally constrained beam subjected to axial force and displacement was theoretically investigated using energy methods. In contrast to previous studies that are based on geometric elliptic integrations, this study was based on the minimization of energy under constraints. The theoretical model presented in this work shows that energy methods, based on the physics of the device, significantly improve understanding of the system behavior and improve the correlation with respect to experimental measurements. The model accounts for longitudinal deformations and friction between the beam and its lateral constraints.

Using the Galerkin discretization method, the deflection is expressed as a linear combination of the buckling eigen modes. The total energy is then minimized under the confinement constraint in order to determine the unknown coefficients multiplying the buckling modes. The static response of the beam was investigated using force- and displacement-control formulations. The force-displacement response as well as the deflected shapes under axial loadings were determined. Results show that the model is able to adequately predict the beam geometry at every loading stage, including the flattening behavior just before the snap buckling transitions, and simultaneously determines the mode transition events.

A dynamic analysis based on a force-control formulation was carried out to investigate the released kinetic energy as well as accelerations of the beam during transitions. The beam was subjected to a cyclic triangular axial force and the constrained minimization problem of the total energy was solved. It was shown that the beam returns to lower buckling configurations through a different equilibrium path. Moreover, the buckling transitions create high kinetic energy and acceleration spikes. However, the location of maximum acceleration differs from one transition to another. Hence, placement of the piezoelectric energy harvester should be carefully chosen

depending on the application. The dissipated energy due to friction was formulated but not included in the analysis because the computation becomes very expensive. Future developments will address the optimization of the algorithm to investigate friction effects.

# CHAPTER 5: ENERGY HARVESTING AND SENSING BASED ON QUASI-STATIC MECHANICAL ENERGY CONCENTRATORS AND TRIGGERS [3]

## 5.1. Introduction

Many real world-physical processes occur at very low frequencies and acceleration levels. Examples of these processes comprise, among others, temperature and pressure variation between day and night as well as bone healing and spinal fusion in biomedical engineering. These processes induce a stress/strain response that occur at frequencies lower than 1 mHz. Monitoring the evolution of quasi-static strain is important and could provide significant benefits. For instance, the history of mechanical loading inside different structures could be used to predict the life expectancy of the structure. This chapter presents a battery-less sensor design that can self-power by harvesting energy directly from the quasi-static events being sensed.

The technical challenge is illustrated for a piezoelectricity driven self-powered sensor whose generic architecture is shown in Figure 5-1 (a). The sensor comprises of a piezoelectric transducer that powers a minimal set of electronic modules by harvesting energy from ambient strain variations. Typically the sensor electronics comprises of: (a) a rectification module to extract energy from the transducer; (b) a triggering module that detects events of interest; and (c) a data-logging module that records events either on a non-volatile memory or using remote data

[3] Results shown in this chapter were published in Lajnef et al. (2013, 2014a, 2014b, 2014c, 2014d and 2014e).

transmission. When the piezoelectric transducer is excited quasi-statically (as shown in Figure 5-1 (b) by the triangular wave) the load voltage generated by the transducer is approximately constant as shown in Figure 5-1 (b). Assuming a nominal sized piezoelectric transducer, the power levels that can be scavenged from mHz strain-signal would be in the order of pico-watts (Sarkar et al. 2013). Unfortunately, the majority of the charge generated by the transducer is lost as leakage through the electronics (for example through diode leakage) and the residual energy is insufficient to drive the rest of the sensor modules (triggering and data-logging modules).

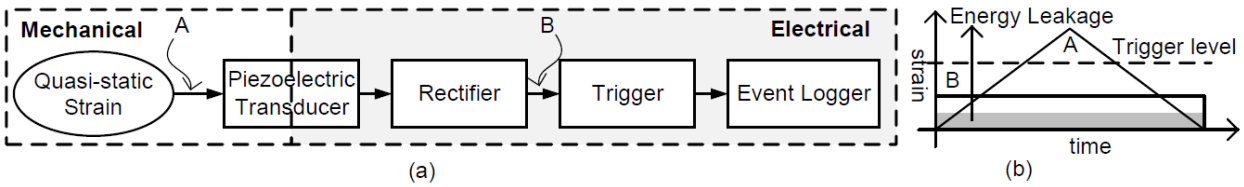


Figure 5-1: (a) System architecture of a generic piezoelectricity driven self-powered sensor; and (b) adverse effect of electronic leakage on energy scavenging for quasi-static excitation.

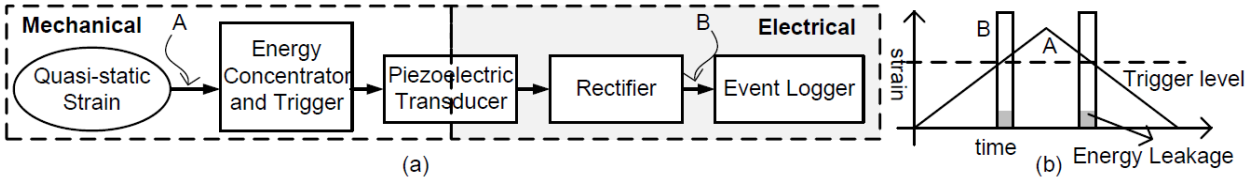


Figure 5-2: (a) System architecture of the proposed self-powered sensor comprising of mechanical energy concentrators; and (b) reduction of electronic leakage during the impulsive energy release of the energy concentrators.

This chapter presents the use of mechanical energy concentrators and triggers as a front-end to circumvent the challenge of quasi-static self-powering. The architecture of the proposed sensor is shown in Figure 5-2 (a) and its principle of operation is illustrated for a simplified loading condition in Figure 5-2 (b). The role of the mechanical energy concentrator is to harvest potential

energy over a long time-span and release the stored energy as bursts and impulses as shown in Figure 5-2 (b). The impulsive nature of the energy-release not only results in piezoelectric output voltage levels that are significantly higher than the triggering but also reduces the effect of energy leakage as shown in Figure 5-2 (b).

This chapter is organized as follows: Section 5.2 presents the principle of operation of the proposed self-powered sensor and Section 5.3 describes the design and characterization of the front-end mechanical energy concentrator. Section 5.4 briefly describes the sensor electronics used for self-powered data-logging and present measurement results obtained from fabricated prototypes.

## 5.2. Principle of operation

The physics and principle of operation of the sensor is illustrated in Figure 5-3 (a)-(c) using a bilaterally constrained elastic beam which is subjected to a quasi-static force F. Figure 5-3 (d) shows an energy diagram schematic that indicates the potential energy stored in the elastic beam as the magnitude of the quasi-static force (F) is increased. Note that under quasi-static loading conditions no energy is dissipated as kinetic energy or heat except during snap buckling events. Assuming that the beam is initially in an energy configuration denoted by state A, increasing the magnitude of the input signal shifts the configuration to a higher potential energy state B. The state B corresponds to the position of the beam shown in Figure 5-3 (a). Because the beam is bilaterally constrained (at point Y), increasing the magnitude of the input signal (F) buckles the beam to another state shown in Figure 5-3 (b). On the energy-diagram shown in Figure 5-3 (d), the mechanical buckling results in a negative-energy slope at state B, where part of the stored potential energy is released instantly as kinetic energy, before the beam buckles to a lower energy state C.

If a piezoelectric transducer is attached to the structure, part of the kinetic energy is transferred to the transducer which is then scavenged for sensing and computation. The impulsive nature of the energy-release not only results in higher piezoelectric output voltage (due to the high frequency transition) but also significantly reduces the effect of electronic leakage.

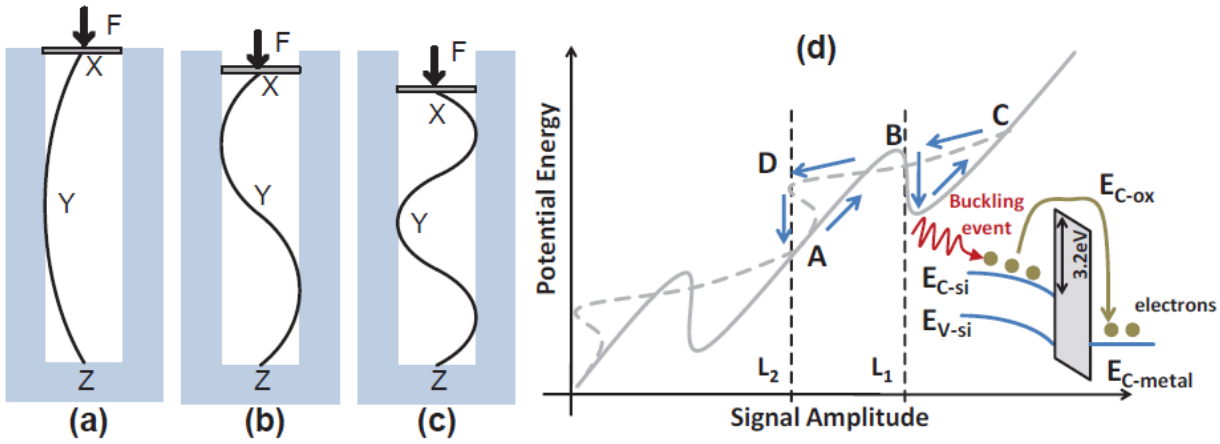


Figure 5-3: Principle of operation of the proposed self-powered sensor: (a)-(c) different buckling states of a bilaterally constrained elastic beam; (d) energy diagram illustrating how the released potential energy induces hot-electrons in a floating-gate transistor channel.

The engineering challenge is to achieve an optimal tradeoff between the energy released during buckling (which is related to the material properties of the beam, the end boundary conditions and the lateral constraints) and the energy required for sensing and computation. One possible way to optimize this trade-off is to exploit the physics of mechanical buckling and the physics of piezoelectricity driven impact-ionized hot electron injection. This principle is also illustrated using the energy-band diagram in Figure 5-3 (d) where the piezoelectric transducer converts the released kinetic energy into high-energy electrons (or hot-electrons) in a floating-gate transistor (Huang at al. 2010). If the energy of some of these electrons (with the right momentum vector) exceeds the energy barrier (3.2eV) of the silicon, silicon-di-oxide interface (as shown in

Figure 5-3 (d)), these electrons surmount the barrier and get trapped onto a floating-gate. The concentration of the trapped electrons can be measured to estimate the number of times the magnitude of the input signal exceeded a mechanical threshold (for instance L1 or L2 in Figure 5-3(d)). Huang at al. 2010 showed that the piezoelectricity driven impact ionized hot-electron injection (p-IHEI) process can be initiated at pico-Joule energy density, which is well matched to the energy released during mechanical buckling of a nominally sized elastic beam. The beauty of this physics-based sensing approach is that it completely eliminates the need for voltage regulation, energy storage, analog-to digital converters (ADCs), micro-controller units (MCUs) and random-access memories (RAMs) and hence can be used to push the fundamental limits of self-powered sensing using sub-Hz signals.

## 5.3. Mechanical energy concentrators and triggers

Mode jumping between stable configurations is related to a partial release of the strain energy stored in the compressed beam. The energy drop is converted primarily into kinetic energy allowing the beam to move from one buckled configuration to another more stable configuration under the increasing axial loading. The snap-through response between the equilibrium positions induces an acceleration, which creates an input excitation to an energy harvesting oscillator transducer. Thus, the low-rate strain variations in the axial direction of the beam are transferred into high-rate transverse acceleration that constitutes the input for the transducer element.

The design of the mechanical energy concentrator follows the test setup described in Section 3.2.1. The capability of the system to harvest energy under quasi-static excitations was experimentally investigated. In order to harvest the kinetic energy released during snap-through transitions, A PVDF Piezoelectric energy-harvester was attached at the buckled beam's mid-span

perpendicular to its longitudinal axis (see Figure 3.1) using an off-the-shelf 5 minute epoxy (J-B weld 5 min epoxy). The harvester was configured in a cantilever configuration and only one piezoelectric element was used for the design. However, multiple transducer elements with different properties as well as other piezoelectric materials (PZT, Microfiber Composites, etc.) can be used for enhancing the energy transfer. The snap-through buckling of the axially loaded beam between equilibrium positions induces acceleration at the base of the cantilever, thus transferring the low-rate strains in the buckled beam's axial direction into high-rate accelerations input for the harvester. The post-buckling behavior of the axially loaded bilaterally constrained beam was described in Chapter 3.The properties of the PVDF film are detailed in Table 5-1. The length and tip mass of the oscillator were varied to modify its natural frequency. The polycarbonate beam was subjected to displacement-controlled low-frequency cyclic loading tests. The input frequency was varied to investigate its effect on the levels of the extractable energy. A 10 MΩ - impedance oscilloscope was used to record the output voltage of the piezoelectric harvester.

Table 5-1: Properties of the piezoelectric vibrator.

| Properties (Piezoelectric PVDF / Substrate ) | |
|---|---|
| Elastic Modulus | 2 GPa / 2.4 GPa |
| Density | 1780 kg/m3/ 1390 kg/m3 |
| Thickness | 28 μm / 205 μm |
| Width | 12 mm / 16 mm |
| Piezoelectric Constant (d31) | 23e-12m/V |
| Capacitance | 2.8nF |
| Electrical permittivity | 115 e-12F/m |

Figure 5-4 displays the variation of the axial force in the compressed beam and the output piezoelectric voltage of a full loading/unloading cycle. The first voltage oscillation is caused by the first contact between the beam and the rigid constraints, which correspond to the first buckling mode. The other successive voltage output events are generated by the snap-through of the beam at mode transitions. The high-rate events induce free-vibration in the piezoelectric element. Thus, the output frequency is the natural frequency of the piezoelectric energy harvester controlled by the PVDF film stiffness and the lumped mass. This figure also shows the frequency up-conversion capability of the mechanism where the frequency of the input displacement is 0.05 Hz and the output frequency of the generated voltage is 6.667 Hz.

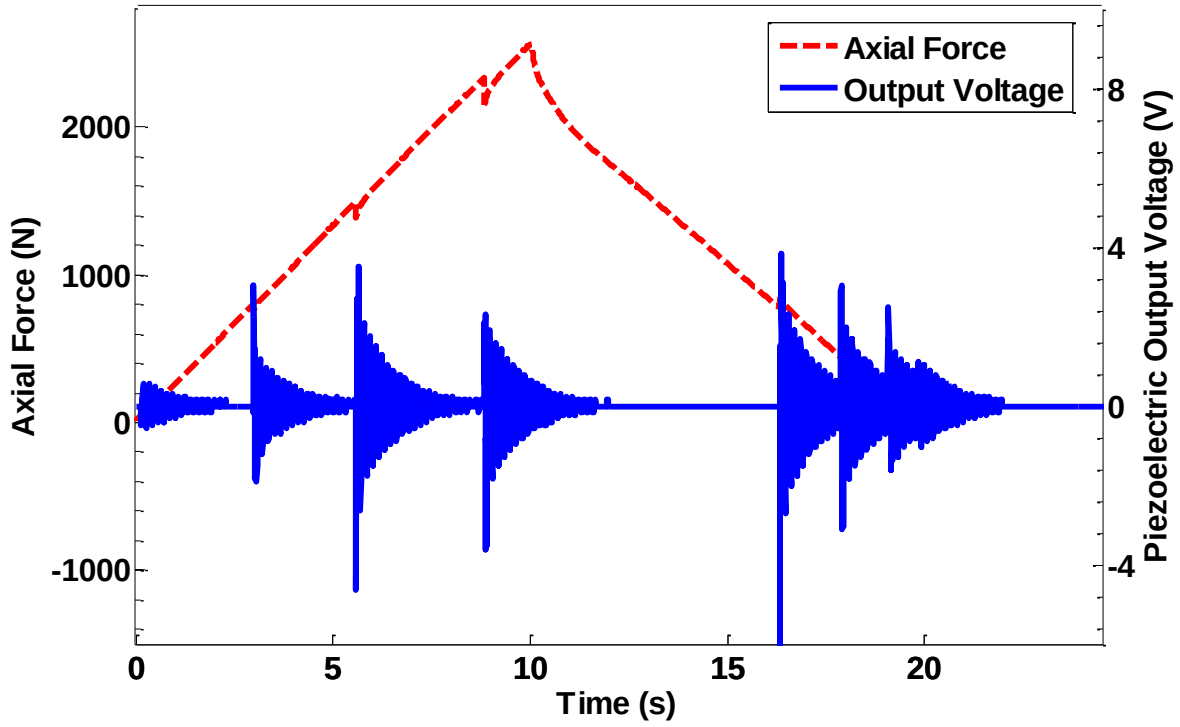


Figure 5-4: Piezoelectric output voltage (output frequency = 6.6667Hz) generated for a full load cycle at 0.05 Hz.

Figure 5-5 shows the computed energy generated by a cantilever piezoelectric PVDF beam measured across a 10 MΩ resistor. The natural frequency of the vibrator was varied from 10 to 90 Hz by modifying the effective length of the PVDF film and the tip mass. The input deformation (axial displacement) rate was varied by increasing the loading/unloading cycle period from 6 s to 150 s, which corresponds to lowering the frequency of the input deformation from 0.16 Hz to 0.006 Hz. The obtained results confirm that energy can be transferred at extremely low-rate deformation input. The input frequency has little influence on the levels of harvested energy. The energy is mainly controlled by the natural frequency and electro-mechanical properties of the scavenger. The levels of harvested energy as well as the output signal frequency can be tuned (optimized) by controlling the piezoelectric element and the constrained beam properties. It should be restated that other piezoelectric materials (PZT, MFC) can be used for enhanced energy transfer.

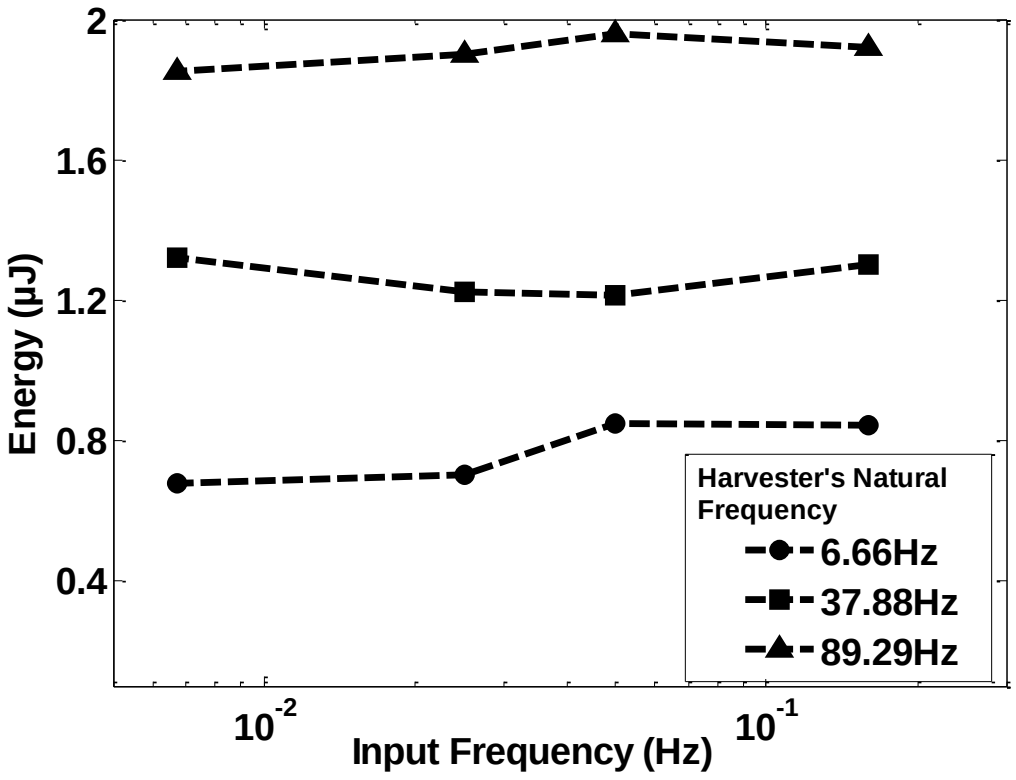


Figure 5-5: Harvested energy for different piezoelectric elements and input loading frequencies.

In a second set of experiments the constrained beam was loaded past its fifth buckling mode (Φ5) and the attained equilibrium position was selected as the initial configuration for this set of tests. Loading cycles were then applied between a maximum load past the seventh mode (Φ7) equilibrium position and a minimum load below the third stable configuration (Φ3). The applied axial load and the voltage output from the PVDF oscillator are shown in Figure 5-6 as function of time. In the figure, the labels Φ3 to Φ7 indicate the positions of snaps or mode transitions. The input axial load was varied at a frequency of 0.11 Hz. At this very slow rate, the voltage response is driven by the natural frequency of the piezoelectric beam (free vibration between transitions), tuned at 6 Hz for this test. This test clearly shows that the system can be initially centered (positioned) so as to harvest energy from compressive as well as from tensile input global loading deformations.

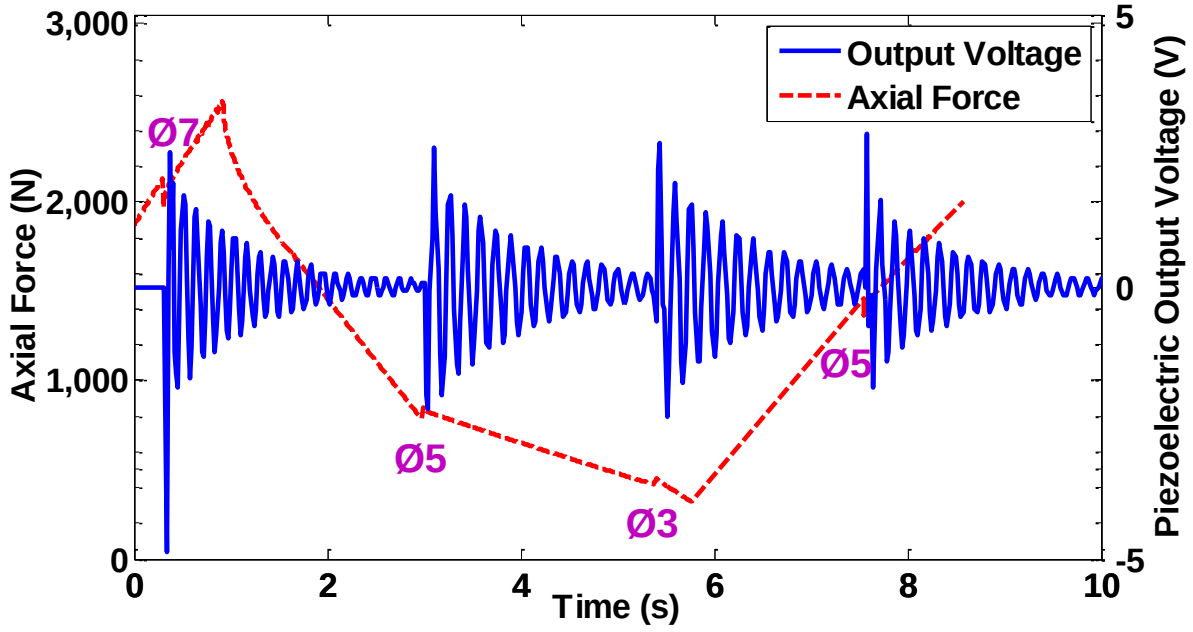


Figure 5-6: Frequency up-conversion principle for alternating loading between the third and the seventh modes at 0.11 Hz. The fifth mode was used as the initial equilibrium position.

## 5.4. Self-powered piezo-floating-gate sensing and data logging

The circuit level schematic and the principle of operation of a linear p-IHEI based data logger is shown in Figure 5-7. The circuit consists of a floating-gate pMOS transistor $M_{fg}$ whose source is driven by a constant current source $I_{ref}$ that is powered by either a piezoelectric transducer or by some other energy source $V_{dda}$. Note that both the energy sources are isolated by a diode, which allows $V_{dda}$ to supersede the signal generated by the piezoelectric transducer. Also note that a full-bridge rectifier (formed by four diodes) is used for extracting energy from the transducer and drive the constant current source $I_{ref}$. The polysilicon gate of the pMOS transistor is electrically insulated by silicon-dioxide (hence the name "floating-gate"); therefore, any electron injected onto the gate is retained for a long period of time (8 bits precision for 8 years) (Diorio et al. 1996). Electrons are injected onto the floating-gate using an impact-ionized hot-electron injection (IHEI) process that involves applying $V_{sd}$ > 4.2V (in 0.5-μm CMOS process) across the source and the drain terminal. The large electric field near the drain of the pMOS transistor creates impact-ionized hot-electrons. When the energy of these electrons exceeds the gate-oxide potential barrier (≈3.2eV) they can get injected onto the floating-gate. IHEI current, $I_{inj}$, in a pMOS transistor is dependent on the transistor source current $I_s$, the source to- drain voltage $V_{sd}$ and the gate-to-drain voltage $V_{gd}$ across the transistor. This dependence can be expressed in functional form as:

$$I_{inj} = f(I_s, V_{sd}, V_{gd}) \tag{5-1}$$

where f (.) is an arbitrary function that could be empirically determined (Huang et al. 2011). However, the circuit in figure. 5-7 (a) achieves stable and ultra-linear injection using a negative feedback loop formed by the opamp A and the floating-gate transistor $M_{fg}$. The source current is held constant at $I_{ref}$, which ensures that the source-to-gate voltage $V_{sg}$ remains constant during injection. When switch SP is open, the feedback is enabled and opamp A ensures that the source-

to-drain voltage $V_{sd}$ is held constant to $V_{ref}$. Thus, according to Equation (5-1) the injection current $I_{inj}$ remains constant. The amount of charge injected onto the floating-gate and hence the decrease in floating-gate voltage $V_{fg}$ is proportional to the duration for which the source current $I_s$ is activated and SP is open. This can be expressed as:

$$\Delta V_{fg} = \frac{1}{C_T}\int_0^T I_{inj}dt = \frac{I_{inj}}{C_T}\tau(T) \tag{5-2}$$

where $\tau$ is the duration of injection and $C_T$ is the total floating-gate capacitance, which includes the capacitance $C_{fg}$, tunneling capacitance and other parasitic capacitances associated with the floating node. The change in floating-gate voltage $\Delta V_{fg}$ could be measured by closing the switch SP, as shown in Figure 5-7 (b), which breaks the feedback loop by shorting the other terminal of $C_{fg}$ to ground. Because the source current $I_{ref}$ is constant, $\Delta V_s = \Delta V_{fg}$ which is read-out through a unity-gain buffer. Figure 5-8 shows the measured response of a linear injector where the source voltage $V_s$ is first initialized to 4.3V (using FN tunneling), $V_{ref}$ = 4.8V and $I_{ref}$ = 30nA. It shows that the response follows the linear model almost throughout the range. The piezoelectric transducer is emulated by applying a 50ms long pulse signal (amplitude $V_{dd}$ =6.5V) after which the switch SP is turned ON and the source voltage $V_s$ is measured. Figure 5-8 shows that the change in $V_s$ is linear with respect to the number of applied pulses. The deviation from the linear injection model occurs at the end points of the operating voltage and is due to the finite operating range of the amplifier A. This shows that the linear injector has a linear range of almost 4V. The resolution of the linear injector was measured to be greater than 13 bits (Huang et al. 2011).

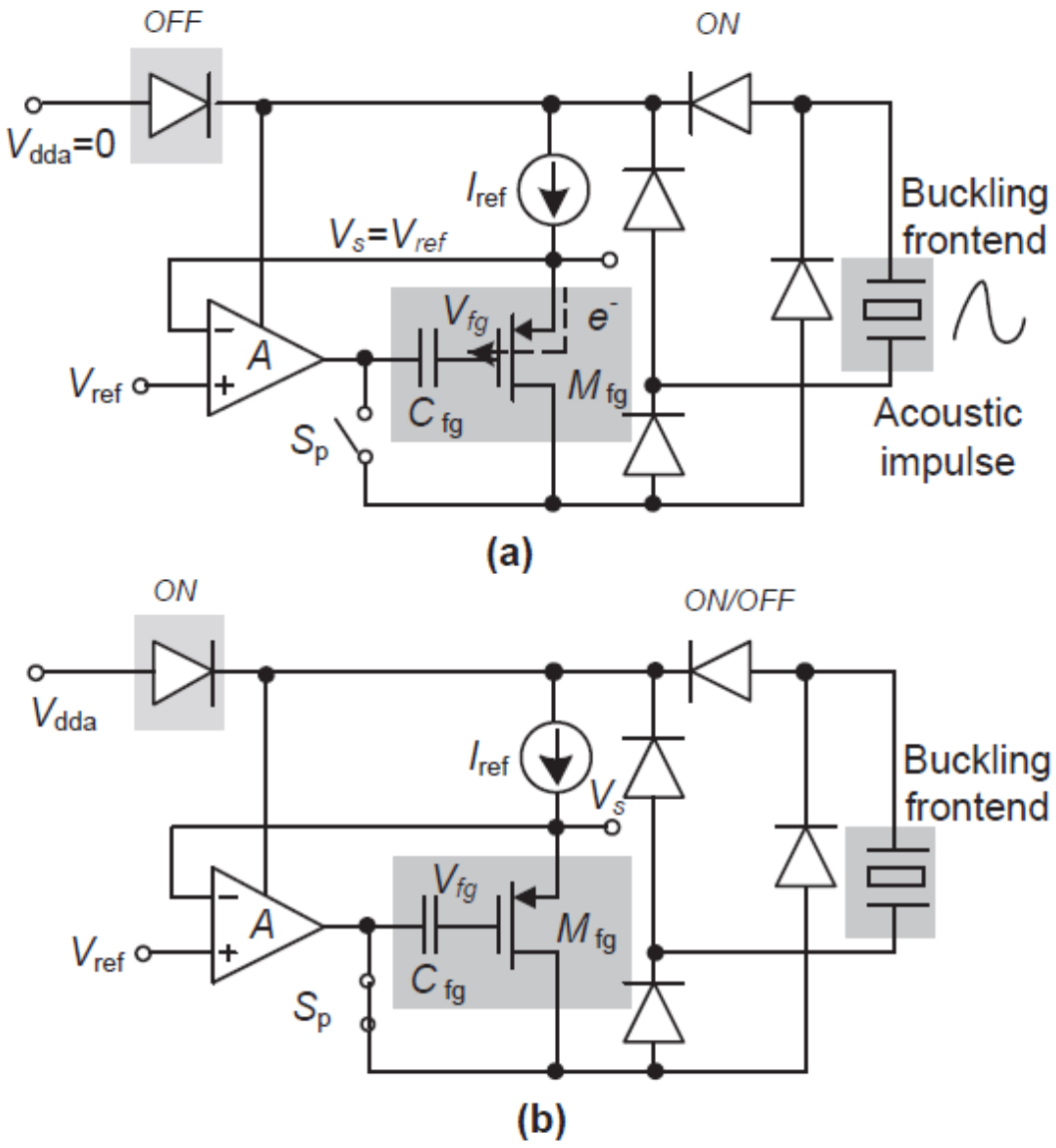


Figure 5-7: Schematic of a linear p-IHEI based data logging circuit: (a) when operating in the data logging mode; and (b) when operating in a data read-out mode (Lajnef et al. 2014b).

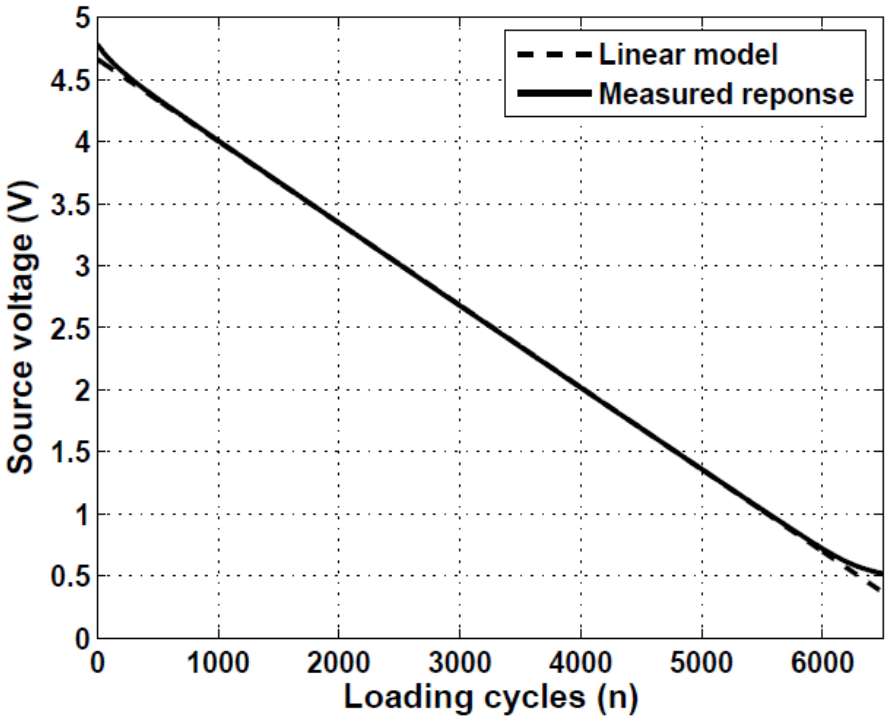


Figure 5-8: Measured output range and the linearity for linear injection circuit (Sarkar et al. 2013).

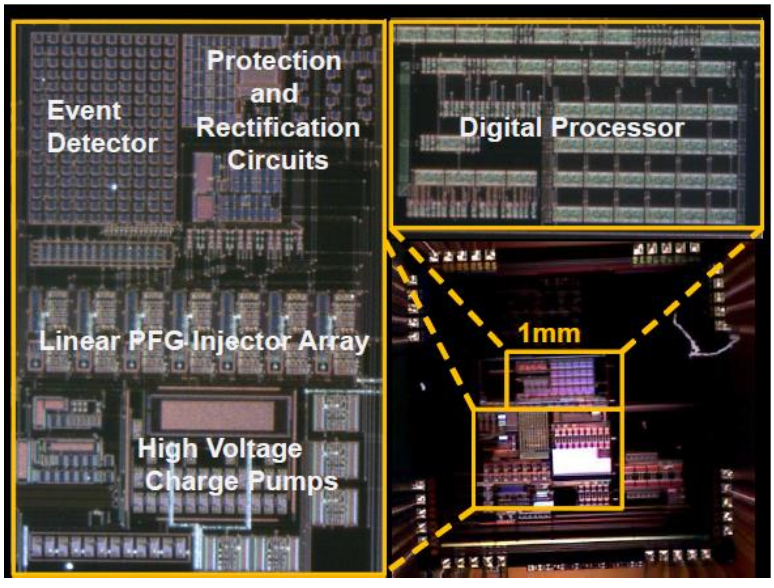


Figure 5-9: Micrograph of a fabricated prototype integrating an array of linear floating-gate injectors along with digital command-control and programming circuits (Lajnef et al., 2014b).

Figure 5-9 shows the micrograph of a p-IHEI based data logging circuit which was fabricated in a 0.5 μm CMOS process. The prototype integrates an array of linear floating-gate injectors that can be programmed using on-chip high-voltage charge pumps. Programming, selection and read-out of the injectors can be controlled using digital command and control, which is implemented on-chip by an integrated digital processing module.

Two sets of experiments were conducted to validate the behavior of the described quasi-static sensing functionalities. In the first runs, the system was cycled between only two equilibrium positions (loading then unloading). The actuator, which applied the external force, was moved at a frequency of 0.1 Hz and then 0.5 Hz while the induced oscillations at the PVDF beam were measured at 12.82 Hz. Figure 5-10 shows the applied input deformation (for a 0.1 Hz loading) and the rectified voltage output generated by the vibrating piezoelectric element. It is noted from the levels of generated voltage that the released energy is higher during loading when the applied force (added potential) is being increased. The combined piezoelectric-floating-gate event counting device was calibrated to detect and record voltages higher than 4V. The impact ionized hot-electron injection process at the floating gate memory cell is activated only when the voltage exceeds the preset threshold. For each event the gate is thus active for about 0.2 seconds. The voltage variations at the floating gate was measured periodically and is shown in figures 5-11 and 5-12. The results in Figure 5-11 were recorded for cyclic input loading events applied at 0.1 Hz while the measurements in Figure 5-12 were obtained for an input loading applied at 0.5 Hz. It is observed that the system clearly implements a linear injector allowing to directly relate the number of applied events to the measured voltage variation at the floating gate output.

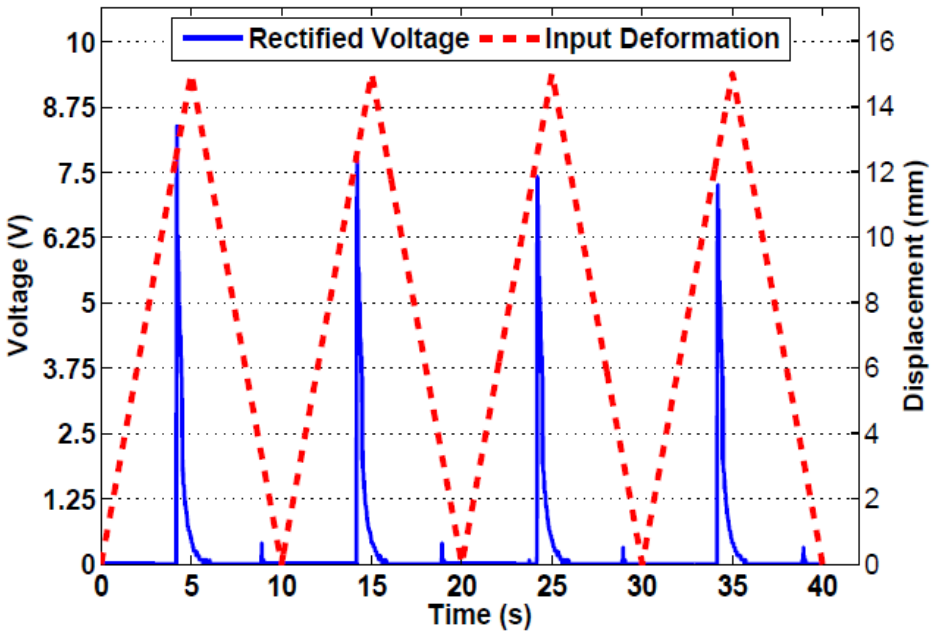


Figure 5-10: Measured output piezoelectric voltage generated for loading cycles at 0.1 Hz, showing the system's ability for energy generation under quasi-static loading.

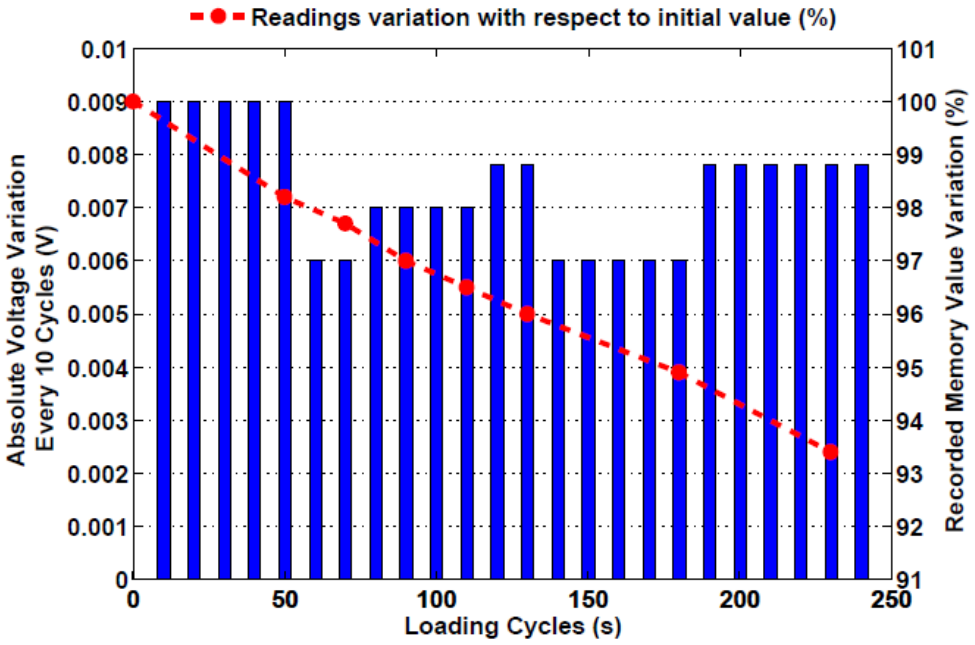


Figure 5-11: Recorded variations of the voltage at the analog floating gate for input cyclic loading events at 0.1Hz.

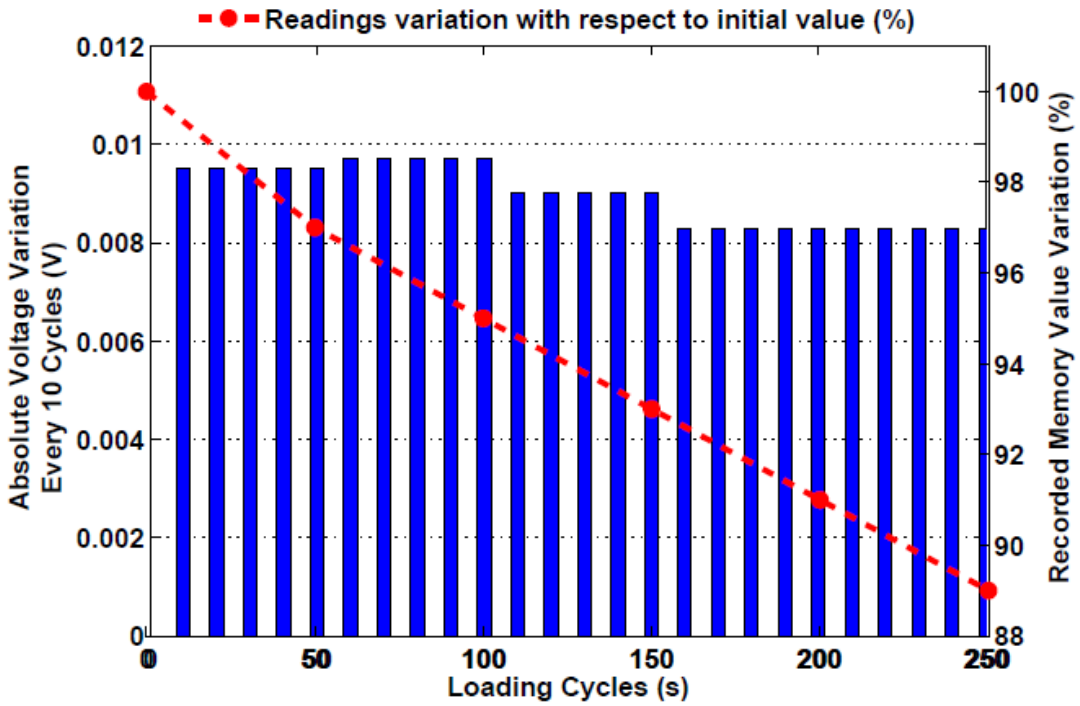


Figure 5-12: Recorded variations of the voltage at the analog floating gate for input cyclic loading events at 0.5 Hz.

In the next set of experiments the restrained beam was initially loaded past its fifth buckling mode which was selected as the starting configuration. Loading cycles were then applied between a maximum load past the seventh mode equilibrium position and a minimum load below the third stable configuration. The mode shapes are shown in Figure 3-2. The applied axial load, axial deformation, and the rectified voltage output from the PVDF transducer are shown in Figure 5-13 as function of time. The input load varies at a frequency of about 0.1 Hz. At this rate the voltage response is driven by the natural frequency of the piezoelectric harvester. For this case the PVDF beam was tuned to 6 Hz. The combined piezoelectric-floating- gate event counting device was again calibrated to detect and record voltages higher than 4 V. For these specific experimental runs, the preset threshold is exceeded only during the snap-buckling from the third to the fifth

mode as clearly shown in Figure 5-13. This translates into a calibrated system that records only these transitions. The difference in voltage output between transitions is due to the levels of stored strain energy in the system before the transition events and can be tuned and calibrated as shown experimentally in Chapter 3. Figure 5-14 shows the recorded voltage variations at the linear injector. The sensor clearly implements a linear recording of events allowing direct correspondence between the number of applied events and the measured sensor output voltage.

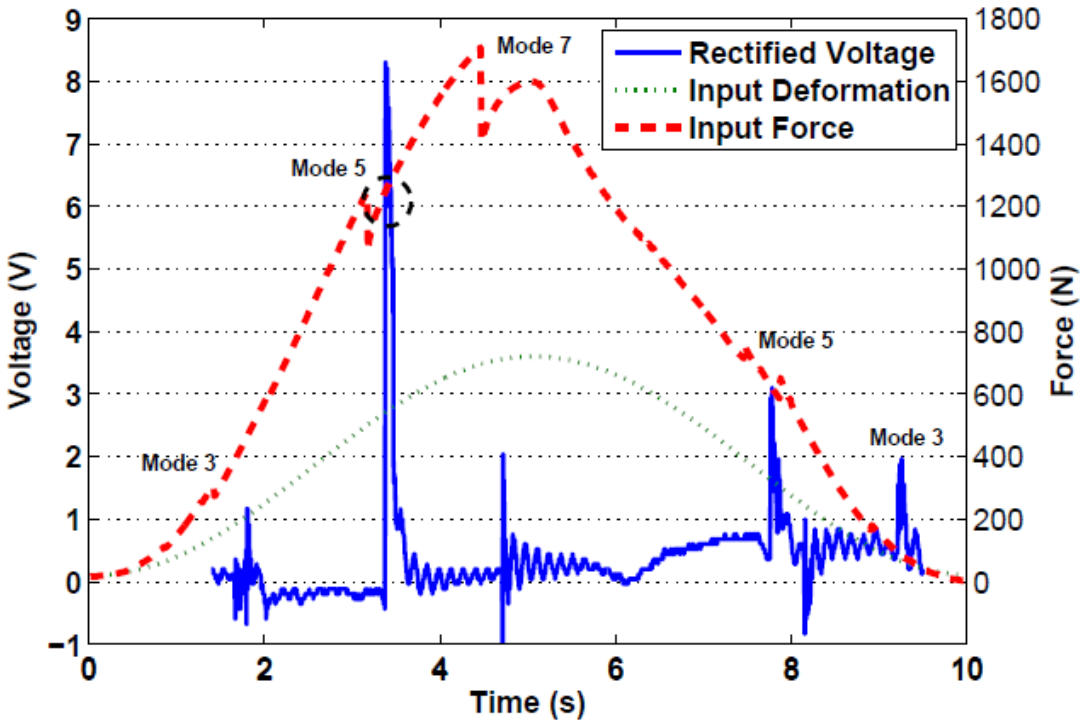


Figure 5-13: Illustration of the energy conversion principle under cyclic loading at 0.1 Hz for the bilaterally constrained beam configuration.

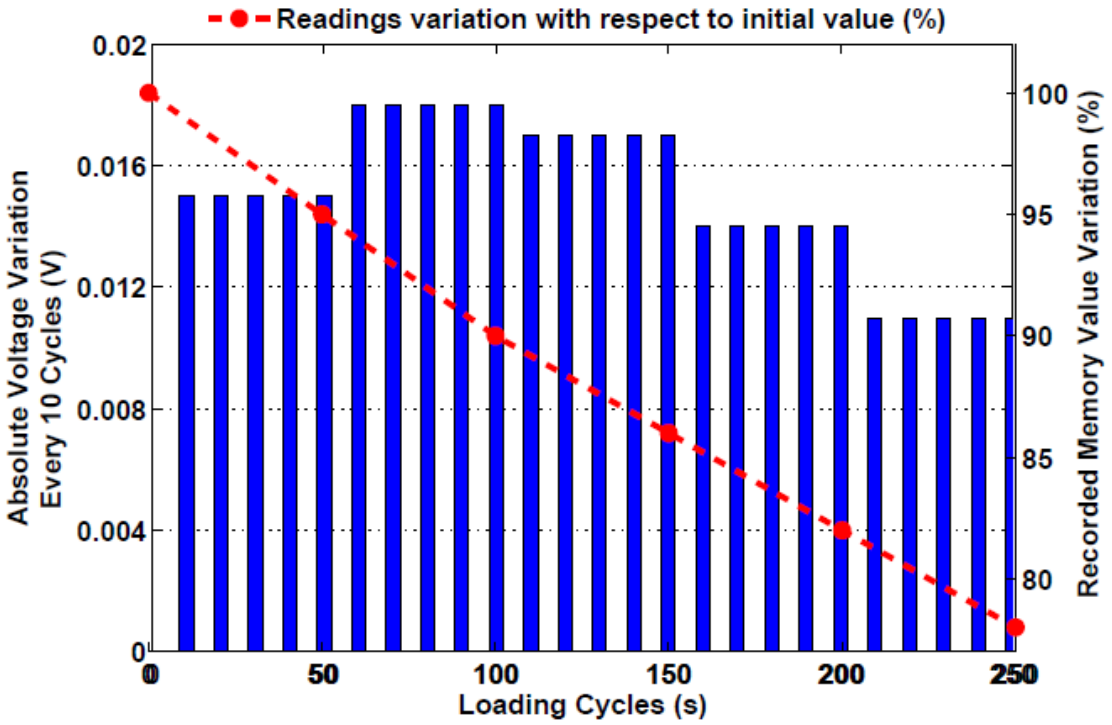


Figure 5-14: Recorded variations of the voltage at the analog floating gate for input cyclic loading events at 0.1 Hz.

## 5.5. Summary

This chapter presented a novel self-powered sensing mechanism that combines the physics of mechanical buckling in bilaterally constrained elastic beams with the physics of piezoelectricity driven hot-electron injection. During the snap-through events, part of the stored strain energy is released as kinetic energy. The piezoelectric transducer that is attached to the buckling element converts the released kinetic energy into high-energy electrons in a floating-gate transistor. The concentration of the trapped electrons can be measured to determine the number of times the magnitude of the input signal exceeded a mechanical threshold.

Integrating mechanical energy concentrators and triggers with the piezo-floating gate sensor allows for harvesting the released energy as bursts and impulses. The impulsive nature of

the energy-release not only results in piezoelectric output voltage levels that are significantly higher than the triggering but also reduces the effect of energy leakage.

The piezo-floating-gate data logging is used as a counting device. The impact ionized hot-electron injection process at the floating gate memory cell is activated only when the voltage exceeds the preset threshold. The levels of the generated voltage differ from one mode transition to another. Therefore the system can be calibrated to record some specific events. The system implements a linear injector allowing to directly relate the number of applied events to the measured voltage variation at the floating gate output.

As shown in Chapter 3, the input frequency has little influence on the occurrence of the snap-buckling events. Therefore, the generation and levels of energy bursts are independent of the input frequency. Results confirm that the energy can be transferred at extremely low-rate deformation input. Moreover, the mechanism allows for frequency up-conversion from the low input frequency (in the order of mHz) to the natural frequency of the piezoelectric scavenger determined by its stiffness and the attached tip mass.

As a result, the proposed sensor was demonstrated to self-power at mHz frequencies and with the potential to scale down to μHz frequencies, a feature that is not possible with other self-powered sensing approaches.

# CHAPTER 6: CONCLUSIONS

## 6.1. Research contributions

### *6.1.1. Post-buckling response of bilaterally constrained beams using an energy method*

The models developed based on geometric assumptions and geometric elliptic integrations are able to capture the system stiffness. However, they fail to accurately predict the levels of forces and displacement at which transitions occur, especially as the number of buckled waves increases. The developed static model, which is based on the minimization of the potential energy, is able to adequately predict the mode transition events as well as the beam geometry at every loading stage, including the flattening behavior just before the snap buckling transitions.

### *6.1.2. Dynamic response and transitions in multiple bifurcation points mechanical energy concentrators*

This research presented a study of the mechanical energy concentrators' dynamic response under cyclic axial loading. The analysis was based on the minimization of the total energy under the prescribed boundary conditions and constraints. The developed model assesses the dynamic force-displacement response of the system as well as the released kinetic energy and generated transverse accelerations at buckling mode transitions.

### *6.1.3. Energy transfer at quasi-static excitations using mechanical energy concentrators*

This research presented a technique to harvest energy at very low frequencies (less than 1 Hz) using the snap-through behavior between the multiple equilibrium positions of axially-loaded bilaterally-constrained beams. The approach relies on the high-rate motions that are generated

during the transitions between the system's multiple potential energy wells. The input is not a vibration motion but a slow quasi-static deformation. Unlike the developed vibration-based energy harvesters, the proposed mechanism converts the slow-rate input strain into high-rate accelerations generated at buckling mode transitions. During these transitions part of the stored potential energy is released as kinetic energy. The role of the piezoelectric energy harvester is to convert the released kinetic energy into voltage that can be stored or used for computation and sensing.

#### *6.1.4. Self-powered sensing at micro Hertz*

This research introduced a novel technique for self-powered sensing at very low frequencies by integrating mechanical energy concentrators and triggers with piezo-floating gate sensors. Piezo-floating-gate data logging is used as a counting device that records the number of times the magnitude of the input signal exceeded a mechanical threshold. Since the post-buckling response of bilaterally constrained beams is independent of the input frequency, the same levels of energy bursts are always generated regardless the input frequency. Therefore the proposed sensor is able to self-power at μHz frequencies, a feature that is not possible with other self-powered sensing approaches.

## 6.2. Conducted work

The post-buckling response of an axially loaded bilaterally constrained beam was investigated experimentally, numerically and theoretically. It was shown that due to lateral rigid walls, the elastica is able to undergo higher buckling modes as the axial load increases. Under variable axial loading the beam transitions between the different equilibrium states of the system. The transitions between the buckling modes always occur at the same axial force and displacement levels. Furthermore the behavior is independent of the excitation frequency. However, the response

of the system is highly dependent of its parameters such as thickness and length of the beam, modulus of elasticity, gap between the rigid walls, position of the beam and boundary conditions. These parameters affect the axial displacements and forces at which transitions occur and the accelerations generated during buckling mode switching. The effect of these parameters was numerically investigated using an FE model. It was shown that placing the beam adjacent to one of the lateral walls with fixed-end supports generates higher accelerations. Furthermore the accelerations amplify by increasing the thickness, Young's modulus or gap between the walls, or by decreasing the beam length. However, the combination between the length and one of the other parameters may have the opposite effect. Therefore to reduce the beam length, the thickness, Young's modulus and gap should be upper-bounded in order to allow the development of higher modes and hence the generation of high accelerations.

Although tuning the parameters of the system affects dramatically the accelerations generated in snap-through transitions, the number and the spacing between these events was shown to be non-sensitive to the studied parameters. In order to control the number and the spacing between the mode transitions, multiple slender beams were stacked into a system in a parallel configuration. It was shown that any modification of the beams' thicknesses, Young's moduli and gaps between the walls affects the locations of the transitions and the overall stiffness of the system. More important is that the number and the spacing between these events can be controlled by tuning the aforementioned parameters without sacrificing the levels of the accelerations.

A theoretical model using energy methods was developed to investigate the post-buckling response of a bilaterally constrained beam subjected to axial force or displacement. The model accounts for longitudinal deformations and friction. The total energy was minimized under the confinement constraint in order to determine the deflected shape, transitions states and energy

balance at transitions. The static response of the beam was investigated using force- and displacement-control formulations. Results show that the model is able to adequately predict the beam geometry at every loading stage, including the flattening behavior just before the snap buckling transitions, and simultaneously determines the mode transition events.

The released kinetic energy as well as accelerations of the beam during transitions were studied using a dynamic analysis. It was shown that the beam returns to lower buckling configurations through a different equilibrium path. Moreover, the buckling transitions generate high kinetic energy and acceleration spikes. However, the location of the maximum acceleration differs from one transition to another. Hence, placement of the piezoelectric energy harvester should be carefully chosen depending on the application.

During the snap-through events, part of the stored strain energy is released as kinetic energy. The piezoelectric transducer that is attached to the buckling element converts the released kinetic energy into high-energy electrons in a floating-gate transistor. Integrating mechanical energy concentrators and triggers with the piezo-floating gate sensor allows for harvesting the released energy as bursts and impulses. The impulsive nature of the energy-release not only results in piezoelectric output voltage levels that are significantly higher than the triggering but also reduces the effect of energy leakage.

The piezo-floating-gate data logging was used as a counting device. The impact ionized hot-electron injection process at the floating gate memory cell is activated only when the voltage exceeds the preset threshold. The levels of the generated voltage differ from one mode transition to another. Therefore the system can be calibrated to record specific events. The concentration of the trapped electrons can be measured to determine the number of times the magnitude of the input signal exceeded a mechanical threshold. Energy can be transferred at extremely low-rate

deformation input. The generation and levels of energy bursts are independent of the input frequency. The mechanism allows for frequency up-conversion from the low input frequency (in the order of mHz and μHz) to the natural frequency of the piezoelectric scavenger determined by its stiffness and the attached tip mass.

## 6.3. Future research

### *6.3.1. Optimization of the piezoelectric energy scavenger*

The levels of the harvestable energy are independent of the input frequency. However, they highly depend on the natural frequency and electro-mechanical properties of the scavenger. The piezoelectric energy scavenger used in the experiments was made of polymer polyvinylidene fluoride (PVDF) for its low cost and ease to install. However, PVDF materials have low mechanical-to-electrical conversion coefficients. Other piezoelectric materials such as Lead Zirconate Titanate (PZT) and Microfiber Composites can be used to enhance the energy transfer. Dimensions of the piezoelectric energy scavenger and the attached lumped mass should be optimized in order to maximize the energy harvested during snap-through events.

### *6.3.2. Optimization of mechanism's parameters for different strain ranges*

The parametric analysis performed in this work provides confidence that the mechanism can be scalable for embedment within structures. Strains present the input to the mechanical energy concentrators and triggers. Therefore, dimensions and material properties of the bilaterally constrained beam as well as the gap between the lateral rigid walls should be tuned such that transitions occur under the applied level of strain. A design manual or chart can be developed to determine the optimized values of the parameters for different strain ranges. It would be of interest if the mechanism is installed in a pre-compressed configuration such that it transitions between a

higher and lower buckling mode as the global input strain alternates between compression and traction.

### *6.3.3. Optimization of the algorithm to include friction effects*

The theoretical results shown in this work do not include the effect of friction on the post-buckling dynamic response of the bilaterally constrained beam. It would be of interest to investigate the effect of friction on the post-buckling behavior as well as the levels of the released energy and generated accelerations. Even though the formulation of the energy dissipated due to friction was presented in section 4.4.3, the computation was very costly due to the coupling between numerical constrained minimization and numerical integration. A simplification or approximation of the dissipated energy would alleviate the minimization problem resolution.

# APPENDIX

Table A-1: Cases in parametric studies. Case 1 corresponds to the experimentally evaluated system. Parameter values in bold text indicate changes from the values in Case 1.

| | *BC 1* | *BC 2* | *E* | *L* | *t* | $h_0$ | *Beam Position* |
|---|---|---|---|---|---|---|---|
| | = 0 free; =1 fixed | = 0 free; =1 fixed | (MPa) | (mm) | (mm) | (mm) | Side/Center |
| **Reference case 1** | 1 | 1 | 2250 | 250 | 2.34 | 4 | Side |
| Case 2 | **0.75** | 1 | 2250 | 250 | 2.34 | 4 | Side |
| Case 3 | **0.5** | 1 | 2250 | 250 | 2.34 | 4 | Side |
| Case 4 | **0** | 1 | 2250 | 250 | 2.34 | 4 | Side |
| Case 5 | 1 | **0.75** | 2250 | 250 | 2.34 | 4 | Side |
| Case 6 | 1 | **0.5** | 2250 | 250 | 2.34 | 4 | Side |
| Case 7 | 1 | **0** | 2250 | 250 | 2.34 | 4 | Side |
| Case 8 | **0.5** | **0.5** | 2250 | 250 | 2.34 | 4 | Side |
| Case 9 | **0** | **0** | 2250 | 250 | 2.34 | 4 | Side |
| Case 10 | 1 | 1 | **3375** | 250 | 2.34 | 4 | Side |
| Case 11 | 1 | 1 | **4500** | 250 | 2.34 | 4 | Side |
| Case 12 | 1 | 1 | **6750** | 250 | 2.34 | 4 | Side |
| Case 13 | 1 | 1 | 2250 | **212.5** | 2.34 | 4 | Side |
| Case 14 | 1 | 1 | 2250 | **187.5** | 2.34 | 4 | Side |
| Case 15 | 1 | 1 | 2250 | **125** | 2.34 | 4 | Side |
| Case 16 | 1 | 1 | 2250 | **76.2** | 2.34 | 4 | Side |

Table A-1 (cont'd)

| | | | | | | | |
|---|---|---|---|---|---|---|---|
| Case 17 | 1 | 1 | 2250 | 250 | **1.56** | 4 | Side |
| Case 18 | 1 | 1 | 2250 | 250 | **1.17** | 4 | Side |
| Case 19 | 1 | 1 | 2250 | 250 | **0.78** | 4 | Side |
| Case 20 | 1 | 1 | 2250 | 250 | 2.34 | **4.83** | Side |
| Case 21 | 1 | 1 | 2250 | 250 | 2.34 | **5.66** | Side |
| Case 22 | 1 | 1 | 2250 | 250 | 2.34 | **7.32** | Side |
| Case 23 | 1 | 1 | 2250 | 250 | 2.34 | 4 | Center |
| Case 24 | 1 | 1 | **3375** | 250 | 2.34 | 4 | Center |
| Case 25 | 1 | 1 | **4500** | 250 | 2.34 | 4 | Center |
| Case 26 | 1 | 1 | **6750** | 250 | 2.34 | 4 | Center |
| Case 27 | 1 | 1 | 2250 | **212.5** | 2.34 | 4 | Center |
| Case 28 | 1 | 1 | 2250 | **187.5** | 2.34 | 4 | Center |
| Case 29 | 1 | 1 | 2250 | **125** | 2.34 | 4 | Center |
| Case 30 | 1 | 1 | 2250 | 250 | **1.56** | 4 | Center |
| Case 31 | 1 | 1 | 2250 | 250 | **1.17** | 4 | Center |
| Case 32 | 1 | 1 | 2250 | 250 | **0.78** | 4 | Center |
| case 33 | 1 | 1 | 2250 | 250 | 2.34 | **4.83** | Center |
| Case 34 | 1 | 1 | 2250 | 250 | 2.34 | **5.66** | Center |
| Case 35 | 1 | 1 | 2250 | 250 | 2.34 | **7.32** | Center |
| Length and thickness variation | | | | | | | |
| Case 36 | 1 | 1 | 2250 | **212.5** | **1.56** | 4 | Side |

Table A-1 (cont'd)

| | | | | | | | |
|---|---|---|---|---|---|---|---|
| Case 37 | 1 | 1 | 2250 | **212.5** | **1.17** | 4 | Side |
| Case 38 | 1 | 1 | 2250 | **212.5** | **0.78** | 4 | Side |
| Case 39 | 1 | 1 | 2250 | **187.5** | **1.56** | 4 | Side |
| Case 40 | 1 | 1 | 2250 | **187.5** | **1.17** | 4 | Side |
| Case 41 | 1 | 1 | 2250 | **187.5** | **0.78** | 4 | Side |
| Case 42 | 1 | 1 | 2250 | **125** | **1.56** | 4 | Side |
| Case 43 | 1 | 1 | 2250 | **125** | **1.17** | 4 | Side |
| Case 44 | 1 | 1 | 2250 | **125** | **0.78** | 4 | Side |
| Case 45 | 1 | 1 | 2250 | **76.2** | **1.56** | 4 | Side |
| Case 46 | 1 | 1 | 2250 | **76.2** | **1.17** | 4 | Side |
| Case 47 | 1 | 1 | 2250 | **76.2** | **0.78** | 4 | Side |
| Length and gap variation | | | | | | | |
| Case 48 | 1 | 1 | 2250 | **212.5** | 2.34 | **4.83** | Side |
| Case 49 | 1 | 1 | 2250 | **212.5** | 2.34 | **5.66** | Side |
| Case 50 | 1 | 1 | 2250 | **212.5** | 2.34 | **7.32** | Side |
| Case 51 | 1 | 1 | 2250 | **187.5** | 2.34 | **4.83** | Side |
| Case 52 | 1 | 1 | 2250 | **187.5** | 2.34 | **5.66** | Side |
| Case 53 | 1 | 1 | 2250 | **187.5** | 2.34 | **7.32** | Side |
| Case 54 | 1 | 1 | 2250 | **125** | 2.34 | **4.83** | Side |
| Case 55 | 1 | 1 | 2250 | **125** | 2.34 | **5.66** | Side |
| Case 56 | 1 | 1 | 2250 | **125** | 2.34 | **7.32** | Side |

Table A-1 (cont'd)

| | | | | | | | |
|---|---|---|---|---|---|---|---|
| Case 57 | 1 | 1 | 2250 | **76.2** | 2.34 | **4.83** | Side |
| Case 58 | 1 | 1 | 2250 | **76.2** | 2.34 | **5.66** | Side |
| Case 59 | 1 | 1 | 2250 | **76.2** | 2.34 | **7.32** | Side |
| Length and Young's modulus variation | | | | | | | |
| Case 60 | 1 | 1 | **3375** | **212.5** | 2.34 | 4 | Side |
| Case 61 | 1 | 1 | **4500** | **212.5** | 2.34 | 4 | Side |
| Case 62 | 1 | 1 | **6750** | **212.5** | 2.34 | 4 | Side |
| Case 63 | 1 | 1 | **3375** | **187.5** | 2.34 | 4 | Side |
| Case 64 | 1 | 1 | **4500** | **187.5** | 2.34 | 4 | Side |
| Case 65 | 1 | 1 | **6750** | **187.5** | 2.34 | 4 | Side |
| Case 66 | 1 | 1 | **3375** | **125** | 2.34 | 4 | Side |
| Case 67 | 1 | 1 | **4500** | **125** | 2.34 | 4 | Side |
| Case 68 | 1 | 1 | **6750** | **125** | 2.34 | 4 | Side |
| Case 69 | 1 | 1 | **3375** | **76.2** | 2.34 | 4 | Side |
| Case 70 | 1 | 1 | **4500** | **76.2** | 2.34 | 4 | Side |
| Case 71 | 1 | 1 | **6750** | **76.2** | 2.34 | 4 | Side |

# REFERENCES

## REFERENCES


Barton, D.W., Burrow, S.G. and Clare, L.R., 2010. Energy harvesting from vibrations with a nonlinear oscillator. Journal of vibration and acoustics. 132021009-021009-7.

Blystad, L-C.J. and Halvorsen, E., 2011. An energy harvester driven by colored noise. Smart Materials and Structures 20 025011.

Borchani, W., Lajnef, N. and Burgueño R., 2013. Control of Snap-through Transitions in the Response of Mechanically-equivalent Frequency Modulators. ASME Conference on Smart Materials, Adaptive Structures and Intelligent Systems, Snowbird, UT, September 2013.

Borchani, W., Lajnef, N. and Burgueño R., 2014a. Dynamic Transitions in Multiple Bifurcation Points Mechanical Energy Concentrators. 17th U.S. National Congress on Theoretical and Applied Mechanics, Michigan State University, June 2014.

Borchani, W., Lajnef, N. and Burgueño R., 2014b. Model development for Dynamic Energy Conversion in post-buckled multi-stable slender columns. ASME Conference on Smart Materials, Adaptive Structures and Intelligent Systems, Newport, Rhode Island, September 2014.

Burgess, I.W., 1971. The buckling of a radially constrained imperfect circular ring. International Journal of Mechanical Sciences. 13,741–753.

Burgueño, R., Lajnef, N., 2013. Energy harvesting devices for low frequency. Application. U.S. Patent Application, Serial No. 13/960,356, United States

Cazottes, P., Fernandes, A., Hafez, M. and Pouget, J., 2009. Bistable buckled beam: modeling of actuating force and experimental validations. Journal of Mechanical Design 131 101001.

Chai, H., 1998. The post-buckling response of a bi-laterally constrained column. Journal of the Mechanics and Physics of Solids 46 1155-1181.

Chateau, X. and Nguyen, Q.S., 1991. Buckling of elastic structures in unilateral contact with or without friction. European Journal of Mechanics-A/Solids 10 71-89.

Daqaq, M.F., 2010. Response of uni-modal duffing-type harvesters to random forced excitations Journal of Sound and Vibration 329 3621-3631.

Diorio, C., Hasler, P., Minch, B. and Mead, C.A., 1996. A single-transistor silicon synapse, IEEE Trans. Electron Devices 43 1972-1980.

Domokos, G., Holmes, R. and Royce, B., 1997. Constrained Euler buckling. Journal of Nonlinear Science 7 281-314.

Elfrink, R., Kamel, T.M., Goedbloed, M., Matova, S., Hohlfeld, D., Van Andel, Y. and Van Schaijk, R., 2008. Vibration energy harvesting with aluminum nitride-based piezoelectric devices. International Workshop on Micro and Nanotechnology for Power Generation and Energy Conversion Applications – PowerMEMS, Sendai, Japan, pp 249-252

Elvin, N.G., Lajnef, N. and Elvin, A.A., 2006. Feasibility of structural monitoring with vibration powered sensors. Smart Materials and Structures 15 977-986.

Erturk, A., Hoffmann, J .and Inman, D.J., 2009. A piezomagnetoelastic structure for broadband vibration energy harvesting. Applied Physics Letters 94 254102.

Erturk, A., Renno, J.M. and Inman, D.J., 2009. Modeling of piezoelectric energy harvesting from an L-shaped beam-mass structure with an application to UAVs. Journal of Intelligent Material Systems and Structures 20 529–544.

Essenburg, F., 1975. On the significance of the inclusion of the effect of transverse normal strain in problems involving beams with surface constraints. Journal of Applied Mechanics 42 127-132.

Fang, W. and Wickert, J.A., 1994. Post buckling of micromachined beams, Journal of Micromechanics and Microengineering. 4, 116-122.

Finkel, P., Lofland, S.E. and Garrity, E., 2009. Magnetoelastic/piezoelectric laminated structures for tunable remote contactless magnetic sensing and energy harvesting. Applied Physics Letters 94 07250.

Galchev, T., Kim, H. and Najafi, K., 2011. Micro power generator for harvesting low-frequency and nonperiodic vibrations. Journal of Microelectromechanical Systems 20 852–66.

Green, P.L., Papatheou, E. and Sims, N.D., 2013. Energy harvesting from human motion and bridge vibrations: An evaluation of current nonlinear energy harvesting solutions. Journal of Intelligent Material Systems and Structure 24 1494-1505.

Holmes, P., Domokos, G., Schmitt, J. and Szeberényi, I., 1999. Constrained Euler buckling: an interplay of computation and analysis. Computer Methods in Applied Mechanics and Engineering 170 175–207.

Huang, C., Lajnef, N., Chakrabartty, S., 2010. Self-calibration and characterization of self-powered floating-gate usage monitors with single electron per second operational limit. IEEE Transactions of Circuits and Systems-I, 57 556-567.

Huang C., Sarkar P., and Chakrabartty S., 2011. “Rail-to-rail hot-electron injection programming of floating-gate voltage bias generators at a resolution of 13bits”, IEEE Journal of Solid-State Circuits 46 2685-2692.

Hutchinson, J.W. and Koiter, W.T., 1970. Postbuckling theory. Applied Mechanics Reviews .23, 1353-1366.

Jung, S.M. and Yun, K.S., 2010. Energy-harvesting device with mechanical frequency-up conversion mechanism for increased power efficiency and wideband operation. Appl. Phys. Lett. 96 111906.

Lajnef, N., Burgueño, R., Borchani, W., Sun, Y. and Heeringa, A., 2012. Characterization of mechanically-equivalent amplifiers and frequency modulating concepts for energy harvesting devices. Proc. Conference on Smart Materials, Adaptive Structures and Intelligent Systems, Atlanta, GA, September 2012.

Lajnef, N., Burgueño, R., Chakrabartty, S. and Borchani, W., 2013. Self-powered Sensing System for the Monitoring of Quasi-static Structural Response. ASME Conference on Smart Materials, Adaptive Structures and Intelligent Systems, Snowbird, UT, September 2013.

Lajnef, N., Burgueño, R., Borchani, W. and Sun, Y., 2014a. A concept for energy harvesting from quasi-static structural deformations through axially loaded bilaterally constrained columns with multiple bifurcation points. Smart Mater. Struct. 23 055005.

Lajnef, N., Borchani, W., Burgueño, R., Chakrabartty, S., 2014b. Self-powered piezo-floating-gate smart-gauges based on quasi-static mechanical energy concentrators and triggers, IEEE Sensors Journal DOI: 10.1109/JSEN.2014.2351398.

Lajnef, N., Chakrabartty, S., Burgueño, R. and Borchani, W. 2014c. Quasi-static self-powered sensing and data logging, in Proc. SPIE Sensors and Smart Structures Technologies for Civil, Mechanical, and Aerospace Systems, San Diego, USA, March 2014

Lajnef, N., Burgueño, R., Borchani, W. and Chakrabartty, S., 2014d. Sub-Hz Self-Powered Sensing Based on Mechanical-Buckling Driven Hot-Electron Injection. International Symposium on Circuits and Systems, Melbourne, Australia, June 2014.

Lajnef, N., Borchani, W., Burgueño, R. and Chakrabartty, S., 2014e. Energy Concentrators for Piezo-powered Quasi-static Data Logging. Proceedings of the 6th World Conference on Structural Control and Monitoring (6WCSCM), Barcelona, Spain, July 2014.

Liu, J.Q., Fang, H.B., Xu, Z.Y., Mao, X.H., Shen, X.C., Chen, D., Liao, H. and Cai, B.C., 2008. A MEMS-based piezoelectric power generator array for vibration energy harvesting. Microelectronics Journal 39 802–806.

Mann, B., Sims, N., 2009. Energy harvesting from the nonlinear oscillations of magnetic levitation. Journal of Sound and Vibrations 319 515–530.

Masana, R. and Daqaq, M.F., 2011. Electromechanical modeling and nonlinear analysis of axially loaded energy harvesters. Journal of Vibration and Acoustics 133 011007-1.

Moss, S., Barry, A., Powlesland, I., Galea, S. and Carman, G.P., 2010. A low profile vibro-impacting energy harvester with symmetrical stops. Applied Physics Letters 97: 234101.

Naghdi, P.M. and Rubin, M.B., 1989. On the significance of normal cross-sectional extension in beam theory with application to contact problems. International Journal of Solids and Structures 25 249–265.

Najafi, K., Galchev, T., Aktakka, E.E., Peterson, R.L. and McCullagh, J., 2011. Microsystems for energy harvesting. Proc. Solid-State Sensors, Actuators and Microsystems. Conf. (Transducers'11), June 2011, Beijing, China pp.1845 -1850.

Park, S., Hah, D., 2008. Pre-shaped buckled-beam actuators: Theory and experiments. Sensors and Actuators A 148 186–192.

Park, G., Rosing, T., Todd, M.D., Farrar, C.R. and Hodgkiss, W., 2008. Energy harvesting for structural health monitoring sensor networks. ASCE Journal of Infrastructure Systems 14 64-79.

Qiu, J., Lang, J.H. and Slocum, A.H., 2004. A curved-beam bistable mechanism. Journal of Microelectromechanical Systems. 13, 137-146.

Rahimi, M., Shah, H., Sukhatme, G.S., Heideman, J. and Estrin, D., 2003. Studying the feasibility of Energy Harvesting in a Mobile Sensor Network. IEEE International Conference on Robotics and Automation Taipei, Taiwan p. 19-24.

Roman, B. and Pocheau, A., 2002. Postbuckling of bilaterally constrained rectangular thin plates. Journal of the Mechanics and Physics of Solids 50 2379 – 2401.

Sarkar P., Huang C., Chakrabartty S., 2013. An ultra-linear piezo-floating- gate strain-gauge for self-powered measurement of quasi-static-strain. IEEE Transactions of Biomedical Circuits and Systems, 7 437 - 450.

Sneller, A.J., Cette, P. and Mann, B.P., 2011. Experimental investigation of a post-buckled piezoelectric beam with an attached central mass used to harvest energy. Proceedings of the Institution of Mechanical Engineers, Part I: Journal of Systems and Control Engineering 225 497–509.

Sodano, H.A., Inman, D.J. and Park, G., 2004. A review of power harvesting from vibration using piezoelectric materials. The Shock and Vibration Digest 36 197-205.

Soliman, M.S.M., Abdel-Rahman, E.M., El-Saadany, E.F. and Mansour, R.R., 2008. A wideband vibration-based energy harvester. Journal of Micromechanics and Microengineering 18 115021.

Stanton, S.C., McGehee, C.C. and Mann, B.P., 2009. Reversible hysteresis for broadband magnetopiezoelastic energy harvesting. Applied Physics Letters 95 174103

Stein, E. and Wriggers, P., 1984. Stability of rods with unilateral constraints, a finite element solution. Computers & Structures 19 205–211.

Tang, L., Yang, Y. and Soh, C.K., 2010. Toward broadband vibration-based energy harvesting. Journal of Intelligent Material Systems and Structures 21 1867–97

Twiefel, J. and Westermann, H., 2013. Survey on broadband techniques for vibration energy harvesting. Journal of Intelligent Material Systems and Structures doi: 10.1177/ 1045389X13476149.

Vangbo, M., 1998. An analytical analysis of a compressed bistable buckled beam. Sensors and Actuators A 69 212-216.

Wickenheiser, A.M. and Garcia, E., 2010. Broadband vibration-based energy harvesting improvement through frequency up-conversion by magnetic excitation. Smart Materials and Structures 19 065020.

Yang. Z, and Yang, J., 2009. Connected vibrating piezoelectric bimorph beams as a wide-band piezoelectric power harvester. Journal of Intelligent Material Systems and Structures 20 569–574.

Zhu, D., Tudor, M.J. and Beeby, S.P., 2010. Strategies for increasing the operating frequency range of vibration energy harvesters: a review. Measurement Science and Technology 21 022001.